

DESIGN AND EVALUATION OF COMPACT HEAT EXCHANGERS FOR HYBRID
FUEL CELL AND GAS TURBINE SYSTEMS

by

Joel David Lindstrom

A thesis submitted in partial fulfillment
of the requirements for the degree

of

Master of Science

in

Mechanical Engineering

MONTANA STATE UNIVERSITY
Bozeman, Montana

April 2005

© COPYRIGHT

by

Joel David Lindstrom

2005

All Rights Reserved

APPROVAL

of a thesis submitted by

Joel David Lindstrom

This thesis has been read by each member of the thesis committee and has been found to be satisfactory regarding content, English usage, format, citations, bibliographic style, and consistency, and is ready for submission to the College of Graduate Studies.

Dr. M. Ruhul Amin

Approved for the Department of Mechanical and Industrial Engineering

Dr. R. Jay Conant

Approved for the College of Graduate Studies

Dr. Bruce McLeod

STATEMENT OF PERMISSION TO USE

In presenting this thesis in partial fulfillment of the requirements for a master's degree at Montana State University – Bozeman, I agree that the library shall make it available to borrowers under rules of the Library.

If I have indicated my intention to copyright this thesis by including a copyright notice page, copying is allowable only for scholarly purposes, consistent with “fair use” as prescribed in the U.S. Copyright Law. Requests for permission for extended quotation from or reproduction of this thesis (paper) in whole or in parts may be granted only by the copyright holder.

Joel David Lindstrom

April 14, 2005

ACKNOWLEDGEMENTS

I would like to thank my advisor, Dr. M. Ruhul Amin, for the generous amount of guidance and support he provided me throughout my research. I would also like to thank Dr. Vic Cundy and Dr. Alan George for their support as committee members. Many thanks to Dr. Doug Cairns, Dr. Ladean McKittrick, and Dr. Mike Edens for their time spent with my thermal stress and creep modeling inquiries.

My appreciation extends to the entire staff of the Department of Mechanical and Industrial Engineering, as well as to my fellow graduate students. Thanks to Dr. Lee Spangler for the opportunity to undertake this research project. This work was supported by the US Department of Energy under a subcontract from FuelCell Energy, Contract No. 18297.

TABLE OF CONTENTS

LIST OF TABLES	vii
LIST OF FIGURES	viii
NOMENCLATURE	xii
ABSTRACT	xvi
1. INTRODUCTION	1
BACKGROUND AND MOTIVATION	2
2. COMPACT HEAT EXCHANGER DESIGN	4
COMPACT HEAT EXCHANGER CHARACTERIZATION	4
Plate-Fin	5
Fin-Tube	8
Microchannel	11
Primary Surface	13
Spiral	14
Compactness Summary	15
DURABILITY	16
FOULING AND CORROSION	20
COST	21
3. PROBLEM FORMULATION AND NUMERICAL METHODOLOGY	23
PERFORMANCE COMPARISON METHOD	23
Mathematical Formulation - Coarse Filter Elimination	23
Mathematical Formulation - Fine Filter Elimination	24
Numerical Procedure - Fine Filter Elimination	28
TRANSIENT THERMAL SIMULATION	31
Mathematical Formulation	32
Solution Methodology	34
THERMAL STRESS SIMULATION	39
CREEP LAW FORMULATION	47
4. MODEL VALIDATION AND GRID INDEPENDENCE	52
FINE FILTER VALIDATION	52
TRANSIENT THERMAL SIMULATION GRID TEST	53

THERMAL STRESS GRID TEST	56
CREEP MODEL VERIFICATION	59
5. RESULTS AND DISCUSSION	60
PERFORMANCE COMPARISON METHOD	60
Coarse Filter Elimination	60
Fine Filter Elimination	64
TRANSIENT THERMAL SIMULATION	70
THERMAL STRESS SIMULATION	75
Low Temperature Heat Exchanger Static Thermal Stress	76
Low Temperature Heat Exchanger Transient Thermal Stress	84
High Temperature Heat Exchanger Thermal Stress Before Creep	90
High Temperature Heat Exchanger Thermal Stress After Creep	99
High Temperature Heat Exchanger Creep Comparison	107
6. CONCLUSIONS AND RECOMMENDATIONS	114
CONCLUSIONS	114
RECOMMENDATIONS FOR FUTURE WORK	118
REFERENCES CITED	121
APPENDICES	126
APPENDIX A: Permission to Use Images.....	127

LIST OF TABLES

Table	Page
1. Compactness	15
2. Partition Plate Material Properties	43
3. Creep Law Constants	50
4. Tensile Stress Grid Sensitivity	57
5. Compressive Stress Grid Sensitivity	58
6. Fuel Preheat Exchanger Selection	63
7. Low Temperature Heat Exchanger Selection	63
8. High Temperature Heat Exchanger Selection	64
9. LTHE Maximum and Minimum Stress Summary	90
10. HTHE Maximum and Minimum Stress Before Creep	94
11. HTHE Maximum and Minimum Stress After Creep	101
12. HTHE Maximum and Minimum Creep Strain	108

LIST OF FIGURES

Figure	Page
1. Counterflow Plate-Fin Heat Exchanger	7
2. Recent Brazed Plate-Fin Design	7
3. Bare and Finned Tubular Heat Exchangers	9
4. Fin-Tube Bundle	10
5. Complete Fin-Tube Heat Exchanger	10
6. Recent Fin-Tube Design	11
7. Printed Circuit Heat Exchanger	12
8. Spiral Heat Exchanger	15
9. Typical Creep Curve ($T > 0.4T_m$)	19
10. Fluid and partition plate grid setup	34
11. Calculation sequence: (a) First half-step and (b) Second half-step	36
12. Heat exchanger partition plate setup for thermal stress and creep calculation	45
13. Creep Fit Verification	51
14. Code Validation, Thermal Density versus Header Width	53
15. Half-step time increment analysis: (a) Hot fluid outlet temperature (b) Cold fluid outlet temperature	55
16. Spatial increment analysis: (a) Hot fluid outlet temperature (b) Cold fluid outlet temperature	55
17. Plain Fin Thermal Density versus Compactness	65
18. Louver Fin Thermal Density versus Compactness	65
19. Strip Fin Thermal Density versus Compactness	66
20. Wavy Fin Thermal Density versus Compactness	66

21. Printed Circuit Thermal Density versus Compactness	67
22. Fin Comparison, Thermal Density versus Compactness	67
23. Fin Comparison, Flow Length versus Compactness	68
24. Fin Comparison, Thermal Density versus Flow Length	68
25. Ramping rate of 0.03 °K/s: (a) Heat transfer to and from a single heat exchanger plate, (b) Heat lag	71
26. Ramping rate of 0.3 °K/s: (a) Heat transfer to and from a single heat exchanger plate, (b) Heat lag	71
27. Ramping rate of 3.0 °K/s: (a) Heat transfer to and from a single heat exchanger plate, (b) Heat lag	72
28. Ramping rate of 30.0 °K/s: (a) Heat transfer to and from a single heat exchanger plate, (b) Heat lag	72
29. Outlet temperatures for ramp rates 3.0 and 30.0 °K/s: (a) Hot side, (b) Cold side	73
30. Contour plot of temperature in the fluid and partition plate for: (a) steady state and (b) 0.03, (c) 0.3, (d) 3.0, and (e) 30.0 °K/s ramp rate cases	75
31. Body Temperature and Magnified Strain in Steady State LTHE	76
32. Steady State LTHE Four-Bar Linkages at Reference Temperature	77
33. Steady State LTHE Four-Bar Linkages at Operating Temperature	78
34. Four Bar Linkage Representation	78
35. Y Component Stress in Steady State LTHE	81
36. Z Component Stress in Steady State LTHE	82
37. YZ Shear Stress in Steady State LTHE	83
38. Von Mises Equivalent Stress in Steady State LTHE	83
39. Maximum transient thermal stress occurrences for the 30.0 °K/s ramp rate case: (a) Heat transfer to and from a single heat exchanger plate, (b) Von Mises Equivalent stress, and (c) Y and Z Component stresses	85

40. Body Temperature and Magnified Strain in Transient State LTHE 86

41. Y Component Stress in Transient State LTHE 87

42. Z Component Stress in Transient State LTHE 88

43. YZ Shear Stress in Transient State LTHE 88

44. Von Mises Equivalent Stress in Transient State LTHE 89

45. Body Temperature and Magnified Strain in HTHECA Before Creep 91

46. Body Temperature and Magnified Strain in HTHECB Before Creep 91

47. Y Component Stress in HTHECA Before Creep 95

48. Y Component Stress in HTHECB Before Creep 95

49. Z Component Stress in HTHECA Before Creep 96

50. Z Component Stress in HTHECB Before Creep 96

51. YZ Shear Stress in HTHECA Before Creep 97

52. YZ Shear Stress in HTHECB Before Creep 97

53. Von Mises Equivalent Stress in HTHECA Before Creep 98

54. Von Mises Equivalent Stress in HTHECB Before Creep 98

55. Body Temperature and Magnified Strain in HTHECA After Creep 100

56. Body Temperature and Magnified Strain in HTHECB After Creep 100

57. Y Component Stress in HTHECA After Creep 102

58. Y Component Stress in HTHECB After Creep 102

59. Z Component Stress in HTHECA After Creep 103

60. Z Component Stress in HTHECB After Creep 103

61. YZ Shear Stress in HTHECA After Creep 104

62. YZ Shear Stress in HTHECB After Creep 104

63. Von Mises Equivalent Stress in HTHECA After Creep 105

64. Von Mises Equivalent Stress in HTHECB After Creep	105
65. X Component Creep Strain in HTHECA	109
66. X Component Creep Strain in HTHECB	109
67. Y Component Creep Strain in HTHECA	110
68. Y Component Creep Strain in HTHECB	110
69. Z Component Creep Strain in HTHECA	111
70. Z Component Creep Strain in HTHECB	111
71. YZ Shear Creep Strain in HTHECA	112
72. YZ Shear Creep Strain in HTHECB	112
73. Von Mises Equivalent Creep Strain in HTHECA	113
74. Von Mises Equivalent Creep Strain in HTHECB	113

NOMENCLATURE

<u>Symbol</u>	<u>Description</u>
a	Parting plate thickness (m)
A	Total heat transfer area on one side of the heat exchanger, $NTU \cdot C_{\min}/U$, or the heat transfer area of the control volume encompassed by one fin on one side of a single heat exchanger cell (m^2)
A_c	Cross sectional area of the control volume encompassed by one fin on one side of a single heat exchanger cell (m^2)
A_{fr}	Heat exchanger frontal area, A_o/σ , (m^2)
A_o	Minimum free flow area, m_d/G , (m^2)
A_r	Fin area per total area (---)
b	Heat exchanger plate spacing (m)
$B_{1...3}$	Creep function constants (---)
C	Heat capacity rate ($W/^\circ K$)
c_{ijkl}	Material constitutive tensor (Pa)
$C_{1...4}$	Creep law constants (---)
cp	Heat capacity ($J/gm \cdot ^\circ K$)
D_h	Hydraulic diameter (m)
d_{ij}	Rate of deformation tensor (1/s)
dx	Spatial increment across plate thickness (m)
dy	Spatial increment across plate length (m)
dz	Spatial increment across plate width (m)
e	Deformation tensor (---)
E	Elastic modulus (GPa)

f	Fanning friction factor (---)
F	Geometric similarity scale reduction factor (---)
f_i^B	Body force component (N)
f_i^S	Surface traction component (Pa)
g_c	Force-mass conversion constant (32.174 lb·ft/lbf·s ²)
G	Mass velocity (kg/m ² ·s)
h	Convective heat transfer coefficient, (W/m ² ·°K)
j	Colburn factor (---)
k	Thermal conductivity (W/m·°K), or Boltzmann's Constant (1.3807·10 ⁻²³ J/°K)
l	Fin length (m)
L	Core length, $D_h \cdot A/4 \cdot A_o$, (m)
m_d	Mass flow rate (kg/s)
n	Stress exponent (---)
N_0	Avogadro's Number (6.0221·10 ²³ 1/mole)
NTU	Number of heat transfer units (---)
ntu	Number of heat transfer units based on one fluid side, $\eta_o \cdot h \cdot A/C$, (---)
P_f	Fin pitch (1/m)
PQ	Percent Heat (---)
Pr	Prandtl number (---)
Q	Total heat exchanger duty, or heat transfer rate into or out of a single partition plate (W)
Q_{\max}	Maximum possible heat exchanger duty (W)
R	Gas constant, $k \cdot N_0$, (8.3145 J/mole·°K)

Re	Reynolds number, $G \cdot D_h / \mu$, (---)
S	Surface of deformed body
t	Time (s)
T	Temperature ($^{\circ}\text{K}$)
TD	Heat exchanger thermal density, Q/V , (MW/m^3)
u	Displacement (m)
U	Overall heat transfer coefficient ($\text{W}/\text{m}^2 \cdot ^{\circ}\text{K}$)
v	Velocity (m/s)
V	Heat exchanger volume, A/α , (m^3), or volume of deformed body
W	Internal virtual work (J)
X	Spatial component across plate thickness (m)
Y	Spatial component across plate length (m)
Y_s	0.2 % offset yield strength (MPa)
Z	Spatial component across plate width (m)

Greek Symbols

α	Ratio of total heat transfer area on one side of an exchanger to the total volume of the exchanger (m^{-1}), or thermal expansion coefficient ($1/^{\circ}\text{K}$)
β	Compactness, ratio of heat transfer area on one side of a heat exchanger to the volume between the plates on that side (m^2/m^3)
δ	Fin thickness (m), or variation operator or virtual operator
ΔH	Activation energy for creep (kJ/mole)
ΔP	Pressure drop of one fluid side (kPa)
ΔQ	Heat lag (W)

ε	Heat exchanger effectiveness, Q/Q_{\max} , (---)
ε_c	Creep strain (---)
η_f	Fin efficiency (---)
η_o	Extended surface efficiency, $1-A_r(1-\eta_f)$, (---)
μ	Dynamic viscosity (cp)
ν	Poisson's ratio (---)
ρ	Density of working fluid or partition plate (kg/m^3)
σ	Ratio of free flow area to frontal area (---), or stress (MPa)

Subscripts

c	Cold fluid side
h	Hot fluid side
i	Inlet
m	Mean or melt
max	Maximum
met	Metal
min	Minimum
n	New
o	Outlet
s	Scale
w	Wall
1	One side of the heat exchanger
2	Other side of the heat exchanger

ABSTRACT

Hybridized Carbonate and Solid Oxide fuel cell power plants are currently under investigation to fulfill demands for high efficiency and low emissions. Selection and design of high performance heat exchangers are essential for such applications. In this work, various compact heat exchanger (CHEX) technologies pertinent to gas-gas recuperative duties are presented. The CHEX types considered include brazed plate-fin, fin-tube, microchannel, primary surface and spiral. Based on a comparative rating procedure, two CHEX designs namely, plate-fin and microchannel were chosen for further review. Plain, strip, louver, wavy and semicircular surface geometries were then evaluated with a numerical CHEX sizing procedure. The brazed plate-fin CHEX having the louver fin geometry was determined the most conducive with hybrid fuel cell and gas turbine systems.

Multiple numerical modeling efforts were carried out to develop plate-fin heat exchanger design recommendations. A model was created for the transient thermal simulation of counterflow heat exchanger partition plates. For this analysis, an alternating direction implicit finite difference scheme was written in the Java programming language to model temperature in the working fluids and partition plate. Thermal stress was then calculated in various partition plate designs for steady state and transient modes of operation. Thermal stress was modeled in two heat exchanger materials, stainless steel 304 and Inconel 625. A primary creep law was developed for Inconel 625 to simulate creep behavior in high temperature (up to 1150 °K) heat exchanger partition plates.

The results of the transient thermal simulation clearly show the effect of temperature ramping rate on the rate of heat transfer between the working fluids and partition plate. Thermal stress results confirm that additional stress produced in heat exchanger partition plates during transient operation is negligible for temperature ramping rates consistent with high temperature fuel cells. Based on this result it is suggested that employing slow temperature ramping permits the use of higher performance heat exchanger designs, given that damage generally accrued during transient operation is circumvented. Thermal stress results also show that heat exchanger partition plate aspect ratio (Width/Length) plays a major role on the amount of thermal stress produced within the plate. More importantly, this change in aspect ratio has an even larger effect on creep behavior.

CHAPTER 1

INTRODUCTION

Fuel cell technology has been identified to meet simultaneous demands for more electric power and less pollution. Fuel cells are electrochemical devices that convert chemical energy directly to electrical energy with very high efficiency. Due to their electrochemical conversion, fuel cell systems retain very low emission levels and exhibit “good neighbor characteristics”. Distributed fuel cell power systems are desired since they could offer higher grid reliability than centralized power stations and circumvent further installation and maintenance of transmission lines. In particular, high temperature fuel cells can utilize existing natural gas infrastructures effectively. Carbonate and Solid Oxide fuel cells operate at high temperature (900 °K – 1300 °K) and reject a significant amount of heat so that hybridized fuel cell and gas turbine (FCGT) power plants are under investigation. Ultra high fuel to electricity conversion efficiencies (>70% LHV) of such designs have been projected, Leo et al. (2000).

Proper heat exchanger selection and design are instrumental to the success of a hybrid FCGT power plant. A heat exchanger with low effectiveness will have a large impact on system cost with only minimal impact on system output, and similarly, a heat exchanger with very high effectiveness will have a large size so that it will be too expensive to make the best overall impact, Utriainen and Sunden (2001a).

Three different heat exchanger process conditions were analyzed for the hybrid FCGT application, namely a Fuel Preheat Exchanger, a Low Temperature Heat

Exchanger (up to 950 °K), and a High Temperature Heat Exchanger (up to 1150 °K). Much of the present work was focused on the High Temperature Heat Exchanger due to its very high operating temperature. Significant focus was also spent on the Low Temperature Heat Exchanger since it generally has operating conditions conducive with transient modeling.

Background and Motivation

In the early 1970s use of recuperation was limited by low thermal effectiveness, inability to remain leak tight, failures induced by thermal stress, performance degradation due to fouling, large size, and high cost, McDonald (1997). Heat exchangers have made improvements over the years, however, each of the mentioned issues remain only to a lesser extent. Another reason why early heat exchangers had a slow reception is that designers were adding these bulky units to existing engines with no cycle modifications to fully utilize the additional hardware. For example, the entire layout of a gas turbine power plant has been reversed to accommodate a simplified flow path for the recuperated gas, Esbeck et al. (1998).

Compact heat exchangers have traditionally been sought in the aerospace industry due to the strong incentive to minimize exchanger weight and volume. Conversely, low cost and rugged dependability have been, by convention, the principle considerations for stationary systems, Fraas and Ozisik (1965). However, it should be considered that high temperature fuel cell systems have much lower power density than competing gas turbine systems, and distributed power stations will likely have demand in urban areas. Thus,

heat exchanger size has turned into a critical issue. Many hybrid FCGT system designs also require a heat exchanger constructed out of an expensive high temperature alloy, further necessitating optimal heat exchanger design. Further, to achieve an overall system efficiency of greater than 70%, very low heat exchanger pressure drops are needed, initiating more challenges to creating a compact design.

CHAPTER 2

COMPACT HEAT EXCHANGER DESIGN

Compact Heat Exchanger Characterization

Compact heat exchangers offer the ability to transfer heat between large volumes of gas with minimum footprint. A gas to fluid exchanger is considered compact if it has a heat transfer area to volume ratio greater than $700 \text{ m}^2/\text{m}^3$ on at least one of the fluid sides, Shah (2000). Compactness is a good indication of performance, the higher the compactness generally the higher the effectiveness for a given pressure drop, Oswald (2003). Increased compactness can be achieved by reducing the size of the heat exchanger passages or by adding secondary surfaces (fins) within the passage. Compact heat exchangers are generally characterized by having a large frontal area and a short flow length. Flow maldistribution can be an undesirable result of this, so that header and distributor design becomes more important as compactness increases, Shah (2002). High compactness is desirable for performance, although increased compactness yields increased thermal stress, which can reduce heat exchanger life, Voss (2004). However, when employing temperature ramping rates consistent with high temperature fuel cells, a heat exchanger with higher compactness and equal pressure drop can be employed without reducing service life, given that severe thermal transients are mitigated.

Small hydraulic diameter tends to imply laminar flow, which is desirable to maintain a reasonable pressure drop given that fluid pumping power is often equally as important as heat transfer rate. However, laminar flow generally does not produce high convection

coefficients, so that inducing secondary flows or interrupting boundary layers is often desired. Secondary flows can displace stagnant fluid areas which will produce a higher convection coefficient. Interrupting developing boundary layers can maintain a high heat transfer coefficient throughout the entire flow passage length. Fins can accomplish both of these tasks, as well as provide structural support for heat exchangers that endure pressure differentials.

Flow arrangement is not a trivial decision in compact heat exchanger design. Flow length in crossflow units is independent of the other fluid stream so that full pressure drop utilization can be achieved by both fluid streams. However, when exchanger effectiveness is high, perhaps greater than 80%, the size of a crossflow unit may become excessive, Shah (1981). The most compact flow arrangement for high effectiveness exchangers is that of counterflow, even though it poses difficulty in headering flow streams to and from the heat exchanger core and denies optimal flow length for one of the two fluid streams. The counterflow design also exhibits the least severe temperature gradients, which is a clear advantage for durability considerations. For balanced flows, counterflow operation with crossflow distributors is a reasonable compromise between header design and heat exchanger compactness.

Plate-Fin

Brazed Plate-Fin exchangers (BPFE) can achieve very high compactness, one surface configuration was found to have $6560 \text{ m}^2/\text{m}^3$, Kraus et al. (2001), which is over ten times that of conventional shell and tube heat exchanger surfaces. BPFES have a long history in gas-gas heat transfer applications because of their ability to achieve such high levels of

compactness. There are numerous surface geometries that have been used in BPFEs. Offset strip-fins have more than 60 years of research behind them and are one of the most widely used geometries that does not call for mass production. Louver fins are also widely used given their mass production manufacturability. Other plate-fin surface geometries include plain triangular, plain rectangular, wavy, offset strip, louver, and perforated plate fin surfaces.

Conventional plate-fin heat exchangers have always been relatively compact, though they have had problems with thermal shock. Rigid plate connections are known to experience a time lag in following the temperature variations in the heat exchanger cells. Perhaps the greatest detriment of the conventional BPF E design is that they often had high stress points induced by inflexible, monolithic structures. These high stress points were often the brazed joints themselves, which are still common points of failure. Brazed joints are difficult to inspect and repair, any defect in a braze connection may propagate over time towards failure. Conventional plate fin exchangers also have a rather high parts count, which compounds the negative aspects of brazing. Thus, quality control in BPF E manufacture is an issue. Some plate-fin heat exchanger manufacturers have opted to use diffusion bonding techniques, which are known to demonstrate much higher strength than braze connections, Kunitomi et al. (1999). An illustration of a generic counterflow plate-fin heat exchanger with crossflow distributors is shown in Fig. 1.

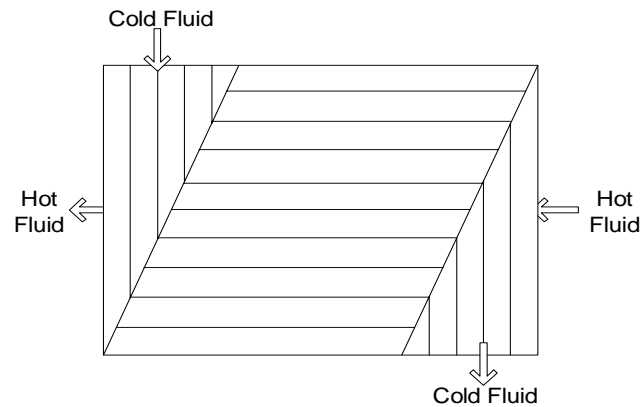


Fig. 1. Counterflow Plate-Fin Heat Exchanger

A commercially available plate-fin heat exchanger manufactured by Ingersoll-Rand is shown in Fig. 2. It is claimed to be a hybrid design of the plate-fin and primary surface heat exchangers, having the principal advantage of durability achieved by non-rigid plate connections. The design has a minimal need for preload during assembly and is modular, where cells and cores can be stacked together to meet a desired heat load. Five different cell sizes are available, including three different plate areas and two different fin heights, Kesseli et al. (2003).

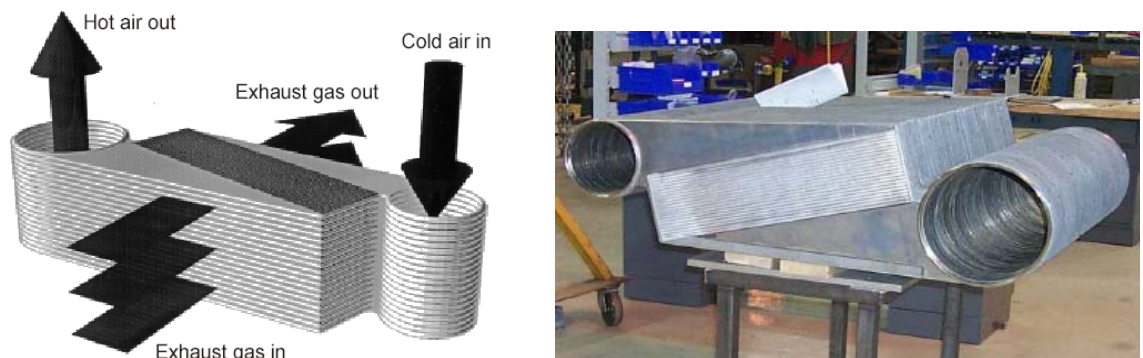


Fig. 2. Recent Brazed Plate-Fin Design (permission to use this image was granted by Ingersoll-Rand Energy Systems, see Appendix A)

Fin-Tube

Compact fin-tube exchangers (FTE) consist of many diverse tube, fin, and flow orientations. Generally, FTEs are comprised of small bore tubes spaced closely together. Crossflow FTEs were found capable of high compactness, having up to $3300 \text{ m}^2/\text{m}^3$ on the fin side, Shah (1981). However, as mentioned previously, high effectiveness sought with crossflow orientation may yield excessive size. Counterflow and spiral flow arrangements are deployed with FTEs, although at a high detriment of low surface compactness. There are two general categories of FTE fins, namely individual and plate fins. The plate fins used for the fin-tube heat exchangers are generally the same as plate-fin heat exchanger surface geometries, where the fins are continuous throughout the core with tube bundles protruding through them. Individual fins can be comprised of longitudinal, annular, helically wound, or pin fins. Plate fins generally allow higher temperatures and pressures than individual fins and are less expensive, although individual fins tend to provide less pressure drop. Turbulators or longitudinal fins can also be added to the inside of the tube to generate secondary flows, eliminate developing boundary layers, and reduce fouling, Behm (2003). When the heat capacities are roughly the same for both fluid streams (balanced flow), fins can be used on both sides of the heat exchanger tube or not at all. Because the heat capacities of both fluid streams are near equal, the convection coefficients, often the greatest resistances to heat transfer, are also near equal. Use of fins in the case of balanced flow is generally to increase heat exchanger compactness.

Bare tube bundles in counterflow as shown in Fig. 3 represent one of the first gas turbine heat exchanger designs manufactured over 40 years ago by Escher-Wyss, Ltd., Fraas and Ozisik (1965). The performance of this design was improved by adding longitudinal fins also shown in Fig. 3; however, the finned design was still not very compact.

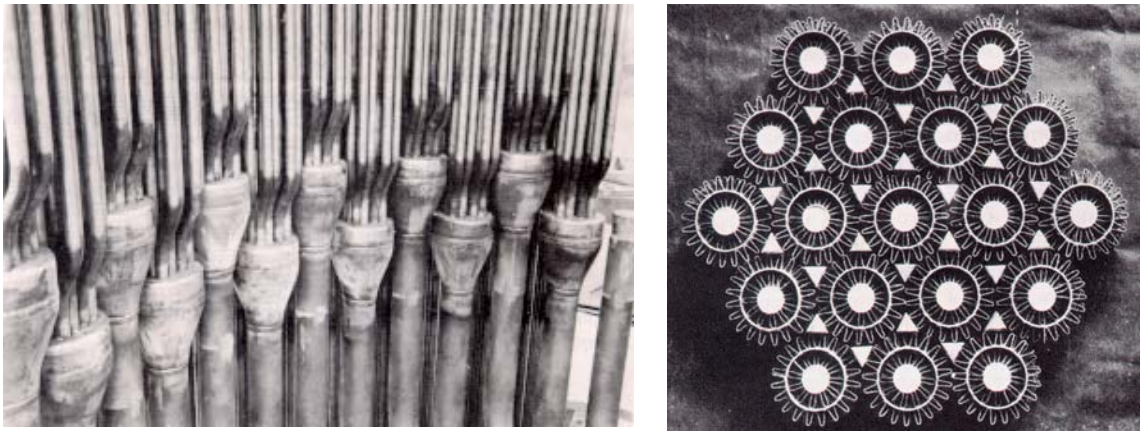


Fig. 3. Bare and Finned Tubular Heat Exchangers (permission to use this image was granted by Axima Refrigeration GmbH, see Appendix A)

It is difficult to attain a highly compact surface in counterflow FTE design, mainly because tubes do not stack together well. This can be realized by identifying the filler shapes used to block gas flow through the interstices of the tube bundle and center of each tube as shown in Fig. 3. Fig. 4 displays an Escher-Wyss tube bundle designed for counterflow operation, which was built with tubes similar to those shown in Fig. 3. Another disadvantage of the conventional FTE is attaching a bundle of individual tubes into a single larger tube, which results in wasted space as demonstrated in Fig. 5.

Headering tubes in this bundle increases flow length without fully contributing to heat exchange. In addition, this type of structure is hardly amenable to modularity.

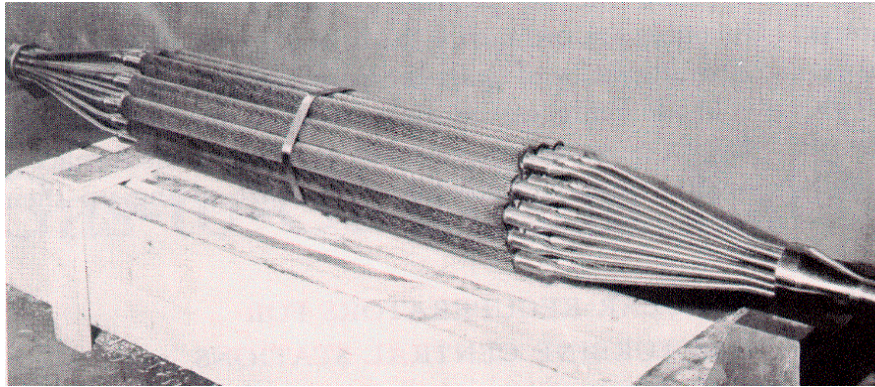


Fig. 4. Fin-Tube Bundle (permission to use this image was granted by Axima Refrigeration GmbH, see Appendix A)

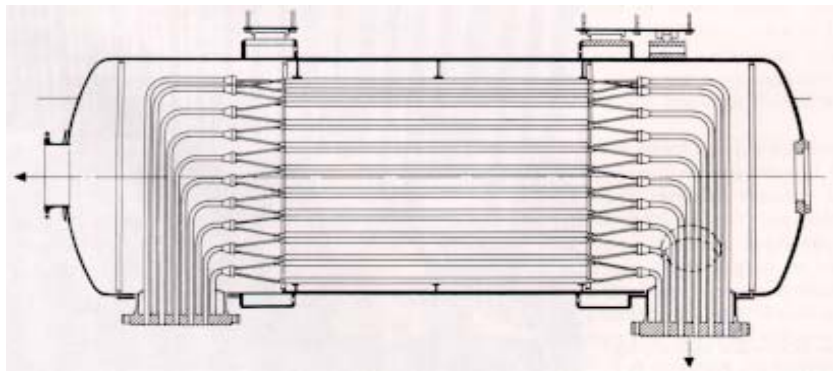


Fig. 5. Complete Fin-Tube Heat Exchanger (permission to use this image was granted by Axima Refrigeration GmbH, see Appendix A)

For relatively low pressure gas / gas operation, the use of tubes is hardly warranted, Behm (2003). Tubes have poor thermal density (exchanger duty / core volume) and are expensive compared to sheets. Moreover, material waste can be comparatively high for crossflow FTE manufacture, which becomes especially important when high temperature

materials are used. FTEs have had success mostly with gas to liquid flow conditions, where low density, low heat capacity gases transfer heat with high heat capacity liquids.

However, the flexibility of tubular construction is well suited to a prescribed envelope, and tubes are suitable for fluids under high pressure. The high pressure fluid is positioned inside the tubes relieving the exchanger shell of the high pressure. The more compact fin-tube design shown in Fig. 6 is a product of MTU Aero Engines GmbH of Germany, which is designed for high pressure ratio aerospace engines. Small bore, oval shaped tubes are good for pressure containment, and can exhibit structural integrity in a cyclic environment.



Fig. 6. Recent Fin-Tube Design (permission to use this image was granted by MTU Aero Engines GmbH, see Appendix A)

Microchannel

Microchannel exchangers are classified by having hydraulic diameter between 10 and 200 μm and minichannel exchangers having hydraulic diameter between 200 to 3000 μm , Kandlikar and Grande (2002). However, this work will consider microchannel

exchangers (ME) as those fabricated from individual flat plates having high compactness. In addition, MEs fabricated specifically by chemical etching will be further classified and referred to as printed circuit heat exchangers (PCHE). The commercially available PCHE shown in Fig. 7 is fabricated by Heatric Ltd. Plates in Heatric's exchangers are diffusion bonded so that the connections are claimed to be as strong as the parent metal.



Fig. 7. Printed Circuit Heat Exchanger (permission to use this image was granted by Heatric, see Appendix A)

It has been reported that true MEs (hydraulic diameter between 10 and 200 μm) can experience unexpectedly high heat transfer performance. It is said that surface roughness is a main parameter of this, which could represent an easily acquired and economical way to pursue CHEX performance enhancement. Because wall roughness plays an important role in microchannel design, it is known that applying conventional Nusselt numbers for given cross sections is erroneous, Reid (1998). Rarefaction and gas compressibility are often necessary considerations for ME design. Depending on the size of the hydraulic diameter, the continuum theory may need to be modified or even abandoned when flow

passages become small enough. In order to prevent the effects of rarefaction, continuum flow analysis may be preserved by maintaining a Knudsen number of less than 0.001, Kandlikar and Grande (2002). Despite this information there is still much difficulty in correlating numerical predictions with experimental ME data. In addition, it is yet to be seen how conducive the PCHE chemical etching technology is with nickel alloys intended for operation above 1075 °K, Wang (2003).

Primary Surface

Primary surface exchangers (PSE) are characterized by having only a primary surface to transfer heat between fluid streams; there are no secondary surfaces (fins). PSEs consist of pairs of corrugated sheets welded together, where the flow path can be orthogonal to or in line with the corrugations. Solar Turbines Inc. has been developing a stamped plate PSE for over 30 years. A unique cross corrugated wavy duct configuration used by Solar Turbines is known to generate secondary flow patterns. Fluid is actually forced to permeate into adjacent ducts as the wavy pattern crosses itself, which in addition to the surface waviness creates very favorable conditions for secondary flow, Utriainen and Sunden (2001b).

It has been reported by Solar Turbines Inc. that clamping cells together, instead of having a rigid cell structure, can permit enough movement between cell contacts to relieve concentrated stresses at weld locations. Sound suppression is also attributed to the damping characteristic of the clamped design, Solar Turbines (1995). However, stamped plate PSE designs are compactness limited due to material properties and manufacturing techniques, and folded sheet PSE designs can suffer from exhaust flow

blockage due to a lack of support structures between cells. The latter consideration is a very important aspect for high temperature (>925 °K) operation. Another disadvantage of PSEs is that they often require a significant preload mechanism which can result in complex manufacturing procedures, Kesseli (2003). Each of these disadvantages are exacerbated as operating temperature exceeds 925 °K and use of less malleable nickel alloys become warranted.

Spiral

Spiral exchangers (SE) consist of two continuous sheets of metal wound in a spiral fashion. Spiral exchangers have traditionally been used with particle laden or high viscosity fluids because of their self-cleaning nature. Scale is swept away because turbulence induced by the swirling fluid path scrubs and flushes the passages clean. A fouling factor of one third that of shell and tube type exchangers is not unusual for SEs. Mechanical cleansing is also a desirable feature available with many of the spiral designs, where often the coil end caps can be removed.

However, SEs were found to have very limited compactness levels of about 1600 m^2/m^3 , Bacquet (2001). In addition, the coiled design can require extensive and laborious manufacturing equipment. Nonetheless, the SE is currently in development and has been proposed by Oswald (2003) to withstand the structural problems of gas turbine heat exchangers. A spirally wrapped primary surface microturbine heat exchanger produced by Acte S.A., of Belgium is shown in Fig. 8.



Fig. 8. Spiral Heat Exchanger (permission to use this image was granted by ACTE s.a., see Appendix A)

Compactness Summary

It was found repeatedly that smaller core volume and increased heat exchanger performance can be obtained largely by increasing surface compactness. Therefore, the compactness criterion was considered very important for the hybrid FCGT application. An extensive literature review was conducted to estimate the range of compactness commonly deployed for each compact heat exchanger type and tabulated in Table 1.

Table 1. Compactness

Exchanger Type	Compactness (m^2/m^3)
Plate-Fin	250 – 6560
Fin-Tube	190 - 3300 / Fin
	138 - 1150 / Tube
Microchannel	2000 - 10,000
Primary Surface	1640 – 3600
Spiral	120 – 1600

Complete detail of numerous BPFE and FTE surface configurations were found in the extensive work of Kays and London (1984). The BPFE was found to have compactness figures of up to $6560 \text{ m}^2/\text{m}^3$, given by Kraus et al. (2001). Compactness data for the FTE were found to reach $3300 \text{ m}^2/\text{m}^3$, although this value being for crossflow orientation only. Data for counterflow FTEs with longitudinal fins could not be found since they are generally not even considered compact, Shah and Webb (1983). The tube side of the FTE displays rather low compactness, reaching only $1150 \text{ m}^2/\text{m}^3$, Shah (1981). The ME is discussed in Wadekar (2003) and Hesselgreaves (2001). The PSE was found to have a compactness range of 1640 to $3600 \text{ m}^2/\text{m}^3$ by Utriainen and Sunden (2001b) and McDonald (2000) respectively. The SE compactness data were found to reach an upper limit of $1600 \text{ m}^2/\text{m}^3$, Bacquet (2001).

Durability

Historically, gas turbine heat exchangers have had very poor reliability. Durability was found to be the single most important design aspect of traditional gas fired engine heat exchangers. Thermal stress is produced in monolithic structures when hot regions expand and are restricted by cooler regions. Plastic and creep deformation derived in heat exchanger components are primarily induced from thermal stress, as opposed to stress induced by gas pressure differentials. Modes of heat exchanger failure commonly known to occur are due to fin blowout, plate rupture, and braze dislocation. Furnace brazing has traditionally been used to connect plates and fins. However, according to

some studies, the reliability of this technique is insufficient when used for conventional gas turbine heat exchangers.

The highest thermal stresses in a heat exchanger can occur during transient operation if the hot inlet rate of temperature change is high enough. Fortunately, temperature ramping will be much slower for most FCGT heat exchangers, since high temperature fuel cells have a much longer start up time and more gradual transients than do traditional gas-fired turbine systems. In addition, most FCGT systems are expected to operate with lower pressure ratios than conventional gas turbine systems. However, some FCGT heat exchangers may be used for load leveling and or quick startup, where they could be subject to stringent temperature ramping rates. This scenario would most likely place durability as the primary design parameter as it is with traditional gas turbine heat exchangers. However, in this work it was assumed that the temperature ramping rate in the heat exchangers follow closely to that of the fuel cells. Therefore, transient durability requirements were considered less severe for the present application compared to conventional gas turbine heat exchangers.

Temperature ramping rates in FCGT system heat exchangers can be several orders of magnitude slower than temperature ramping rates in conventional gas turbine system heat exchangers. Given a slow ramping rate, a more compact heat exchanger with the same pressure drop can be designed while still maintaining sufficient heat exchanger service life. The configuration of which will be characterized by having a short flow length and large frontal area. The point to which thermal performance can be increased or pressure

drop decreased (both coincident with shortening plate flow length) can be evaluated using the modeling techniques discussed herein.

Creep is often attributed as the primary degradation mechanism for components that endure high temperature operation. This is especially apparent when the operating temperature exceeds $2/3$ the melting point of the material of construction. Creep in polycrystalline materials occurs as a result of the motion of dislocations within grains, grain boundary sliding, and diffusion processes. There are three major stages of creep: primary, secondary, and tertiary. These three stages can be distinguished in Fig. 9, which represents a typical creep curve when a material is tested at constant stress and temperature ($T > 0.4T_m$). The primary stage consists of a movement of atoms in the material's crystal lattice when a load is applied. During the primary creep phase, work-hardening gradually inhibits the dislocation motion. Thus, creep strain rate is rapid at first and gradually slows to a relatively constant rate. As this occurs, the secondary region of creep strain begins to dominate. In the secondary or steady state creep phase, work-hardening and thermally activated recovery (softening) processes are generally balanced. Thus, the secondary creep phase corresponds with the relatively linear portion of the creep curve shown in Fig. 9. The tertiary creep phase consists of a rapid move towards failure, which is usually accelerated by a reduction in cross sectional area from the formation of macro-sized cracks and necking. The tertiary range of creep is generally not of concern when modeling, as it is normally considered to have reached the point of failure when this phase of creep is initiated. As mentioned, when the temperature grows above $2/3$ the melting point of the material, creep becomes progressively more prevalent.

This will be a very important factor for the high temperature FCGT heat exchanger design. Small amounts of creep are usually recovered, but for the most part, creep strain can be regarded as permanent, Webster and Ainsworth (1994).

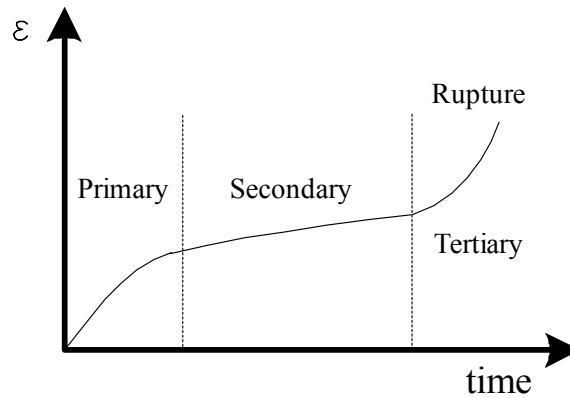


Fig. 9. Typical Creep Curve ($T > 0.4T_m$)

A sensible approach to structural and life cycle analyses used to develop a leading counterflow plate-fin heat exchanger was summarized in Kretzinger et al. (1983), Valentino (1980), and Parker (1977). In these papers, rigorous use of finite element modeling was described, which was used to obtain information needed for calculating low cycle fatigue life of the heat exchanger components with creep interaction. A commonly used sequence of steady state thermal and stress analyses, transient operation stress analyses, creep analyses, and service life calculations was deployed. This pioneering work was carried out by AIRsearch Manufacturing Company.

Fouling and Corrosion

Fouling in gas turbine heat exchangers is typically from the deposition of unburnt hydrocarbons on the heat transfer surface, which typically occurs on the cooler portion of the exhaust gas side of the heat exchanger. Fouling is one of the major potential problems in compact heat exchangers due to small hydraulic diameter and lack of cleaning ability. Fouling can reduce the heat transfer coefficient 5 to 10%, but can increase the pressure drop up to several hundred percent, particularly for compact heat exchangers with gas flow, Shah (2000). Fouling mechanisms are generally understood, but little success has been made in prediction and prevention. Effective cleaning techniques will be an increasingly important requirement for CHEX design. To reduce the effects of fouling, filters may be used, flow streams may be pulsated, fluids may be reversed, the cold fluid may be stopped, chemicals may be added to the flow streams or even baking and rinsing the entire core is a possibility, Deakin et al. (1999). None of these techniques are as effective as mechanical cleansing. By convention, the only relevant CHEX type known to have this feature is that of the spiral configuration. To determine the presence of carbonaceous material buildup during operation, a carbon monoxide detector can be used to monitor the exchanger effluent streams.

Corrosion processes in heat exchangers can be reduced by utilizing appropriate alloys for their construction. There are several different mechanisms of corrosion damage, including uniform, galvanic, crevice, pitting, intergranular, erosion, and stress-corrosion cracking, Walker (1990). Water vapor is known to have a deleterious role on the oxidative lifetime of metallic heat exchangers, Pint et al. (1999). This is an important

consideration for FCGT heat exchangers where process streams have significant steam content. Stainless steel is commonly used in heat exchanger applications up to 925 °K because of its combination of low cost, durability, and corrosion resistance. However, temperatures in excess of 925 °K must be endured by some FCGT heat exchangers. Nickel is an attractive metal for use in severe operating conditions that consist of corrosive environments and temperatures above 925 °K. Nickel is ductile and tough so that nickel alloys can be machined by standard conventions. Although, when a heat exchanger has to be made from an expensive nickel alloy, the cost of raw material generally dominates the cost of the exchanger, Deakin et al. (1999).

Cost

High compactness is desired for FCGT heat exchangers, although increased compactness will generally reflect in increased capital cost. For a given pressure drop, the higher is the compactness, shorter is the flow length and larger is the frontal area. This implies that higher compactness yields smaller plate size, resulting in higher fabrication cost. However, higher compactness generally yields higher CHEX performance, so that a trade study may be warranted to develop an optimal design.

Many heat exchangers require manual assembly, which adds a significant cost factor. The quantity of individual components which constitute a complete heat exchanger has a large bearing on overall cost, McDonald (2000). Typically, individual exchanger parts need forming, fitting, welding, testing, and often manual assembly. Therefore, manufacturability is a vital criterion for comparative evaluation of different heat

exchanger designs. For example, the PSE generally requires fewer parts than the BPFE since it does not have secondary surfaces. Although, as reported by Ingersoll-Rand (2001), PSE designs often require a heavy preload mechanism, a complex manufacturing technique that could completely offset the gain in cost effectiveness due to a low parts count.

Another consideration is that modular “off the shelf” type heat exchangers are generally more cost effective. This is due to the fact that retooling fabrication machinery for every heat exchanger size is not warranted. It is reasonable to expect that custom heat exchanger fabrications will demand higher capitol costs. Manufacturing capability is also a significant aspect when soliciting high temperature (>925 °K) heat exchanger designs, where use of less malleable nickel alloys is generally warranted. Market size and availability is vital to heat exchanger cost based on simple economic analysis. CHEXs that have a longer deployment history generally have a cost advantage due to more developed design and fabrication techniques. A useful documentation of brazed plate-fin heat exchanger cost was published in Kesseli et al. (2003). It should also be noted that heat exchanger cost has a very strong dependence on effectiveness and pressure drop specifications. A detailed life cycle cost analysis should be carried out to maximize a power plant’s economic return.

CHAPTER 3

PROBLEM FORMULATION AND NUMERICAL METHODOLOGY

Performance Comparison Method

The two step heat exchanger selection approach outlined by Wadekar (2003) was used to carry out this procedure. The first step consists of a Coarse Filter elimination, where all CHEX types are compared and most of which eliminated. The second step consists of a Fine Filter elimination, where different surface geometries of the remaining CHEX types are evaluated, resulting in the selection of the single best performing surface geometry for the present application.

Mathematical Formulation - Coarse Filter Elimination

A numerical rating procedure was used to select the two most compatible CHEX types for the three general FCGT process conditions: Fuel Preheat Exchanger, Low Temperature Heat Exchanger, and High Temperature Heat Exchanger. The criteria used to make this selection include compactness, durability, material cost, manufacturability, availability, maintenance, and applicability. Each of these criteria was given a weight factor according to its importance for each FCGT process condition. The weighting scale was defined as a range from one to five, where five carried the most importance. The weights given to each criterion for each process condition consist of the following:

1. Compactness was assigned a weight factor of five for all three FCGT process conditions.

2. Durability was assigned a weight factor of four for the Fuel Preheat Exchanger and five for both Low and High Temperature Heat Exchangers.
3. Material Cost was assigned a weight factor of three for the Fuel Preheat Exchanger and Low Temperature Heat Exchanger assuming stainless steel is used. A weight factor of five was assigned for the High Temperature Heat Exchanger assuming a nickel alloy is used.
4. Manufacturability was assigned a weight factor of two for the Fuel Preheat Exchanger and Low Temperature Heat Exchanger assuming stainless steel is used. A weight factor of 4 was assigned to the High Temperature Heat Exchanger assuming a nickel alloy is used.
5. Availability, maintenance, and applicability were assigned a weight factor of three for all three FCGT process conditions.

Mathematical Formulation - Fine Filter Elimination

It should be noted that vendor manufacturing characteristics (available plate and fin sizes) should be considered at this point in order to proceed in an effective manner. As illustrated subsequently in Chapter 5, the BPFE and ME were chosen for further review in the present elimination step. Thus, the Fine Filter elimination model was developed using the plate-fin heat exchanger sizing procedure outlined by Shah (2000). This procedure requires specification of all inlet and outlet fluid properties, NTU, and all surface properties geometrical and thermal-hydraulic. From these inputs, the CHEX dimensions necessary to meet a prescribed heat duty can be found, with which the Fine Filter elimination procedure is based.

The High Temperature Heat Exchanger process condition was considered in the present CHEX sizing analysis since it requires high effectiveness (>90%) and is therefore commonly sought after. Thus, the control volume for the Fine Filter mathematical formulation was taken as the counterflow heat exchange portion of Fig. 1. Mathematical expressions for certain terms subsequently mentioned but not shown can be found in the nomenclature section. The idealizations made in this analysis consist of the following:

1. The control volume was considered adiabatic
2. Heat transfer coefficients were considered constant
3. Extended surface efficiencies were considered constant
4. Temperature gradients transverse to the flow direction were neglected
5. Flow maldistribution was neglected
6. Longitudinal conduction was neglected
7. Entrance effects were neglected
8. Radiation was neglected

Idealizations 1 through 6 were adopted from the plate-fin heat exchanger sizing procedure outlined in Shah (2000). Entrance effects were neglected for the purpose of surface selection, though they were accounted for in the actual heat exchanger calculations discussed in subsequent chapters. Radiation was also neglected in the Fine Filter elimination model, as it was in the procedure outlined in Shah (2000). However, radiation could be important when a high concentration of water vapor and or carbon dioxide is present, Shah and Sekulic (2003). In this case, the heat exchanger sizing

procedure outlined by Shah (2000) can still be used, where radiation heat transfer coefficients would be added to their respective hot and cold fluid convective heat transfer coefficients. It was assumed that the concentration of water vapor and carbon dioxide in the hybrid FCGT system heat exchangers will not be high enough to affect the Fine Filter model results significantly. Therefore, the numerical evaluations performed in this work do not account for radiation.

As described by Shah (2000), given known process conditions, surface geometries, and estimated extended surface efficiencies, initial core mass flux terms can be obtained for each fluid side using:

$$G = \sqrt{\frac{2 g_c \Delta p}{\left[\frac{f}{j} \frac{ntu}{\eta_o} \frac{1}{\rho} Pr^{\frac{2}{3}} + 2 \left(\frac{1}{\rho_o} - \frac{1}{\rho_i} \right) \right]}} \quad (1)$$

Core Reynolds numbers are then obtained using the core mass flux terms and other known variables. With known surface geometries and Colburn data, heat transfer coefficients are calculated with:

$$h = j G c_p Pr^{\frac{-2}{3}} \quad (2)$$

Depending on the type of surface geometry, a particular relationship is used to determine the fin efficiency for each side of the heat exchanger, followed by evaluating

extended surface efficiencies. An initial overall heat transfer coefficient is then found based on known surface geometries and estimated values:

$$U_1 = \left(\frac{1}{\eta_{o,1} h_1} + \frac{1}{\eta_{o,1} h_{s,1}} + \frac{\frac{\alpha_1}{\alpha_2}}{\eta_{o,2} h_{s,2}} + \frac{\frac{\alpha_1}{\alpha_2}}{\eta_{o,2} h_2} \right)^{-1} \quad (3)$$

From this, the total heat transfer area on side 1 of the heat exchanger can be found. Given this area and known surface properties, the heat transfer area on the opposing side can be found. With the current mass velocity values the minimum free flow area can be determined for each fluid side. Next, frontal area is obtained for both fluid sides. Because high effectiveness warrants counterflow orientation, both sides of the heat exchanger must have the same flow length. Therefore, a single frontal area must be agreed upon. It is recommended that the higher frontal area of the two fluid sides is assumed, Shah (1988). The minimum free flow area is then recalculated. Core flow length can then be obtained using parameters from either fluid side. Using the estimated core length and other known parameters, the core pressure drop can be estimated on both heat exchanger sides using:

$$\Delta p = \frac{G^2}{2 g_c} \left[f \frac{4L}{D_h} \frac{1}{\rho} + 2 \left(\frac{1}{\rho_o} - \frac{1}{\rho_i} \right) \right] \quad (4)$$

Wall temperature effects are accounted for in the friction parameter of Eq. (4). Next, the mass flux terms are recalculated using Eq. (4) and the specified pressure drops,

followed by reevaluation of core Reynolds numbers and all subsequent steps described. For the second and subsequent iterations wall resistance is accounted for, so that Eq. (3) becomes:

$$U_1 = \left(\frac{1}{\eta_{o,1} h_1} + \frac{1}{\eta_{o,1} h_{s,1}} + \frac{a A_1}{k_w A_w} + \frac{\frac{A_1}{A_2}}{\eta_{o,2} h_{s,2}} + \frac{\frac{A_1}{A_2}}{\eta_{o,2} h_2} \right)^{-1} \quad (5)$$

The specified and calculated pressure drops are then compared after each iteration. When they are within a desired tolerance the sizing procedure is complete. At this time the heat exchanger dimensions can be obtained.

Numerical Procedure - Fine Filter Elimination

The commercial software Mathcad was used to carry out the Fine Filter numerical setup. Five surface geometries were considered: plain, louver, strip, wavy, and semicircular. The vast majority of surface information assessed with the Fine Filter model was taken from the extensive work of Kays and London (1984). More compact surfaces were derived from Kays and London (1984) using complete geometric similarity. Two objects are geometrically similar when the ratio of any two linear dimensions of one object is the same for the other object. In the case of plate-fin and microchannel surfaces, five parameters must be geometrically scaled to obtain a new set of input information for the Fine Filter model. For each new surface, the plate spacing, fin pitch, fin thickness, hydraulic diameter, and compactness parameters were reduced in size by a scale factor (F) as follows. Scaled values for plate spacing, fin thickness, and

fin pitch were straightforward to obtain given they are linear dimensions. An original fin pitch would be multiplied by F to obtain the new fin pitch, and similarly, the original values of plate spacing and fin thickness would be divided by F to obtain their new values. Obtaining reduced scale figures for hydraulic diameter and compactness were not as straightforward however, since they are not linear dimensions. The following derivation was used to determine scaled values for hydraulic diameter and compactness parameters.

For the louver fin surface geometry, the cross sectional area and total area of the control volume encompassed by one fin on one side of a single heat exchanger cell were found to be most accurately expressed by Eqs. (6) and (7) respectively:

$$A_c = \frac{b}{P_f} - \delta \sqrt{\left(b^2 + \frac{1}{P_f^2}\right)} \quad (6)$$

$$A = \left[\frac{2}{P_f} - \delta + 2 \sqrt{\left(b^2 + \frac{1}{P_f^2}\right)} \right] L \quad (7)$$

The actual volume that encompasses these two areas can be represented by Eq. (8):

$$V = \frac{b}{P_f} \quad (8)$$

Hydraulic diameter as defined by Kays and London (1984) can be presented as:

$$D_h = \frac{4 A_c L}{A} \quad (9)$$

Substituting Eqs. (6) and (7) into Eq. (9), the hydraulic diameter of a louver fin heat exchanger can be defined as:

$$D_h = \frac{4 \left[\frac{b}{P_f} - \delta \sqrt{\left(b^2 + \frac{1}{P_f^2} \right)} \right]}{\left[\frac{2}{P_f} - \delta + 2 \sqrt{\left(b^2 + \frac{1}{P_f^2} \right)} \right]} \quad (10)$$

By inserting the scaled values for fin pitch, plate spacing and fin thickness into Eq. (10), the expression for the new hydraulic diameter can be simplified and shown as:

$$D_{h,n} = \frac{D_h}{F} \quad (11)$$

Louver fin compactness may be presented as:

$$\beta = \frac{A}{V} = \frac{\frac{2}{P_f} - \delta + 2 \sqrt{\left(b^2 + \frac{1}{P_f^2} \right)}}{\frac{b}{P_f}} \quad (12)$$

Similarly, by substituting the new values for fin pitch, plate spacing and fin thickness into Eq. (12), the expression for the new compactness can be simplified and shown as:

$$\beta_n = F \beta \quad (13)$$

Similar derivations were developed for the various surface geometries, such as the wavy, offset strip, and printed circuit configurations.

The Fine Filter model remained identical for each surface analysis with exception to the heat transfer and friction characteristics unique to the given surface, which also bears distinct values for the following surface properties: hydraulic diameter, compactness, fin pitch, plate spacing, fin thickness, fin area / total area, and fin length. Optimization attempts such as using multiple fin layers or cross corrugated wavy patterns were ignored in this comparison. The fin layers for both hot and cold fluid sides were assigned identical. In general, this type of configuration would not yield a competitive CHEX design, but does provide a tractable fin performance comparison. Eight iterations were carried out for each surface analyzed to obtain a consistent high level of convergence.

Transient Thermal Simulation

A heat exchanger life cycle analysis can be evaluated only when temperature distributions during steady state and transient periods are obtained. Ideally, a stress strain cycle would be constructed for the various heat exchanger components under duress. For the plate-fin design, three major components to evaluate are the partition plates, fins, and braze connections. In this work, a numerical model was developed for counterflow heat exchangers, which was used to predict static and transient temperature profiles of the working fluids and partition plate.

Mathematical Formulation

To evaluate heat exchanger service life, prediction of temperature profiles during transient operation is needed to predict peak stress and strain levels, followed by creep deformation. To address this task for counterflow heat exchanger partition plates, an alternating direction implicit (ADI) finite difference scheme was written to model transient heat flow between the partition plate and the hot and cold working fluids. The thermal analysis control volume was simplified to a thin strip of metal having no fin or braze attachments, but with convective heat transfer coefficients at the solid-fluid boundaries that would force a known heat flux. It should be noted that use of the spray-type of braze could be evaluated with this model, given it is generally in the form of a flat and uniform surface. However, use of braze on the partition plate surface was neglected in this analysis. Flow maldistribution was also neglected in this model as it was in the Fine Filter model. This idealization stipulates that temperature will be uniform along the width dimension of the plate, so that only the length and thickness dimensions were analyzed in the Transient Thermal Simulation model.

A high effectiveness ($\epsilon > 90\%$) counterflow heat exchanger was used as the platform for this work since it is commonly sought after. The heat transfer coefficients and plate dimensions necessary to meet the steady state heat exchanger operating requirements were calculated using the Fine Filter model. The heat transfer surface considered for both hot and cold fluid sides of the heat exchanger were geometrically scaled versions of the $\frac{1}{2}$ – 11.1 louver fin presented in Kays and London (1984).

Plate dimensions, heat transfer coefficients, and a specified temperature ramp schedule were input information to the present analysis. The ramp schedule used is defined as follows. The cold fluid inlet temperature was held constant at 500 °K throughout the analysis period. The hot fluid inlet temperature was held at 700 °K until a steady state condition was obtained. The hot fluid inlet temperature was then ramped up linearly to the peak temperature of 910 °K and held until a steady state condition was again obtained. The numerical computation automatically terminated at this point.

Mass flow rates, pressures, specific heats, densities, heat transfer coefficients, and thermal conductivity were all held constant throughout this analysis. The heat transfer coefficients were calculated in the Fine Filter model to be 363.2 W/m²·°K and 815.7 W/m²·°K for the hot and cold fluid sides respectively. The metal was taken as stainless steel 304 and considered to have an average and constant thermal conductivity of 20.6 W/m·°K. The dimensions of the simplified partition plate were calculated to be 22.0 cm x 38.1 cm x 0.0381 cm (Length x Width x Thickness). The compactness of the flow passages were assigned to be 1806 m²/m³ and 4214 m²/m³ on the hot fluid and cold fluid sides respectively.

Four different temperature ramping rates were evaluated to assess the wide spectra of rates regularly used in industry. Ramping rate refers to the rate at which either the hot or cold fluid inlet temperature is increased or decreased. In this work, only the hot fluid inlet temperature was ramped, which was increased by a specified rate. The slowest ramping rate was consistent with typical high temperature fuel cell operation of 0.03 °K/s. The highest ramping rate was consistent with peak values used in standby gas

turbine systems of 30.0 °K/s. The purpose of this comparison was to assess the harmful effects of temperature ramping on counterflow gas / gas heat exchangers. It will be shown that heat exchangers designed for slow ramping rates can endure higher performance levels, given that plastic strain damage suffered during transient operation is mitigated.

Solution Methodology

A representation of an enlarged view of the fluid and partition plate control volume mesh is shown in Fig. 10. In the actual mesh there were 248 nodes along the thickness and 125 nodes along the length of the plate. The outermost nodes in the shaded element columns on each side of the partition plate represent the hot and cold fluid temperatures. Thus, the total control volume mesh consisted of 250 by 125, or 31,250 nodes.

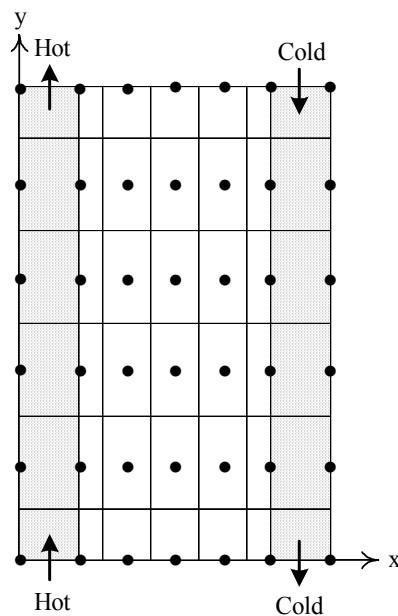


Fig. 10. Fluid and partition plate grid setup

Governing equations for the hot and cold fluid elements were written using an energy balance formulation as represented by Eqs. (14) and (15) respectively. The plate elements were governed by the heat diffusion equation as shown in Eq. (16). The outermost edges of the control volume were assumed adiabatic with exception to the fluid inlets and outlets. The fluid and plate equations were coupled through convective heat transfer boundaries. Each element was governed by an equation that accounted for two dimensional heat transfer and heat capacitance.

$$\rho_h dx dy dz c_p \frac{\partial}{\partial t} T_{hm} = m_{dh} c_{ph} (T_{hi} - T_{ho}) - h_h dy dz (T_{hm} - T_{met}) \quad (14)$$

$$\rho_c dx dy dz c_p \frac{\partial}{\partial t} T_{cm} = m_{dc} c_{pc} (T_{ci} - T_{co}) + h_c dy dz (T_{met} - T_{cm}) \quad (15)$$

$$\rho_{met} c_{pmet} \frac{d}{dt} T_{met} = \frac{\partial}{\partial x} \left(k \frac{\partial}{\partial x} T_{met} \right) + \frac{\partial}{\partial y} \left(k \frac{\partial}{\partial y} T_{met} \right) \quad (16)$$

The governing equations were discretized using the control volume method described in Patankar (1980) and solved using the ADI line-by-line method described in Chapra and Canale (1998). In this procedure, tri-diagonal matrices are utilized yielding a very efficient numerical method. The tri-diagonal matrices were solved using the Thomas Algorithm also described in Chapra and Canale (1998). Temperature calculation for each time increment constituted two half-steps, namely the first half-step and the second half-step. The first half-step comprised solving the solid region equations in the Y-direction and the second half step in the X-direction. Both half-step calculations included solving

the fluid region equations. The calculation sequence used is denoted by the arrows and numbers superimposed on the meshed control volume as shown in Fig. 11 (a) and (b). Each calculation arrow or “sweep” was iterated until a very low tolerance between successive temperature calculations was met. Simpson’s multiple application rule as described in Chapra and Canale (1998) was used to integrate the heat flux along the length of the plate to obtain the total heat transfer rate from the hot fluid to the plate and from the plate to the cold fluid for each time increment.

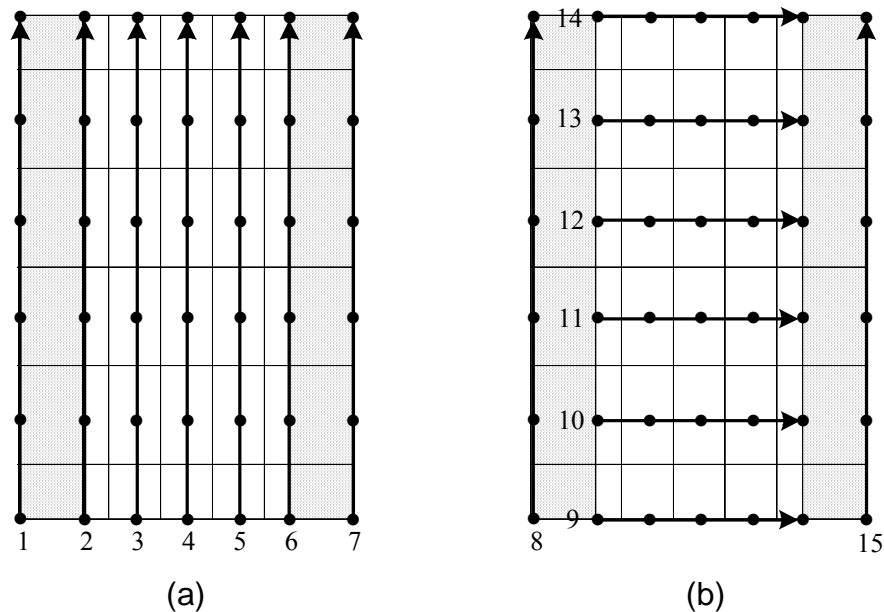


Fig. 11. Calculation sequence: (a) First half-step and (b) Second half-step

Total heat transfer rate and fluid outlet temperature data for both hot and cold fluids were written to a text file after each time increment computation, as opposed to storing this information until the end of the numerical procedure. A similar memory saving technique was used to export temperature data for the entire control volume mesh for the

desired points in time, combining to significantly enhance the model's performance and capability. The code was written in the Java programming language and executed on a PC with 3 GHz processing speed and 1 GB RAM memory. Double precision floating point data type values were used in all calculations.

During a temperature ramp up procedure there is a higher heat transfer rate on the hot fluid side of the plate than on the cold fluid side. This occurrence will increase the temperature of the hot fluid inlet side of the plate faster than the rest of the plate. By having an unequal rate of temperature increase, the hot fluid inlet side of the plate expands faster than the rest of the plate, inducing compressive stress in the hot fluid inlet region. If the thermal stress is high enough, plastic damage can occur within the coincident region of the plate.

The difference of the hot fluid side and cold fluid side heat transfer rate will be referred to as heat lag, or ΔQ as shown in Eq. (17). To normalize ΔQ , the parameter percent heat, or PQ will be reported as shown in Eq. (18).

$$\Delta Q = Q_h - Q_c \quad (17)$$

$$PQ = \left(\frac{\Delta Q}{Q_c} \right) 100 \quad (18)$$

Heat lag is proportional to many parameters, though in the present case it is a strong function of the rate at which the hot fluid inlet temperature is increased. Heat lag may stabilize to a constant value if the span of the temperature ramp is long enough and the

ramping rate is low enough. Maximum heat lag generally occurs at the end of a ramp up procedure, where in the present case the hot fluid inlet temperature reaches 910 °K. A maximum stress and perhaps plastic strain is speculated to be present at or near this time.

Damaging thermal stress can also exist when the ramp procedure is complete and when thermal transients have ceased. The severity of thermal stress during steady state operation is largely proportional to heat exchanger compactness and pressure drop. As compactness is increased, steady state thermal stress is generally increased due to more severe thermal gradients. As pressure drop requirements decrease, flow length is generally decreased, which is also accompanied by more severe thermal gradients. Higher thermal stress during steady state gives way to increased creep damage.

An approach recently adopted in plate-fin heat exchanger design used to counter the effects of excessive thermal gradients is that of non-monolithic heat exchanger core structures. These techniques are intended to alleviate thermal stress during transient and steady state operation. A core that can expand and contract with more freedom can better accommodate rapid transient, high performance, and or high temperature (925 °K – 1175 °K) operation, Child et al. (1999) and Abiko et al. (2003). However, cyclic damage due to transient operation and creep will ultimately lead to cracks in heat exchanger components, eventually resulting in failure. A gas turbine heat exchanger is generally considered to have reached failure when the leakage rate of either fluid deteriorates to about 0.1 %, Sanders and Louie (1999). Nonetheless, when slow ramping rates are employed, transient operation damage is minimized allowing increased heat exchanger performance goals.

Thermal Stress Simulation

Data from the two previous models, namely the Fine Filter model and the Transient Thermal Simulation model, provided sufficient basis to calculate thermal stress in heat exchanger partition plates. This analysis was performed using the finite element analysis software ANSYS University Advanced, Release 8.1 (Swanson Analysis Systems Inc., Canonsburg, PA). The general element formulation used by ANSYS is based on the principle of virtual work (PVW). The PVW states that a virtual or very small change of the internal strain energy must be offset by an identical change in external work due to the applied loads, Snider (1979). Using the PVW, a simultaneous set of linearized equations having displacements as primary unknowns can be derived, beginning with the following form of the PVW governing equation:

$$\int \sigma_{ij} \delta e_{ij} dV = \int f_i^B \delta u_i dV + \int f_i^S \delta u_i dS \quad (19)$$

where σ_{ij} is the Cauchy stress component, δ the variation operator or virtual operator, e_{ij} the deformation tensor, u_i the displacement, x_i the current coordinate, f_i^B the component of body force, f_i^S the component of surface traction, V the volume of deformed body, and S is the surface of deformed body. The internal virtual work can be presented as:

$$\delta W = \int \sigma_{ij} \delta e_{ij} dV \quad (20)$$

where W is internal virtual work. The linearized set of simultaneous equations can be obtained by differentiating virtual work, Bonet and Wood (1997), and Gadala and Wang (1999):

$$D \delta W = \int D \sigma_{ij} \delta e_{ij} dV + \int \sigma_{ij} D \delta e_{ij} dV + \int \sigma_{ij} \delta e_{ij} D dV \quad (21)$$

In element formulation, material constitutive law has to be used to create the relation between stress increment and strain increment. The constitutive law only reflects the stress increment due to straining. However, the Cauchy stress is affected by the rigid body rotation and is not frame invariant. Therefore, an objective stress must be applied in the constitutive law. In this formulation, the Jaumann rate of Cauchy stress as described by McMeeking and Rice (1975) will be used:

$$\frac{\partial}{\partial t} \sigma_{ij}^J = \frac{\partial}{\partial t} \sigma_{ij} - \sigma_{ik} \frac{\partial}{\partial t} \omega_{jk} - \sigma_{jk} \frac{\partial}{\partial t} \omega_{ik} \quad (22)$$

where the partial derivative of σ_{ij}^J with respect to time is the Jaumann rate of Cauchy stress and the partial derivative of ω_{ij} with respect to time is the spin tensor. Using the constitutive law, the stress change due to straining can be expressed as:

$$\frac{\partial}{\partial t} \sigma_{ij}^J = c_{ijkl} d_{kl} \quad (23)$$

where c_{ijkl} is the material constitutive tensor, d_{ij} is the rate of deformation tensor, and v_i is the velocity. Substituting Eq. (23) into Eq. (22) and rearranging terms, the Cauchy stress rate can be shown as:

$$\frac{\partial}{\partial t} \sigma_{ij} = c_{ijkl} d_{kl} + \sigma_{ik} \frac{\partial}{\partial t} \omega_{jk} + \sigma_{jk} \frac{\partial}{\partial t} \omega_{ik} \quad (24)$$

From Eq. (24), the stress differentiation can be derived as:

$$D \sigma_{ij} = C_{ijkl} D e_{kl} + \sigma_{ik} D \omega_{jk} + \sigma_{jk} D \omega_{ik} \quad (25)$$

The differentiation of ωV is:

$$D (dV) = \frac{\partial}{\partial x_k} D u_k dV = D e_v dV \quad (26)$$

where e_v is equal to e_{ii} . Substitution of Eq. (25) and Eq. (26) into Eq. (21) yields:

$$\begin{aligned} D \delta W = & \int \delta e_{ij} C_{ijkl} D e_{kl} dV \dots \\ & + \int \sigma_{ij} \left[\left(\frac{\partial}{\partial x_i} \delta u_k \right) \left(\frac{\partial}{\partial x_j} D u_k \right) - 2 \delta e_{ik} D e_{kj} \right] dV \dots \\ & + \int \delta e_{ij} \sigma_{ij} \left(\frac{\partial}{\partial x_k} D u_k \right) dV \end{aligned} \quad (27)$$

The third term in Eq. (27) is usually insignificant so it is ignored. The final pure displacement formulation is:

$$\begin{aligned}
D \delta W = & \int \delta e_{ij} C_{ijkl} D e_{kl} dV \dots \\
& + \int \sigma_{ij} \left[\left(\frac{\partial}{\partial x_i} \delta u_k \right) \left(\frac{\partial}{\partial x_j} D u_k \right) - 2 \delta e_{ik} D e_{kj} \right] dV
\end{aligned} \tag{28}$$

Assuming all variables are known at time t ; the simultaneous set of linearized equations obtained from Eq. (28) are used to obtain the solution at time $t + \Delta t$. The updated Lagrangian method can be applied to incrementally simulate geometric nonlinearities, which is included when specified by the user. The eight node brick element SOLID185 was used in this analysis, which uses the following shape functions:

$$\mathbf{u} = \frac{1}{8} \begin{bmatrix} u_i (1-s)(1-t)(1-r) + u_j (1+s)(1-t)(1-r) + u_k (1+s)(1+t)(1-r) \dots \\ + u_L (1-s)(1+t)(1-r) + u_M (1-s)(1-t)(1+r) + u_N (1+s)(1-t)(1+r) \dots \\ + u_O (1+s)(1+t)(1+r) + u_P (1-s)(1+t)(1+r) \end{bmatrix} \tag{29}$$

$$\mathbf{v} = \frac{1}{8} [v_i (1-s) \dots (\text{Analogous to } u)] \tag{30}$$

$$\mathbf{w} = \frac{1}{8} [w_i (1-s) \dots (\text{Analogous to } u)] \tag{31}$$

There were two different thermal stress evaluations, namely the Low Temperature Heat Exchanger (LTHE) Thermal Stress model and the High Temperature Heat Exchanger (HTHE) Thermal Stress model. The main differences between these two models were the material of construction and operating temperature. The LTHE partition plates were taken as stainless steel 304 and the HTHE partition plates were taken as

solution-treated Inconel 625. Both thermal stress models consisted of a single heat exchanger partition plate having no fin connections or braze material, the same as in the Transient Thermal Simulation described previously. In contrast to the two dimensional Transient Thermal Simulation model, the thermal stress models were carried out in three dimensions. This was permitted because flow maldistribution was neglected, which stipulates that temperature is uniform along the width dimension.

Average material properties used in this analysis including elastic modulus (E), Poisson's ratio (ν), coefficient of thermal expansion (α), and density (ρ) are tabulated in Table 2. Both stainless steel 304 and solution-treated Inconel 625 partition plate materials were assumed to be isotropic, though E , ν , and α were programmed to include the effects of temperature dependence. Also tabulated in Table 2 are 0.2 % offset yield strengths for each material corresponding to the highest temperature that the respective heat exchanger partition plates will endure. Thus, it will be known if plastic damage occurs when the thermal stress results are obtained. It will be assumed for both materials that the 0.2% offset yield strengths tabulated in Table 2 apply to both tensile and compressive stresses.

Table 2. Partition Plate Material Properties

Material	E (GPa)	ν (---)	α ($1/^\circ\text{K}$)	ρ (kg/m^3)	Y_s (MPa)
SS 304	196	0.305	0.0000187	7900	130
IN 625	181	0.302	0.0000144	8442	255

In practice, heat exchanger partition plates endure stress due in part to differential gas pressures. However, FCGT systems typically have low gas pressure differentials so that

stress and creep affects due to this additional loading was neglected. To further justify this simplification, accounting for gas pressure differentials would require a detailed heat exchanger structure having well defined mechanical constraints. This was not the case, nor the focus for this work, so that stress due to differential thermal expansion was the only stress generating mechanism evaluated.

The partition plates in the thermal stress models were constrained with the least amount of mechanical restraints necessary to prevent rigid body rotation and translation. The mechanical restraints were placed such that the partition plate could expand freely in all directions X, Y, and Z, and also flex in any plane. The partition plates have reflective symmetry along their length dimension located at the center of the width dimension, so that only half of the plate was modeled through the use of symmetry boundary conditions.

A representative control volume for both Low Temperature Heat Exchanger (LTHE) and High Temperature Heat Exchanger (HTHE) thermal stress models is shown in Fig. 12. It can be seen in this figure that the outside corners are restricted against movement in the X-direction (which corresponds to the thickness dimension of the plate), the bottom center of the plate where the origin is located is restricted in the Y-direction (which corresponds to the length dimension of the plate), and the plane by which reflective symmetry applies is restricted in the Z-direction (which corresponds to the width dimension of the plate). The mesh was created manually (mapped) to correspond the rectangular mesh data produced in the Transient Thermal Simulation model. Thus,

temperature data were imported into ANSYS from the Transient Thermal Simulation model through the use of text (.txt) files.

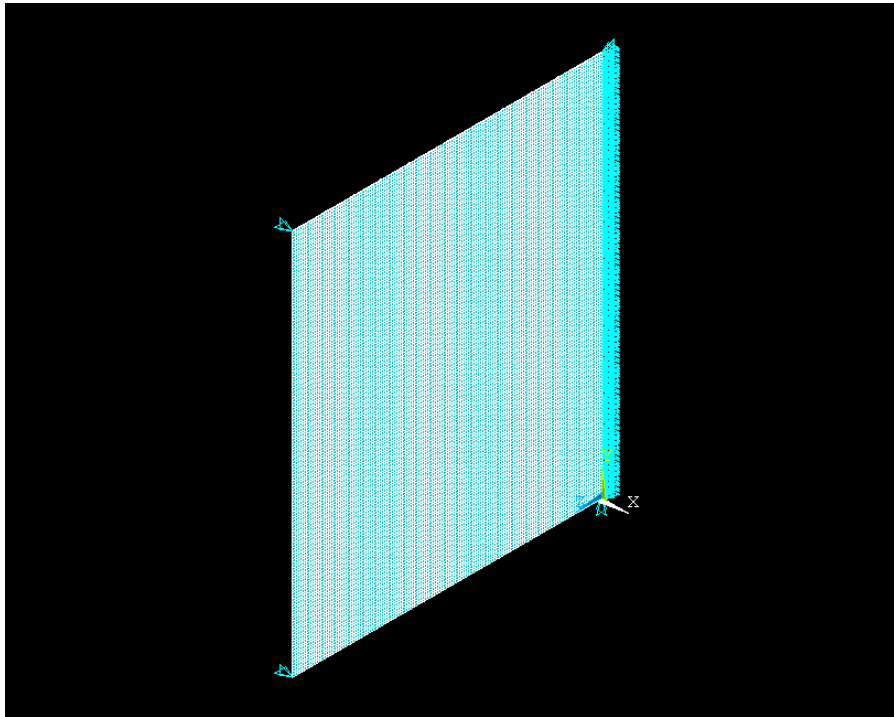


Fig. 12. Heat exchanger partition plate setup for thermal stress and creep calculation

The LTHERM Thermal Stress model was run for the partition plate geometry and heat exchanger process conditions described in the Transient Thermal Simulation section. Thermal stress in the LTHERM partition plate was calculated for the “before ramp” and “after ramp” steady states, as well as for several transient snapshots in time during the 30.0 °K/s temperature ramp procedure. The fastest ramping rate was chosen for the transient stress analysis to clearly distinguish the transient stress condition from the steady state stress condition.

The HTHE Thermal Stress model was run only for steady state operation, though for two different partition plates having variable width, namely High Temperature Heat Exchanger Case A (HTHECA) and High Temperature Heat Exchanger Case B (HTHECB). A high effectiveness ($\epsilon > 90\%$) counterflow heat exchanger was considered for the HTHE stress analysis since it is commonly sought after. The heat transfer coefficients and plate dimensions necessary to meet the steady state operating requirements of the HTHE were also calculated using the Fine Filter model. The heat transfer surface considered for both hot and cold fluid sides of the heat exchanger were geometrically scaled versions of the $\frac{1}{2}$ – 11.1 louver fin presented in Kays and London (1984).

The HTHE partition plate was taken as solution-treated Inconel 625 and considered to have an average and constant thermal conductivity of $19.3 \text{ W/m}\cdot\text{°K}$. The heat transfer coefficients for the HTHECA were calculated in the Fine Filter model to be $352.4 \text{ W/m}^2\cdot\text{°K}$ and $893.3 \text{ W/m}^2\cdot\text{°K}$ for the hot and cold fluid sides respectively. The HTHECA dimensions were calculated to be $23.7 \text{ cm} \times 25.4 \text{ cm} \times 0.0381 \text{ cm}$ (Length x Width x Thickness). The heat transfer coefficients for the HTHECB were almost identical to that of HTHECA, which were calculated to be $353.3 \text{ W/m}^2\cdot\text{°K}$ and $895.5 \text{ W/m}^2\cdot\text{°K}$ for the hot and cold fluid sides respectively. The HTHECB dimensions were calculated to be $23.7 \text{ cm} \times 38.1 \text{ cm} \times 0.0381 \text{ cm}$ (Length x Width x Thickness). Thus, the major difference between HTHECA and HTHECB was the width dimension. The compactness of the flow passages of both High Temperature Heat Exchangers were assigned to be $1204 \text{ m}^2/\text{m}^3$ and $3612 \text{ m}^2/\text{m}^3$ on the hot fluid and cold fluid sides

respectively. Stress was calculated twice for each candidate High Temperature Heat Exchanger partition plate, before and after a 300 hour creep process.

Creep Law Formulation

As mentioned in the previous section, creep behavior in the heat exchanger partition plates was modeled for both HTHE cases for the course of a 300 hour cycle of operation; creep was not modeled in the LTHE partition plates. Creep of metallic materials is a highly empirical science. To increase creep modeling accuracy, ANSYS has 13 different creep laws that the user can choose from to emulate known experimental data. Temperature dependent creep law constants may be programmed into ANSYS to more accurately fit experimental creep data, however; the creep law constants cannot be programmed to have stress dependence. A time hardening primary creep law was used for both HTHE cases. This creep law was chosen based on the information obtained from an extensive literature review, which indicated that secondary creep may not even occur during a 300 hour cycle of operation given stress levels remain moderate. The time hardening law for modeling primary creep can be constructed through the combination of three separate functions. That is, separate functions of stress, time and temperature as shown in Eq. (32):

$$\epsilon_c = f_1(\sigma) f_2(t) f_3(T) \quad (32)$$

The stress dependent function can be defined as shown in Eq. (33), which is commonly known as the Norton Power Law.

$$f_1(\sigma) = B_1 \sigma^n \quad (33)$$

Approximate values for the stress exponent n were found to take on a value of 5.8 for Inconel 625 at 925 °K having stress of 69.2 MPa to 102.3 MPa, Rodriguez et al. (2003), and 6.3 for Inconel 625 at 760 °K to 1090 °K at 105 MPa, Mathew et al. (2004). However, the Inconel 625 material analyzed by Mathew et al. (2004) was re-solution annealed after 60,000 hours of operation. Similarly, the Inconel 625 material analyzed by Rodriguez et al. (2003) was produced from cryomilled powder. Therefore, these alloys are only qualitatively the same as the commercially available Inconel 625, and as a result, the figures derived from these references may be used as approximate values only. Sufficient data necessary to construct a creep law for commercially available solution-treated Inconel 625 are currently unavailable.

The time dependent function can be defined as shown in Eq. (34), which is also known as the Bailey relation. It was found that the most common exponent m for polycrystalline metals is $1/3$, Feltham (1953).

$$f_2(t) = B_2 t^m \quad (34)$$

The temperature dependent function can be defined as shown in Eq. (35), which is commonly known as Arrhenius' Law. Rodriguez et al. (2003) gives an activation energy

for creep ΔH of 338 kJ/mole for Inconel 625 at 925 °K, as opposed to the commonly adopted activation energy of self diffusion in Ni which is 287 kJ/mole.

$$f_3(T) = B_3 e^{\left(\frac{-\Delta H}{R T}\right)} \quad (35)$$

Combining Eqs. (33), (34), and (35) yields Eq. (36), which represents primary creep with time hardening effects.

$$\varepsilon_c = \left(B_1 \sigma^n\right) \left(B_2 t^m\right) \left[B_3 e^{\left(\frac{-\Delta H}{R T}\right)}\right] \quad (36)$$

The derivative of Eq. (36) with respect to time yields an expression for creep rate as shown in Eq. (37), of which is shown in the form that ANSYS uses in Eq. (38).

$$\frac{\partial}{\partial t} \varepsilon_c = \left(B_1 \sigma^n\right) \left(B_2 m t^{m-1}\right) \left[B_3 e^{\left(\frac{-\Delta H}{R T}\right)}\right] \quad (37)$$

$$\frac{\partial}{\partial t} \varepsilon_c = C_1 \sigma^{C_2} t^{C_3} e^{\frac{-C_4}{T}} \quad (38)$$

Testing of the creep law constants C_1 through C_4 were accomplished by curve fitting the integrated form of Eq. (38) to the most pertinent experimental data found in the literature: Mathew et al. (2004), Stinton and Raschke (2004), and Boyer (1988). From this curve fitting exercise it was found that no gain would be made from programming

temperature dependence into any of the creep law constants. However, it was evident that stress dependence existed in the creep law constants C_1 and C_2 , where higher stress conditions warranted higher values for C_1 and or C_2 . As mentioned previously, the constants used to define creep behavior in ANSYS can be programmed with temperature dependence but they cannot have stress dependence. Therefore, constants C_1 and C_2 were modified from their physically meaningful values to those that would provide the best representation of creep behavior over the spectrum of anticipated stress. Constants C_3 and C_4 were determined using the physically meaningful arguments found in the literature, which correlated well with the experimental data. Apparent and Best Fit values for the creep law constants C_1 through C_4 are tabulated in Table 3.

Table 3. Creep Law Constants

Constant	Apparent Value	Best Fit Value
C_1	none	4.66E-02
C_2	5.8 to 6.3	1.65
C_3	-0.666	-0.666
C_4	40654.32	40654.32

Further, it was found that sheet stock thickness has a major effect on creep behavior, where thinner sheet stock will creep faster than thicker sheet stock, Stinton and Raschke (2004). It was assumed that the HTHE partition plate sheet stock (0.0381 cm thick) will creep more like bulk Inconel 625 material as opposed to Inconel 625 foil (less than 0.02 cm thick).

The experimental creep data from Mathew et al. (2004), Stinton and Raschke (2004), and Boyer (1988) were plotted against their respective creep law predictions as shown in

Fig. 13. Sets of identical symbols represent the empirical data and the lines represent predicted creep behavior. Each line is shown with a symbol at the end of it to indicate the test conditions and the empirical data that it corresponds to. The results show that the formulated creep law does not predict accurately for rapid creep rates (conditions with both high temperature and high stress), attributed mainly to the fact that stress dependent constants could not be used. However, legitimate creep behavior may be simulated with this equation, given that a creep strain of 0.15 % is not exceeded. It can be seen from Fig. 13 that the data from Stinton and Raschke (2004) have the worst curve fit of all the data presented. This is attributed to the fact that this experimental data set represents creep for sheet stock having a thickness of 0.0254 cm. Thus, it was considered acceptable that the prediction yields significantly less creep since the creep law was intended for 0.0381 cm thick sheet stock.

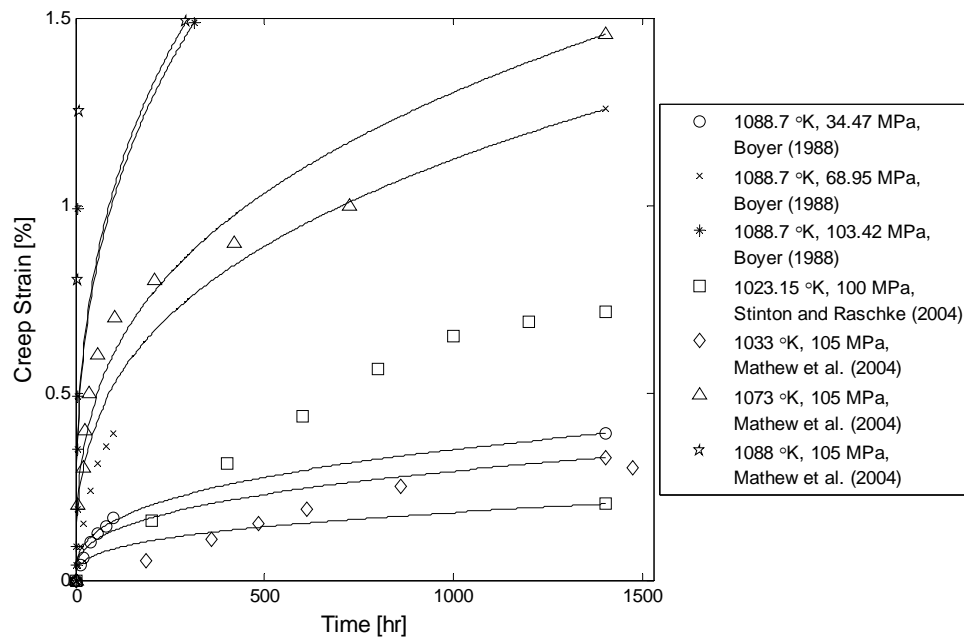


Fig. 13. Creep Fit Verification

CHAPTER 4

MODEL VALIDATION AND GRID INDEPENDENCE

Fine Filter Validation

The Fine Filter model was validated by reproducing heat exchanger design results published in Wang (2003). Most of the heat exchanger design results published in Wang (2003) were originally produced by Concepts Northern Research & Energy Corporation (Concepts NREC). In this work performed by Concepts NREC, a printed circuit heat exchanger was designed for high temperature operation (up to 1125 °K) having helium as the working fluid. Multiple core and header dimensions were evaluated in the Concepts NREC analysis. The Fine Filter model produced heat exchanger core dimensions that correlated well with the mentioned data. Fig. 14 is a plot of the published and Fine Filter model results, expressed as PCHE thermal density (including distributor volume) versus header width. Discrepancies between the published data and reproduced Fine Filter calculations are also shown in Fig. 14 via the dashed lines, which lie roughly between 1.5 – 2.0 % error.

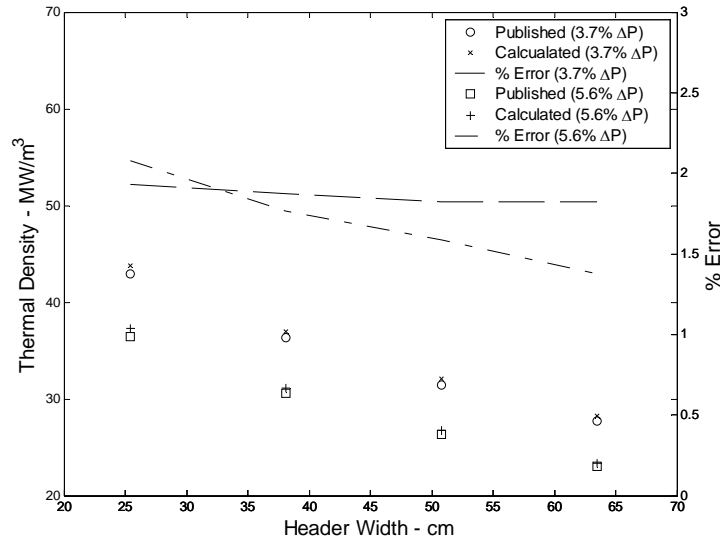


Fig. 14. Code Validation, Thermal Density versus Header Width

Transient Thermal Simulation Grid Test

The Transient Thermal Simulation code was tested systematically using various time increments and spatial resolutions. It was kept in mind that when spatial resolution is increased, the time increment must be decreased sufficiently when using the ADI method. Therefore, the effect of time increment size was tested first using the highest candidate spatial resolution of 101,250 nodes. The grid independency tests were carried out using the 30.0 °K/s ramp schedule to magnify the transient behavior of the problem setup.

The results show that a half-step time increment of 0.1 seconds was sufficient, as shown in hot and cold fluid outlet temperature profiles plotted in Fig. 15. Using the 0.1 second half-step time increment as a datum, the maximum percent difference of the hot and cold fluid outlet temperatures of this result compared with the 0.05 and 0.01 second half-step results are 0.79 % and 1.51 % for the hot side and 1.21 % and 2.46 % for the

cold side, respectively. Though not shown in graphical representation, the maximum percent difference of hot and cold side heat transfer rate results are 1.24 % and 3.01 % for the hot side and 3.50 % and 7.24 % for the cold side, respectively. It is also noted that the runtime using the 0.01 second half-step was approximately 4 hours, whereas the runtime using the 0.1 second half-step was under 1 hour.

The results in Fig. 16 show that a spatial resolution of 31,250 nodes was sufficient when using the 0.1 second half-step time increment. Using the 31,250 node result as a datum, the maximum percent difference of the hot and cold fluid outlet temperatures of this result compared with the 61,250 and 101,250 node results are 0.45 % and 0.98 % for the hot side and 0.71 % and 1.53 % for the cold side, respectively. Though not shown in graphical representation, the maximum percent difference of hot and cold side heat transfer rate results are 0.75 % and 1.65 % for the hot side and 2.02 % and 4.34 % for the cold side, respectively. Therefore, the final mesh parameters selected for this study were a half-step time increment of 0.1 seconds and a spatial resolution of 31,250 (125 by 250) nodes.

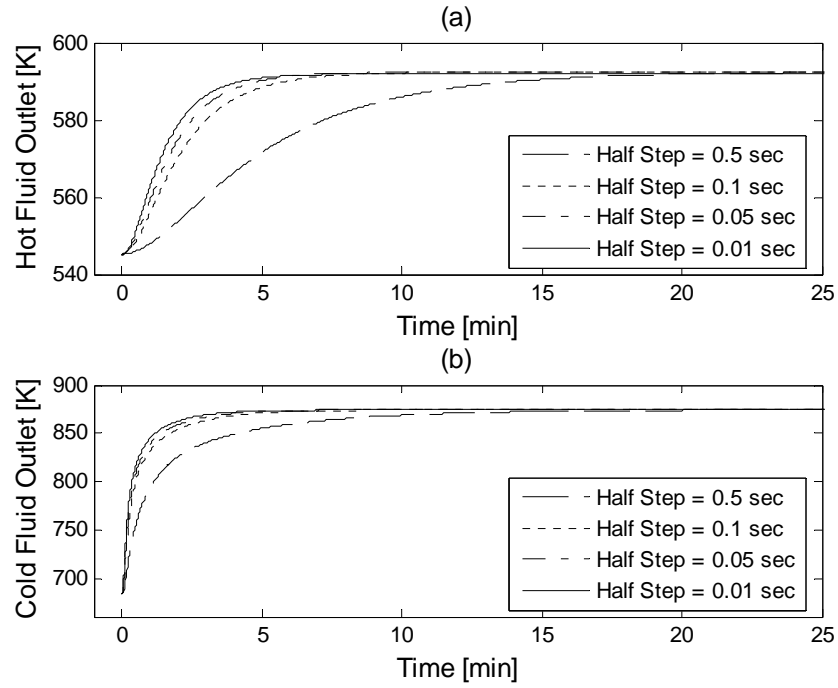


Fig. 15. Half-step time increment analysis: (a) Hot fluid outlet temperature
(b) Cold fluid outlet temperature

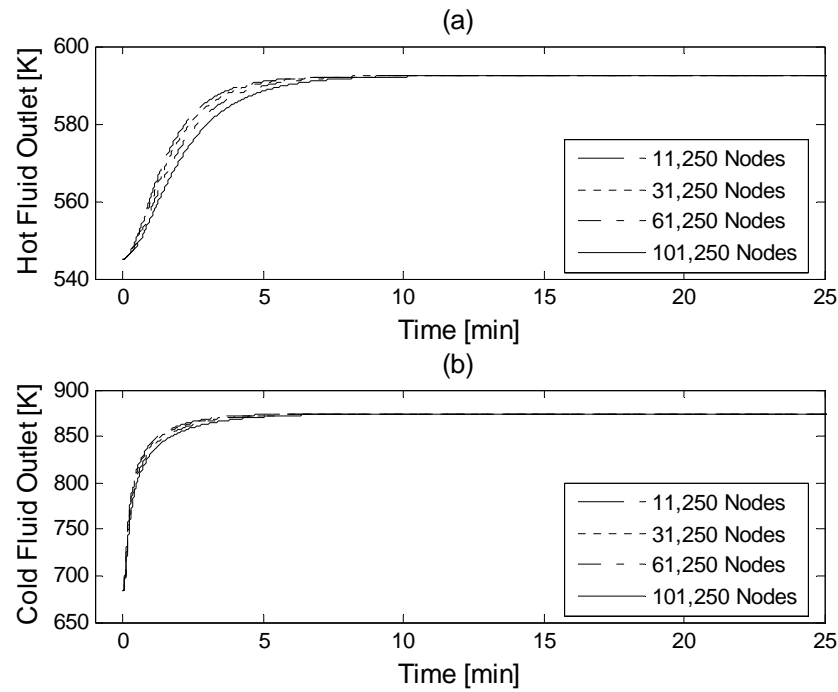


Fig. 16. Spatial increment analysis: (a) Hot fluid outlet temperature
(b) Cold fluid outlet temperature

Thermal Stress Grid Test

The grid resolution and number of initial load substeps used in both LTHER and HTHER thermal stress models were determined by testing the LTHER Thermal Stress model only, since they were very similar formulations. Determining the appropriate resolution for each spatial dimension was somewhat difficult. Two notable limitations arose when developing the mesh for this irregularly shaped control volume: (1) it is not recommended by ANSYS to exceed an aspect ratio of 20 for any two dimensions of the brick element, and (2) the University edition of ANSYS does not permit producing a model having more than 128,000 nodes. These factors made determining the appropriate grid resolution rather challenging, though a mesh having 104,000 nodes was found to produce consistent stress results in all three spatial dimensions.

Maximum and minimum component stress values were used to assess error between mesh densities as shown in Table 4 and Table 5. Since there was difficulty in obtaining a grid resolution that was clearly high enough, the highest grid resolution possible was used as a datum, namely 124,000 nodes. When using this datum it was found that 5 nodes across the thickness dimension of the partition plate were required to reproduce X Component stress values within acceptable error. It was recognized that the X-dimension has low stress levels in comparison to the Y and Z-dimensions. However, a sufficient number of nodes in the X direction was maintained (which requires many more nodes in the Y and Z-dimensions due to aspect ratio limits) since the extent to which the analysis would be changed by reducing node density in X-dimension was not known. Creep can take place in all three spatial dimensions even if it is initiated through a load originating

in only one dimension. Further, there was a significant temperature gradient across the thickness or X-dimension due to heat propagating through the partition plate. Thus, it was decided to maintain a dense grid in all spatial dimensions until a coarse grid is tested and verified to produce consistent results. Similar to the Transient Thermal Simulation grid independence tests, the appropriate spatial resolution was developed while using an excessive number of initial load substeps, which is synonymous with using a small time increment. Once the spatial resolution was chosen, the initial number of load substeps was reduced to an optimal amount. This was based mostly on the model's runtime, which was roughly 4 hours.

Table 4. Tensile Stress Grid Sensitivity

Stress Description	124800 nodes	104000 nodes	87000 nodes	71500 nodes
	Max Stress (MPa)	% Error	% Error	% Error
X Component	4.369	2.650	18.206	26.285
Y Component	69.182	0.046	0.035	0.166
Z Component	95.615	0.047	0.183	0.728
XY Shear	0.357	2.775	14.832	21.523
YZ Shear	19.112	0.010	0.073	0.246
XZ Shear	0.519	1.779	8.748	24.962

Table 5. Compressive Stress Grid Sensitivity

Stress Description	124800 nodes	104000 nodes	87000 nodes	71500 nodes
	Min Stress (MPa)	% Error	% Error	% Error
X Component	-1.900	2.111	16.689	25.066
Y Component	-12.760	0.071	0.133	0.714
Z Component	-46.158	0.097	0.245	0.100
XY Shear	-0.142	24.458	24.486	24.902
YZ Shear	-17.602	0.011	0.074	0.227
XZ Shear	-0.445	1.177	42.645	36.293

In addition to spatial resolution and initial number of load substeps, linear and nonlinear solving procedures were tested. This showed that the iterative, nonlinear solution method was necessary. Temperature dependent properties including thermal expansion coefficient, elastic modulus, and Poisson's ratio were also tested. Each property was given a single constant value to begin with, the results of which were compared to the results when all three material properties were given temperature dependence. These linear and nonlinear material property cases yielded vastly different results from each other in terms of stress magnitude, but the stress contours were qualitatively the same.

The mechanical constraints in the X and Y-dimensions that prevented rigid body translation and rotation were also changed to various node positions to verify that they had no significant role in stress calculation. It was verified that they provided the function of preventing rigid body movement only, and that they did not affect stress calculations. Further, a no-load test, where the entire partition plate was given a single constant temperature, was also performed. This test produced the result of zero stress

throughout the partition plate as it is supposed to. It should also be noted that some problem formulations, whether they had different partition plate size or different temperature distributions, would not converge to a solution. In this case, the spatial resolution could be increased in either the Y or Z-dimension by 10 nodes to escape the peculiar conditions of non-convergence.

Creep Model Verification

When each HTHE thermal stress analysis was completed, the effects of creep were activated in the ANSYS model, which was then restarted to calculate creep behavior for the 300 hour cycle time. The initial time increment had only a small bearing on the consistency of creep results, but it did have a significant impact on computation runtime. Starting time increments of 0.1, 1, and 30 seconds were tested. It was found that the fastest computation was obtained using the 1 second initial time increment, which resulted in a creep model runtime of about 24 hours. It was assumed that the spatial resolution used in the thermal stress models was high enough to accurately predict creep behavior. Further, it was found that a creep strain of 0.15 % would not be exceeded, which verified by good margin that the material remained in the primary creep regime during the 300 hour creep cycle. Thus, the mathematical formulation and curve fit used to model creep remained valid.

CHAPTER 5

RESULTS AND DISCUSSION

Performance Comparison Method

The results of the Performance Comparison Method were divided into two categories, namely the Coarse Filter and Fine Filter. In the former case the heat exchangers were rated by using a set of predetermined design criteria such as compactness, durability, materials cost, etc. In the latter case the performance of the heat exchangers were evaluated based on the heat transfer and fluid flow characteristics.

Coarse Filter Elimination

Each CHEX type received a performance rating for each process condition and criterion. The rating scale was defined as a range from one to ten, where ten was the best score. Justifications of the ratings given consist of the following:

1. With exception to the FTE, compactness ratings for all FCGT process conditions were directly proportional to the compactness data in Table 1. The FTE discrepancy was based on the necessary flow orientation for high effectiveness.
2. Durability ratings were assigned according to a CHEX's potential to overcome creep and fatigue challenges. The assumptions made were as follows:
 - The BPFE can facilitate non-monolithic clamping techniques, Ingersoll-Rand (2001), as well as diffusion bonding, Deakin et al. (1999).
 - The FTE can have problems with tube vibrations, Fraas and Ozisik (1965).

- Diffusion bonding is used for ME assembly.
 - PSE durability decreases greatly above 925 °K.
 - The SE is currently under investigation based in part on its rugged durability.
3. Material Cost ratings were assigned based on the cost of raw material necessary to transfer one unit of heat. The assumptions made were as follows:
- Required material stock is relatively inversely proportional to compactness.
 - The FTE requires more expensive tube stock and generally has the most wasted material in its manufacture.
 - The ME requires relatively thick sheet stock for its flow channel etching process.
4. Manufacturability ratings were assigned based on the difficulties posed in fabrication. The assumptions made were as follows:
- The BPFE and FTE have offsetting characteristics of high parts count and relatively inexpensive fabrication due to a long production history.
 - The ME has relatively expensive fabrication due to a short production history and sophisticated assembly.
 - The PSE and SE both require a significant investment in preload machinery.
5. Availability ratings were assigned based on market status. The assumptions made were as follows:
- Competitive markets exist for The BPFE and FTE.
 - Fair markets exist for the ME, PSE and SE.
6. With exception to the SE and its desirable cleaning characteristics, Maintenance ratings were considered inversely proportional to Compactness ratings.

7. Applicability ratings were assigned based on CHEX attributes pertinent to the FCGT application. The assumptions made were as follows:

- A BPFE was designed in part for the FCGT application, Ingersoll-Rand (1997).
- The FTE is better suited for gas-liquid or high pressure ratio applications.
- The ME holds much promise for increased CHEX performance.
- Most PSE designs were designed for high pressure ratio engines with operating temperatures at or below 925 °K.
- Low compactness SE designs may not be conducive with the inherently low power density, high temperature fuel cell stacks.

Total scores were tallied for each CHEX type for each process condition by summing the products of corresponding weights and ratings, see Table 6 through Table 8. Table 6 indicates the two best CHEXs for the Fuel Preheat Exchanger process condition are the ME and BPFE, having a total score of 173 and 170, respectively. Despite the low effectiveness for the Fuel Preheat Exchanger condition and thus the option of using crossflow, it was not enough to make the FTE competitive. Similarly, the greatest attributes of the PSE and SE are claimed to be transient operation durability, a criterion that was considered less important than compactness for the FCGT application.

Table 6. Fuel Preheat Exchanger Selection

	Weight	BPFE	FTE	ME	PSE	SE
Compactness	5	7	3	10	4	2
Durability	4	8	8	10	10	10
Material Cost	3	8	4	9	10	6
Manufacturability	2	8	8	4	7	7
Availability	3	10	10	5	5	5
Maintenance	3	3	9	1	6	10
Applicability	3	10	5	10	7	8
	Total	170	147	173	158	151

Table 7 indicates the two best rated CHEXs for the Low Temperature Heat Exchanger process condition are the ME and BPFE, having a total score of 183 and 178, respectively. Given the high effectiveness or counterflow orientation generally sought for this process condition, the FTE was rated lower here than it was for the Fuel Preheat Exchanger process condition. The increase in durability requirements shortened the margin between the BPFE and the PSE, but not enough to offset the present emphasis on compactness.

Table 7. Low Temperature Heat Exchanger Selection

	Weight	BPFE	FTE	ME	PSE	SE
Compactness	5	7	1	10	4	2
Durability	5	8	8	10	10	10
Material Cost	3	8	4	9	10	6
Manufacturability	2	8	8	4	7	7
Availability	3	10	10	5	5	5
Maintenance	3	3	9	1	6	10
Applicability	3	10	5	10	7	8
	Total	178	145	183	168	161

Table 8 indicates that the two best rated CHEXs for the High Temperature Heat Exchanger process condition are the ME and BPFE, having a total score of 204 and 201, respectively. The margin at which the ME and BPFE are rated over the other CHEX's

for this process condition is much greater than when stainless steel is the material of construction, as it was for the Low Temperature Heat Exchanger. This implies that the compactness criterion has a compounding effect when expensive alloys are used. In summary, the two CHEX types to be analyzed further in the Fine Filter selection process are the BPFE and ME.

Table 8. High Temperature Heat Exchanger Selection

	Weight	BPFE	FTE	ME	PSE	SE
Compactness	5	7	1	10	4	2
Durability	5	8	8	10	5	10
Material Cost	5	7	1	8	10	5
Manufacturability	4	8	8	4	7	7
Availability	3	10	10	5	5	5
Maintenance	3	3	9	1	6	10
Applicability	3	10	5	10	7	8
	Total	201	154	204	177	182

Fine Filter Elimination

From the Fine Filter model, performances of plate-fin and microchannel surfaces were compared assuming a counterflow heat exchanger constructed with a particular surface. Comparison was accomplished by pitting the resultant thermal density and flow length of each heat exchanger with one another. Surface selection was based primarily on this performance capability. Given that complete data on heat exchanger surface geometries are limited, geometric similarity was used to extrapolate fin performance data to carry out the Fine Filter elimination process. In Fig. 17 through Fig. 21, the circle data points denote thermal density derived from existing heat transfer surfaces, and the asterisk data points denote thermal density derived from extrapolated heat transfer

surfaces via geometric similarity. Likewise, the diamond data points denote flow lengths derived from existing heat transfer surfaces, and the star data points denote flow lengths derived from extrapolated heat transfer surfaces. Each set of data was given a best representation via curve fitting, which were all plotted together for ultimate comparison in Fig. 22 through Fig. 24.

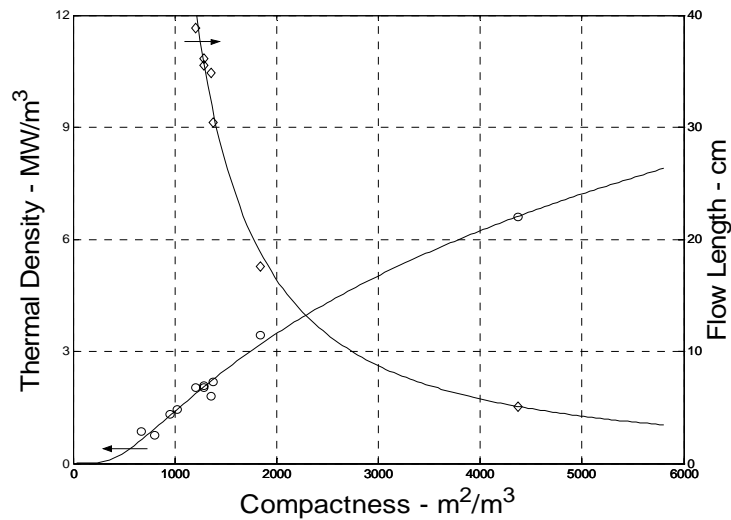


Fig. 17. Plain Fin Thermal Density versus Compactness

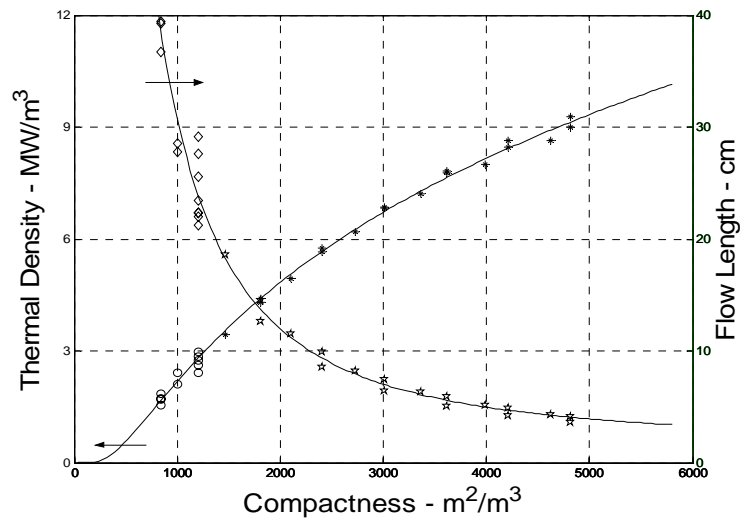


Fig. 18. Louver Fin Thermal Density versus Compactness

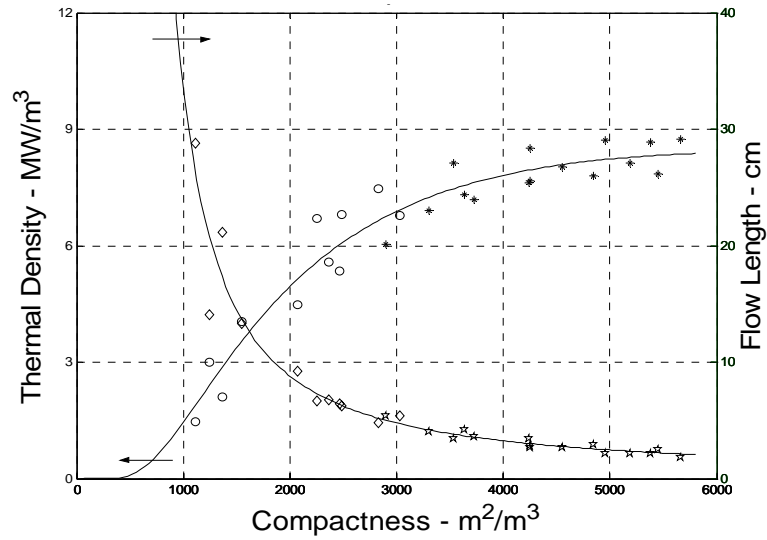


Fig. 19. Strip Fin Thermal Density versus Compactness

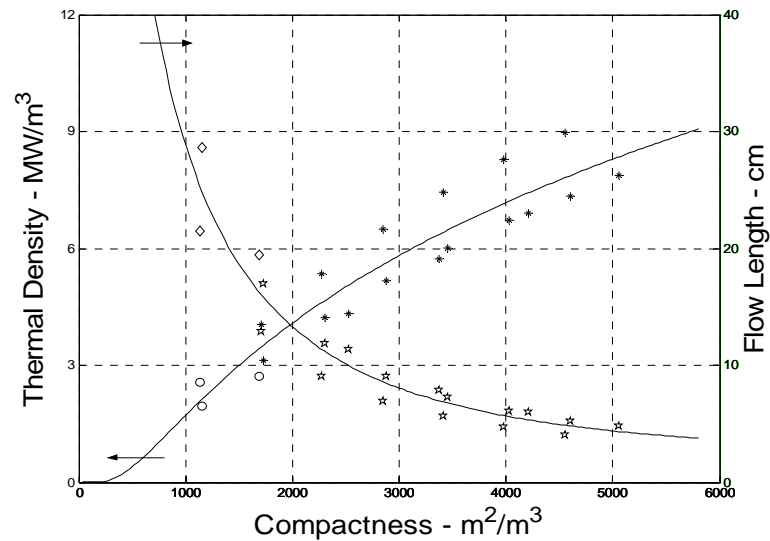


Fig. 20. Wavy Fin Thermal Density versus Compactness

Fig. 17 through Fig. 24 demonstrate the trivial concept that CHEX thermal density increases with increased compactness, but more importantly the results indicate which surface geometry can yield the highest core thermal density and longest flow length for a given level of compactness. As can be seen from Fig. 22, the louver fin can yield the

highest thermal density (lowest volume per unit heat duty) of all the candidate surface geometries. The louver fin was also found to have a competitive flow length for a given level of compactness as shown in Fig. 23. Fig. 24 is a comparison of curve fit representations of thermal density data versus flow length data.

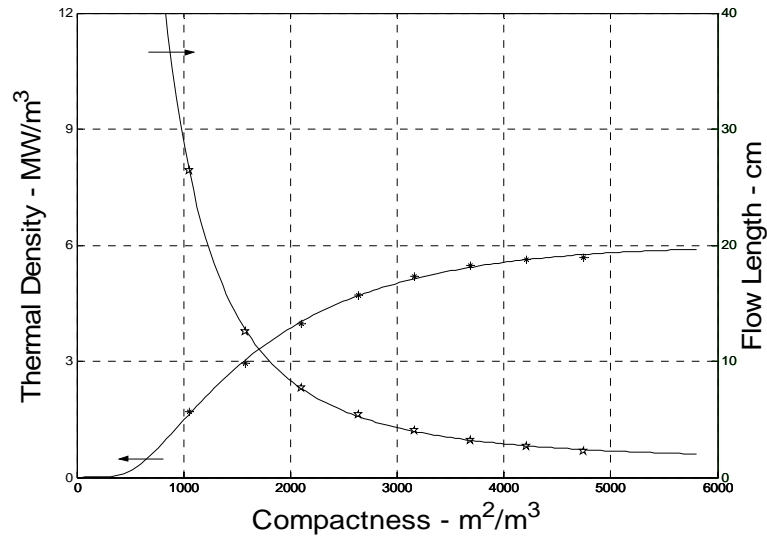


Fig. 21. Printed Circuit Thermal Density versus Compactness

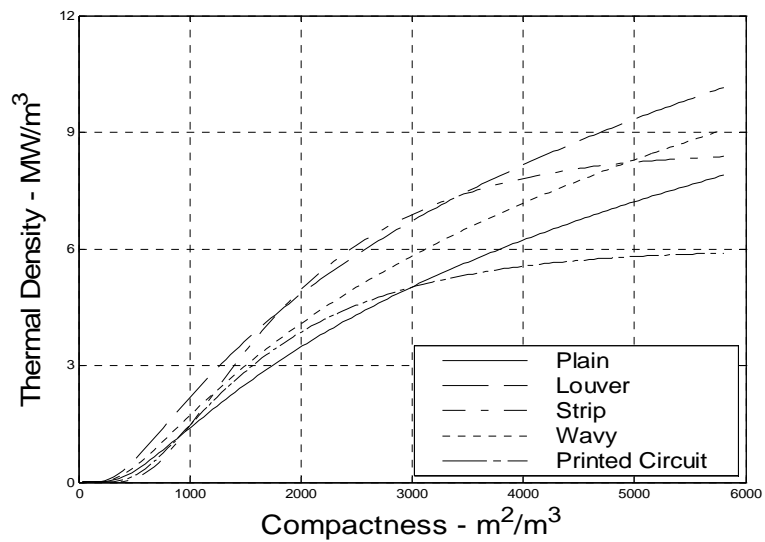


Fig. 22. Fin Comparison, Thermal Density versus Compactness

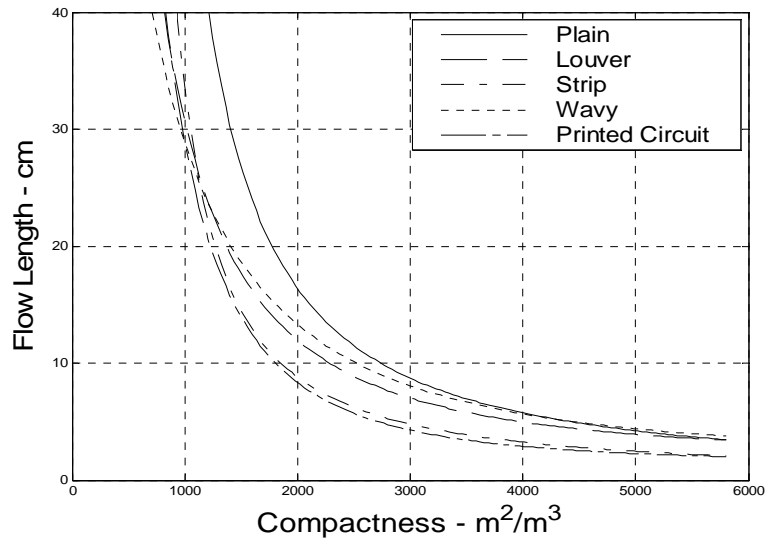


Fig. 23. Fin Comparison, Flow Length versus Compactness

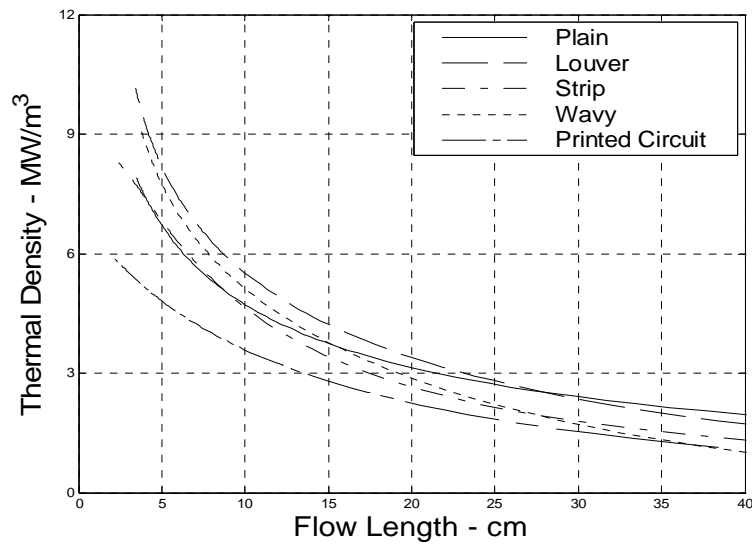


Fig. 24. Fin Comparison, Thermal Density versus Flow Length

It can be seen from Fig. 24 that the louver fin generally yields the longest flow length for a given thermal density. Having a longer flow length is important for two reasons. The first is that of cost, the shorter the flow length, the wider the partition plate needs to be or the more heat exchanger cells are required to meet a given heat duty. Both of these

repercussions are undesirable. When a partition plate becomes excessively wide, pressure losses in the core distributors become high; this breeds more problems such as flow maldistribution. Flow maldistribution can generate excessive temperature gradients and result in lower thermal performance and reduced service life. The alternative to widening the partition plate is to have more heat exchanger cells. When more heat exchanger cells are used it simply becomes a matter of excessive cost due to additional manufacturing and labor, in addition to increasing the number of weldments that could fail. Thus, when considering the performance analysis on the mentioned fin candidates, the louver fin has emerged as the most desirable having the best combination of attributes, which are long flow length and high thermal density.

In addition to the numerical results of the present analysis, the louver fin geometry has other desirable characteristics. The louver fin is formed by a relatively inexpensive rolling process, instead of by a reciprocating press necessary for the strip fin, which makes it much cheaper to produce, Hesselgreaves (2001). The louver fin is also amenable to non-monolithic structural designs used in modern plate-fin heat exchangers. Therefore, the plate-fin type heat exchanger having the louver surface geometry was found to be most compatible with hybrid FCGT process conditions. Using the fin performance data presented in Fig. 18, the heat transfer surfaces chosen for further analyses were geometrically scaled versions of the $\frac{1}{2}$ – 11.1 louver fin presented by Kays and London (1984).

Transient Thermal Simulation

The results of the temperature ramp analysis clearly show a heat lag between the hot fluid heat transfer rate to the metal and the metal heat transfer rate to the cold fluid during the transient process for all four ramping rates. Given the ramp schedule used in this analysis, heat lag (ΔQ) as defined in Eq. (17) stabilized to a constant value for the two slower ramping rates as shown in Fig. 25 and Fig. 26. The maximum and stabilized ΔQ for the 0.03 °K/s ramping rate was 5.3 Watts, corresponding to a percent heat (PQ) as defined in Eq. (18) of 0.8 %. The maximum and stabilized ΔQ for the 0.3 °K/s ramping rate was 57.2 Watts, corresponding to a PQ value of 5.4 %. Conversely, heat lag did not stabilize during the ramp up period for the two faster ramping rates as shown in Fig. 27 and Fig. 28. The maximum ΔQ for the 3.0 °K/s ramping rate was 355.5 Watts, corresponding to a PQ value of 35.5 %. The maximum ΔQ for the 30.0 °K/s ramping rate was 662.5 Watts, corresponding to a PQ value of 92.7 %. At the end of the 30.0 °K/s ramp rate period, the heat rate entering the hot fluid side of the partition plate was almost double than the heat rate exiting the cold fluid side of the plate.

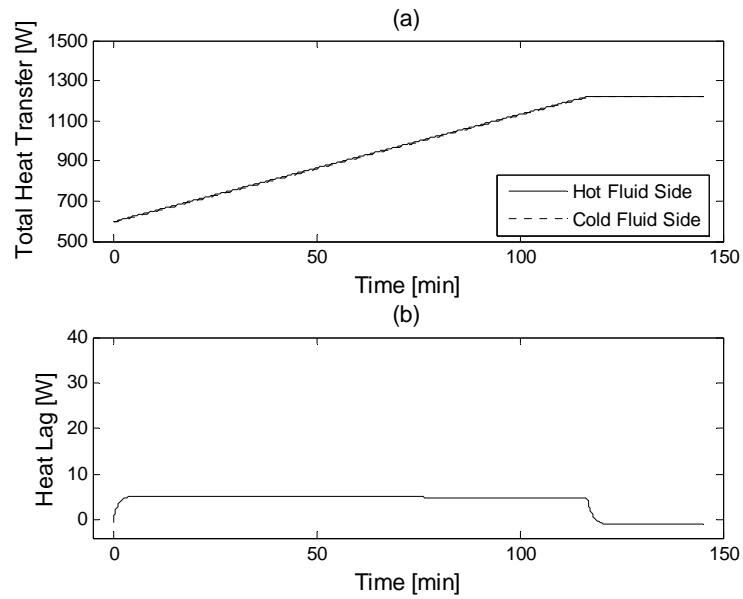


Fig. 25. Ramping rate of 0.03 °K/s: (a) Heat transfer to and from a single heat exchanger plate, (b) Heat lag

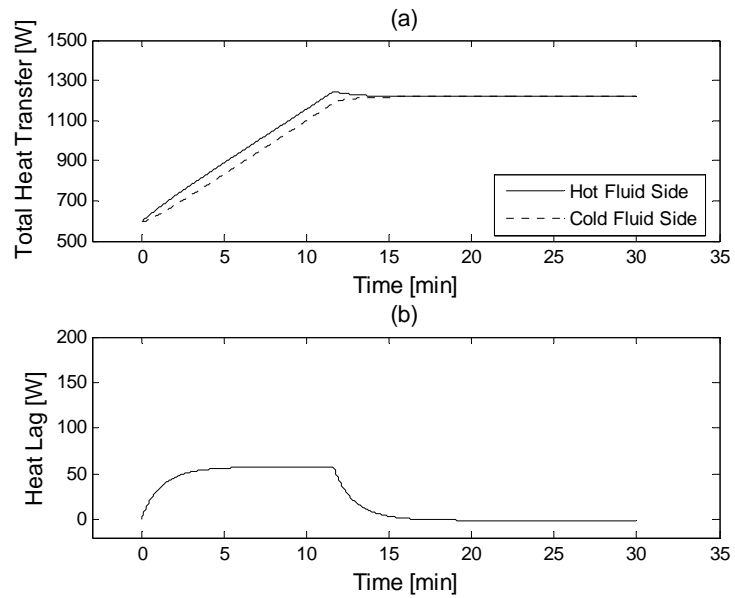


Fig. 26. Ramping rate of 0.3 °K/s: (a) Heat transfer to and from a single heat exchanger plate, (b) Heat lag

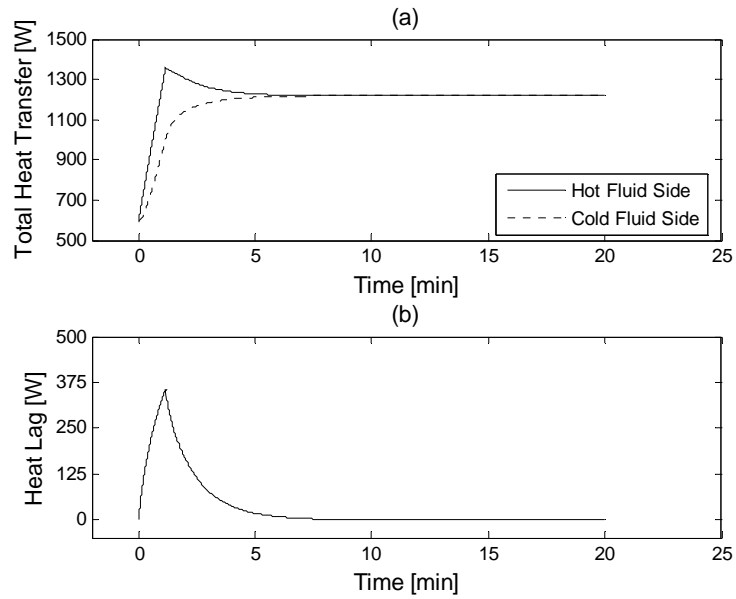


Fig. 27. Ramping rate of 3.0 °K/s: (a) Heat transfer to and from a single heat exchanger plate, (b) Heat lag

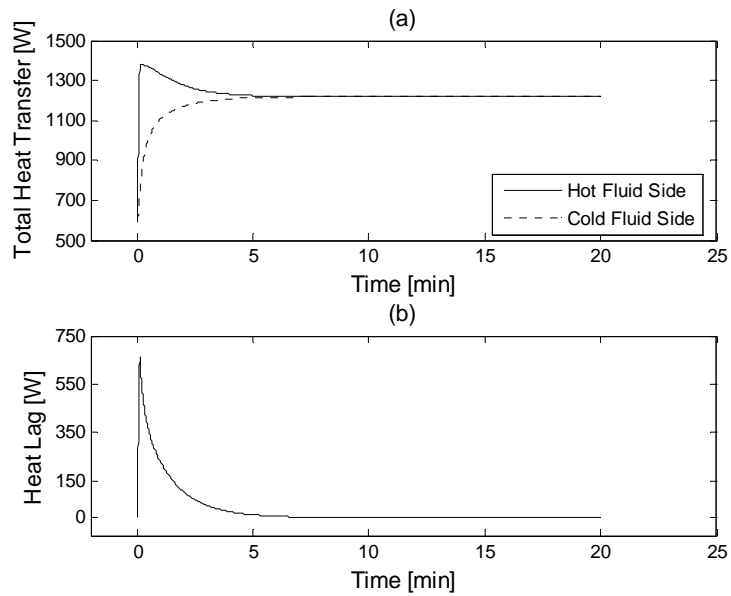


Fig. 28. Ramping rate of 30.0 °K/s: (a) Heat transfer to and from a single heat exchanger plate, (b) Heat lag

It was observed that the partition plate reached a steady thermal condition in roughly 7 minutes from the onset of the ramp schedule for the 3.0 °K/s and 30.0 °K/s ramp rate cases. Thus, the hot and cold fluid outlet temperatures calculated for these two cases were plotted in Fig. 29 for further comparison. This figure shows that the 30.0 °K/s ramping rate yields a marked increase in cold fluid outlet temperature when compared to the 3.0 °K/s ramping rate case, despite the fact that both of these cases require roughly the same amount of time to reach a steady thermal condition.

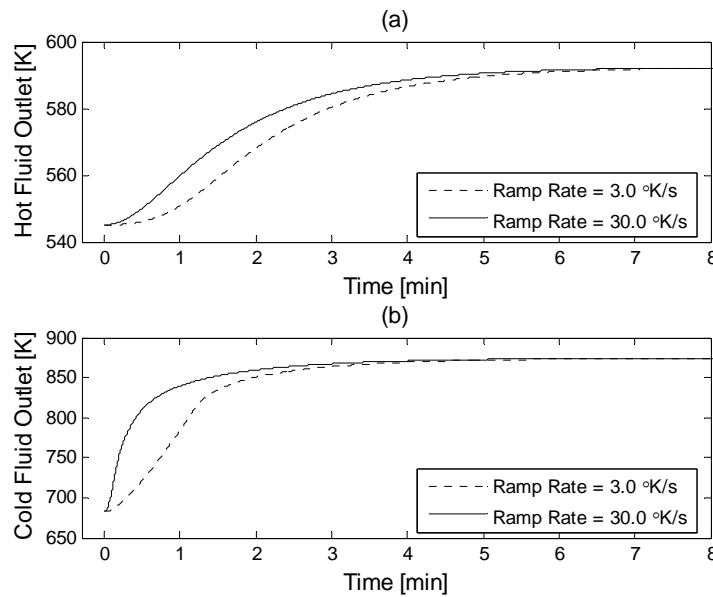


Fig. 29. Outlet temperatures for ramp rates 3.0 and 30.0 °K/s: (a) Hot side, (b) Cold side

Fig. 30 contains contour plots of the fluid and partition plate temperature profiles. Isotherms are labeled with their respective temperature values in degrees Kelvin. The length dimension of the plate is labeled on each contour plot, though the thickness dimension is not labeled for reasons of clarity. As mentioned previously, the thickness of

the plate is 0.0381 cm. Convection resistance between the fluids and plate can clearly be seen by the sharp increase in temperature shown by the isotherms. Fig. 30 (a) is a plot of temperature taken at the steady thermal condition derived after the ramp up procedure. It may be recalled that the ramp up procedure was defined as follows. The cold fluid inlet temperature was held constant at 500 °K throughout. The hot fluid inlet temperature was held at 700 °K until a steady thermal condition was obtained. The hot fluid inlet temperature was then ramped up linearly to the peak temperature of 910 °K and held until a steady thermal condition was again obtained. The end of the ramp up procedure was considered to be the point at which the hot fluid inlet temperature reached the peak temperature of 910 °K, where ΔQ was found to be at a maximum.

Fig. 30 (b) through Fig. 30 (e) consists of contour plots of temperature taken at the end of the ramp up process for each ramp rate case. It can be seen that at the end of the 0.03 °K/s ramp up process that the partition plate temperature profile is roughly the same as the steady state temperature profile. This suggests that increased plate damage due to transient operation at this rate is negligible or nonexistent for the 0.03 °K/s temperature ramping rate. It is also observed from Fig. 30 that the faster the ramping rate the further the plate is from a steady thermal state upon ramp completion. The 3.0 °K/s and 30.0 °K/s ramp rate cases clearly demonstrate transient thermal behavior; given that both have a notable concentration of isotherms at the hot fluid inlet end of the plate. These concentrations are thought to be indicative of transient thermal stress, and such conditions should be observed closely when predicting cyclic plate damage and ultimately heat exchanger service life.

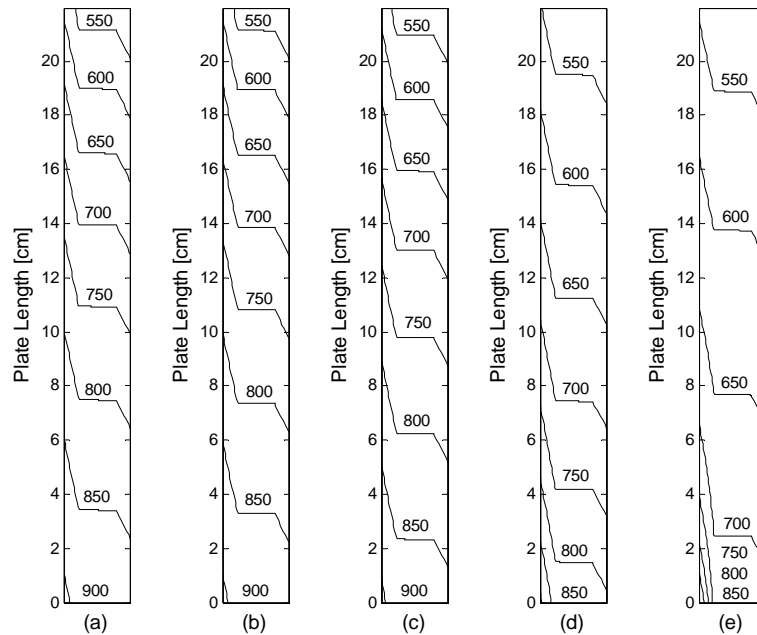


Fig. 30. Contour plot of temperature in the fluid and partition plate for: (a) steady state and (b) 0.03, (c) 0.3, (d) 3.0, and (e) 30.0 °K/s ramp rate cases

Thermal Stress Simulation

The following sections include thermal stress results calculated using ANSYS software for the LTHE and HTHE problem formulations. For the LTHE setup, thermal stress was calculated for the before ramp up state, after ramp up state or steady state, and at the most severe transient state for the 30.0 °K/s ramp rate case. For the HTHE setup, thermal stress was calculated for the variable width partition plate geometries HTHECA and HTHECB, at two different states namely before operation (before creep) and after 300 hours of operation (after creep). The qualitative nature of the stress contour plots for the LTHE before and after ramp up states, as well as the HTHE before creep states, were nearly identical with exception to the magnitude of the stresses. Therefore, a detailed

explanation of the thermal stress derived in the heat exchanger partition plates was made for the LTHE after ramp up state only, since it will be subject to discussion first.

Low Temperature Heat Exchanger Static Thermal Stress

To help visualize how thermal stress can be created in heat exchanger partition plates, an oblique view contour plot of temperature for the steady state LTHE is shown in Fig. 31, along with its corresponding thermal strain which was magnified by 100X. It can be observed from this figure that the hot fluid inlet end (the top) of the plate expands much more than the cold fluid inlet end (the bottom) of the plate, inducing non-uniform thermal expansion. This occurrence of non-uniform temperature within a single solid body will create thermal stress.

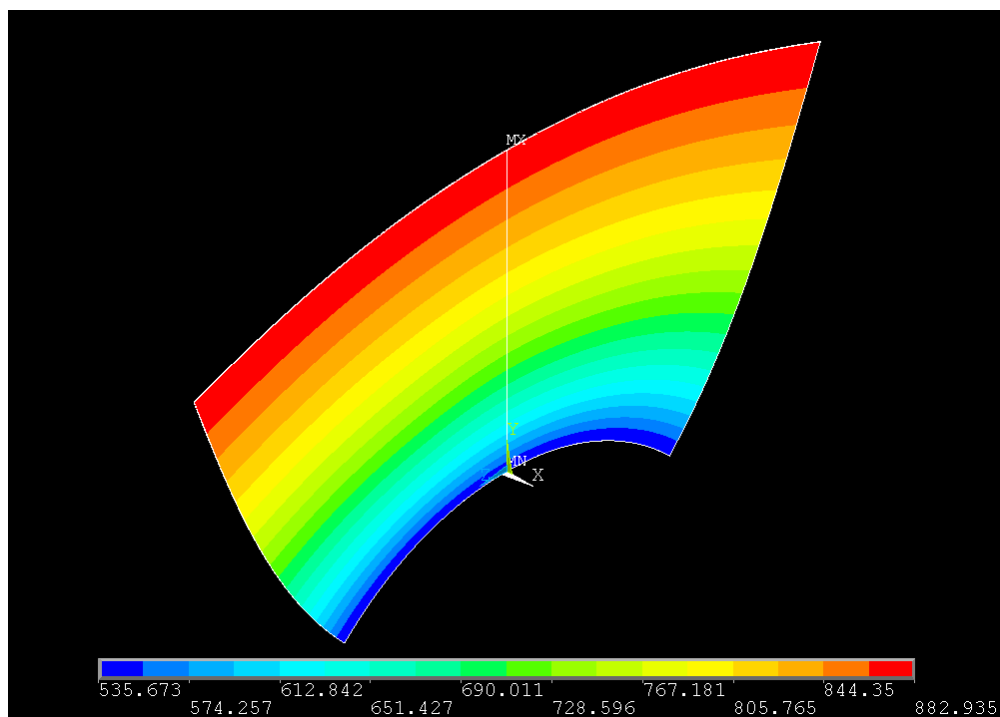


Fig. 31. Body Temperature and Magnified Strain in Steady State LTHE, ($^{\circ}$ K)

Thermal stress derived in the steady state LTHE plate shown in Fig. 31 can be explained through the use of two, four-bar linkage (FBL) idealizations. Consider the two FBLs superimposed on the plan view of the steady state LTHE shown in Fig. 32. These linkages represent half of the LTHE partition plate, where again, this is adequate since reflective symmetry applies to this problem formulation. In Fig. 32, all linkage bars are at the same temperature, which is equal to the partition plate reference temperature of 705 °K. In Fig. 33, the linkage bars are considered to be at the steady state LTHE operating temperature, and are shown with their thermal strain magnified by 100X.

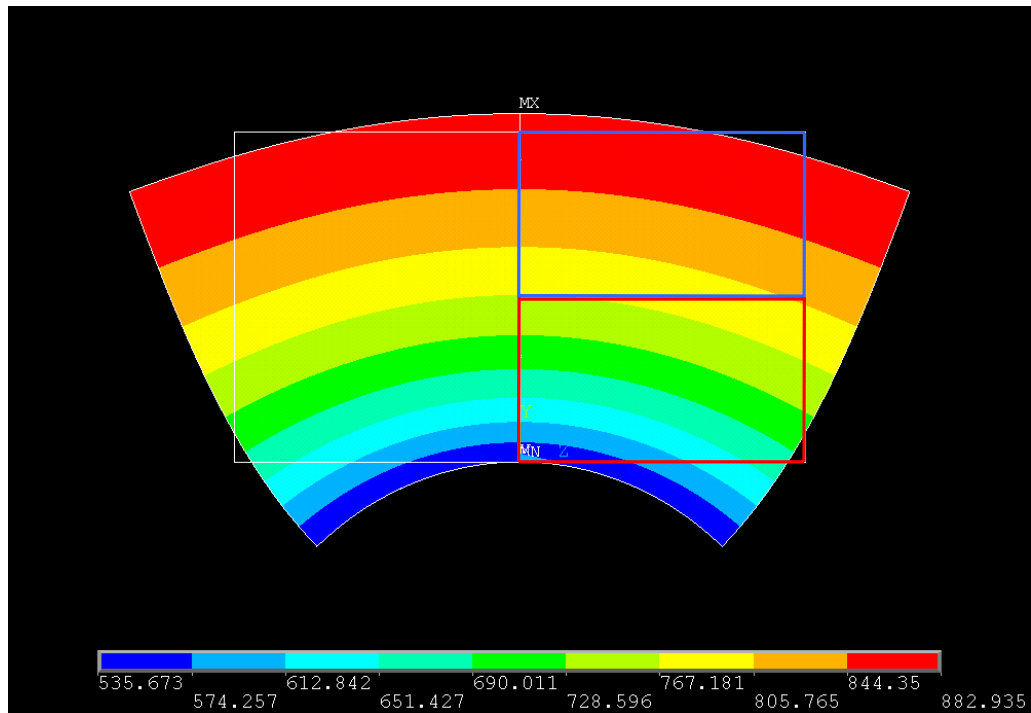


Fig. 32. Steady State LTHE Four-Bar Linkages at Reference Temperature, (°K)

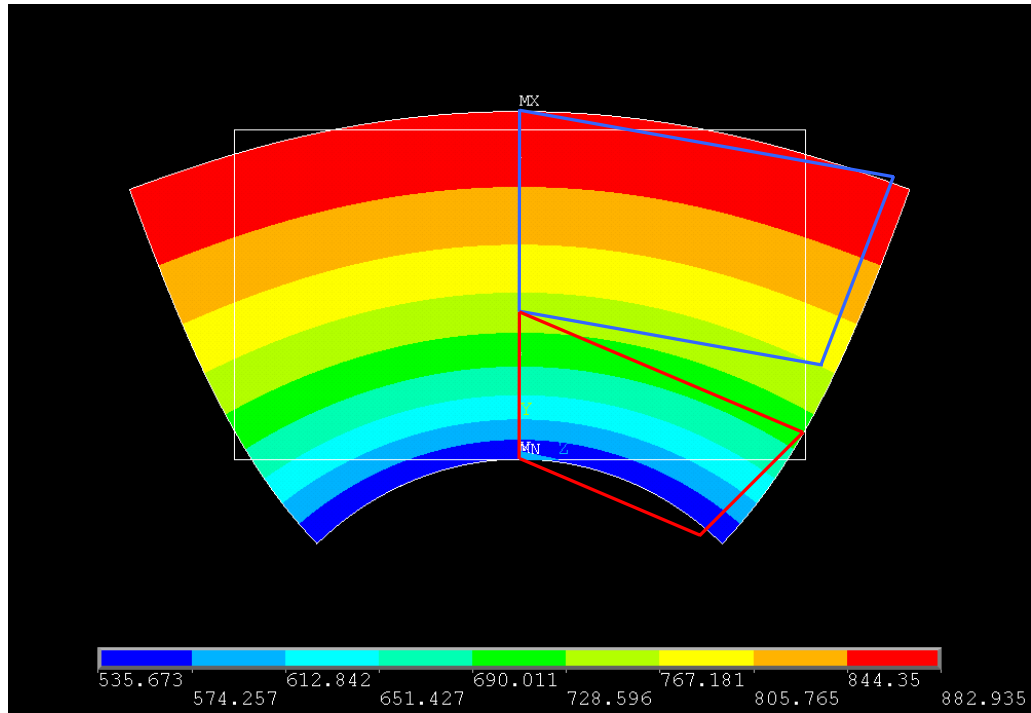


Fig. 33. Steady State LTHE Four-Bar Linkages at Operating Temperature, ($^{\circ}\text{K}$)

The angles within the FBLs shown in Fig. 33 were found using a system of 9 equations and 9 unknowns. Given all four new bar lengths A, B, C, and D as shown in Fig. 34, the equations needed to determine the angles within the FBL are listed as Eqs. (39) through (47).

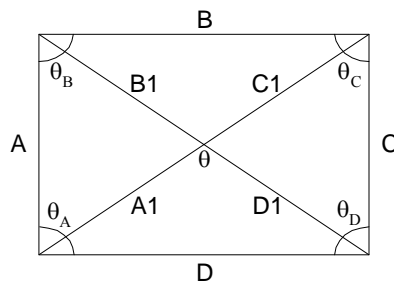


Fig. 34. Four Bar Linkage Representation

$$\frac{1}{2} (D1 + B1) (C1 + A1) \sin(\theta) = \frac{1}{4} \sqrt{4 (B1 + D1)^2 (A1 + C1)^2 - (A^2 + C^2 + D^2 - B^2)^2} \quad (39)$$

$$\cos(\theta) = \frac{A1^2 + D1^2 - D^2}{2 A1 D1} \quad (40)$$

$$\cos(\theta) = \frac{B1^2 + C1^2 - B^2}{2 B1 C1} \quad (41)$$

$$\cos(180 \text{ deg} - \theta) = \frac{A1^2 + B1^2 - A^2}{2 A1 B1} \quad (42)$$

$$\cos(180 \text{ deg} - \theta) = \frac{C1^2 + D1^2 - C^2}{2 C1 D1} \quad (43)$$

$$\theta_A = \text{acos}\left(\frac{1}{2} \frac{D^2 + A1^2 - D1^2}{A1 D}\right) + \text{acos}\left(\frac{1}{2} \frac{A^2 + A1^2 - B1^2}{A1 A}\right) \quad (44)$$

$$\theta_B = \text{acos}\left(\frac{1}{2} \frac{A^2 + B1^2 - A1^2}{B1 A}\right) + \text{acos}\left(\frac{1}{2} \frac{B1^2 + B^2 - C1^2}{B1 B}\right) \quad (45)$$

$$\theta_C = \text{acos}\left(\frac{1}{2} \frac{B^2 + C1^2 - B1^2}{B C1}\right) + \text{acos}\left(\frac{1}{2} \frac{C1^2 + C^2 - D1^2}{C1 C}\right) \quad (46)$$

$$\theta_D = \text{acos}\left(\frac{1}{2} \frac{C^2 + D1^2 - C1^2}{C D1}\right) + \text{acos}\left(\frac{1}{2} \frac{D1^2 + D^2 - A1^2}{D1 D}\right) \quad (47)$$

It was observed that the magnified strain contour plot of the LTHE partition plate shown in Fig. 33 takes on a very similar geometry to that of the magnified strain FBL overlays, indicating a valid simulation was obtained with the LTHE Thermal Stress model. Note that the bar common to both upper and lower FBLs does not overlap itself as it did when the FBLs were at the uniform reference temperature. The separation of these bars implies that there will be tension along the length edge of the partition plate, and opposing stresses, or compression at the center of the partition plate.

Fig. 35 is a contour plot of Y Component thermal stress for the LTHE steady state condition. In this figure and in all subsequent partition plate contour plot figures, the hot fluid inlet end of the plate refers to the top end of the plate and the cold fluid inlet end of the plate refers to the bottom end of the plate. Further, at the center of the bottom end of the plate lays the origin, where the Y dimension extends upward along the length of the plate, the X dimension extends into the thickness of the plate, and the Z dimension extends laterally along the width dimension of the plate.

As predicted from the FBL idealization, Fig. 35 shows that Y Component tension indeed exists along the length edges of the plate, and that compression exists in the center region of the plate. Fig. 36 is a contour plot of Z Component thermal stress for the LTHE steady state condition. A similar FBL explanation may be made for this contour plot, where it too is in a state of tension along the width edges and compression in the center region. The maximum Y and Z Component stresses in the LTHE partition plate do not induce plastic strain during steady state operation, but are significant in reaching 69.2 MPa and 95.7 MPa respectively. In these figures and all subsequent partition plate

contour plot figures, the symbols MX and MN denote the locations of the maximum and minimum values of that respective contour plot.

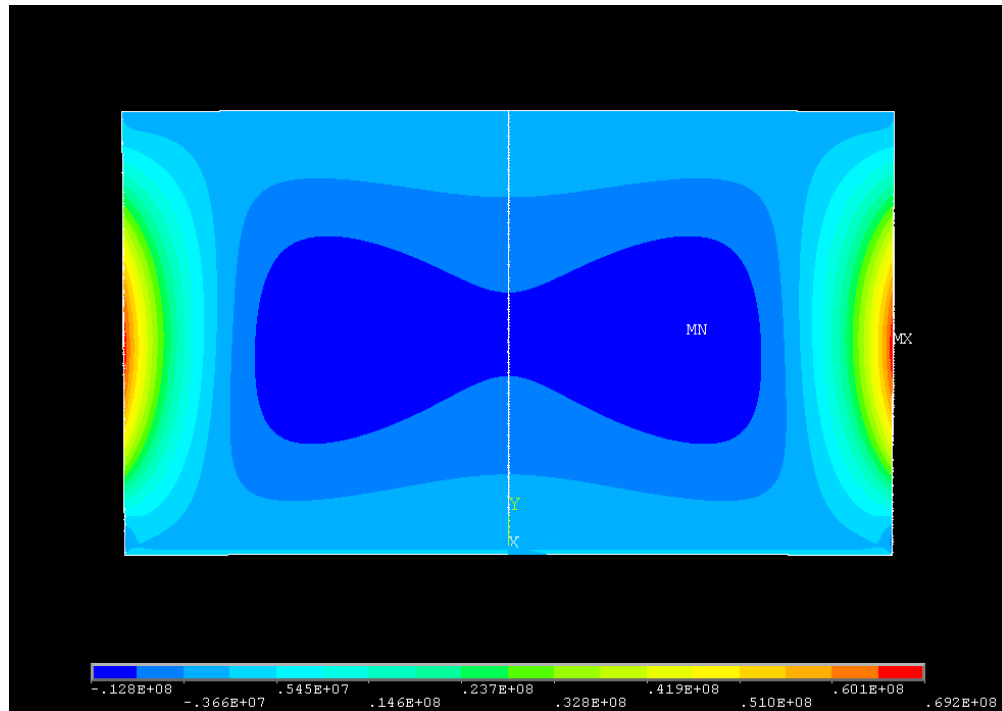


Fig. 35. Y Component Stress in Steady State LTBE, (Pa)

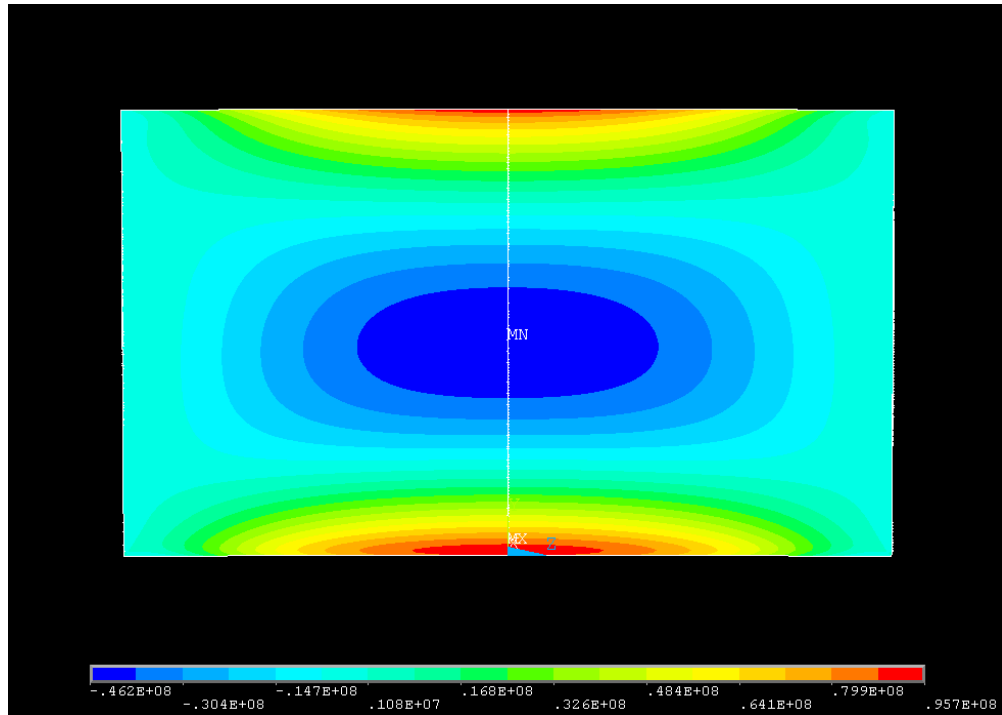


Fig. 36. Z Component Stress in Steady State LTHE, (Pa)

Fig. 37 is a contour plot of YZ Shear stresses for the LTHE steady state condition; note that the minimum shear stresses (indicated by the large negative value as shown in the legend) are located near the corners of the hot fluid inlet end of the plate, and that the maximum shear stresses (indicated by the large positive value as shown in the legend) are located near the corners of the cold fluid inlet end of the plate. The X Component, XY Shear, and XZ Shear stress contour plots were omitted since they were found to have insignificant levels of stress when compared to the contour plots shown herein. Omission of these insignificant stress contour plots applies for all subsequent thermal stress and creep strain discussions. A contour plot of Von Mises Equivalent stress, often considered the most telling contour plot of stress, is shown in Fig. 38 for the LTHE steady state condition.

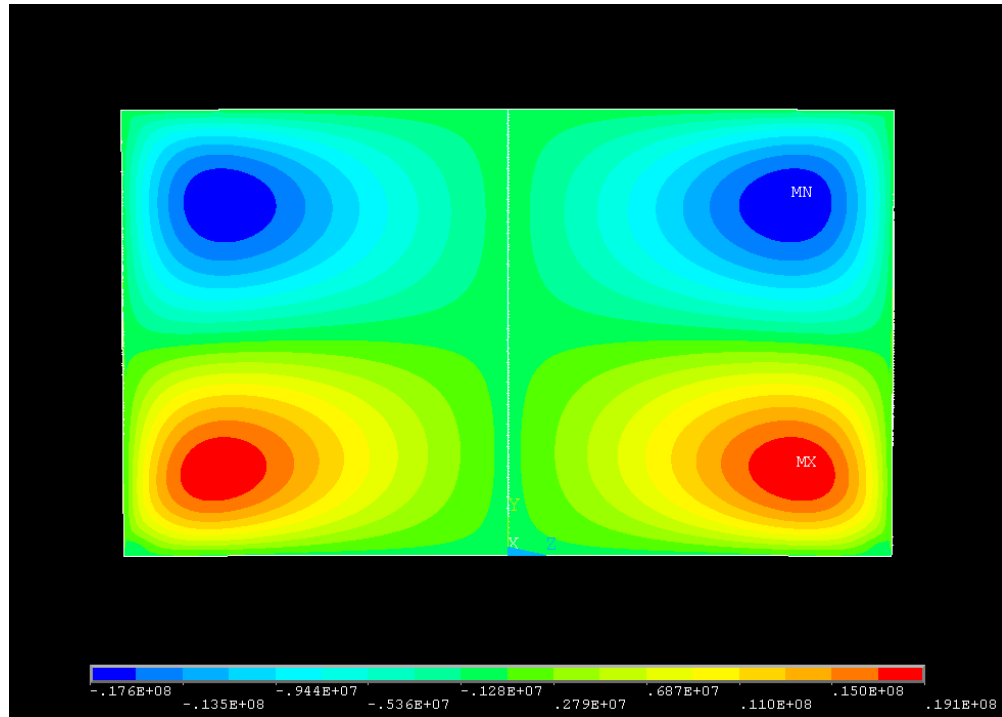


Fig. 37. YZ Shear Stress in Steady State LTHE, (Pa)

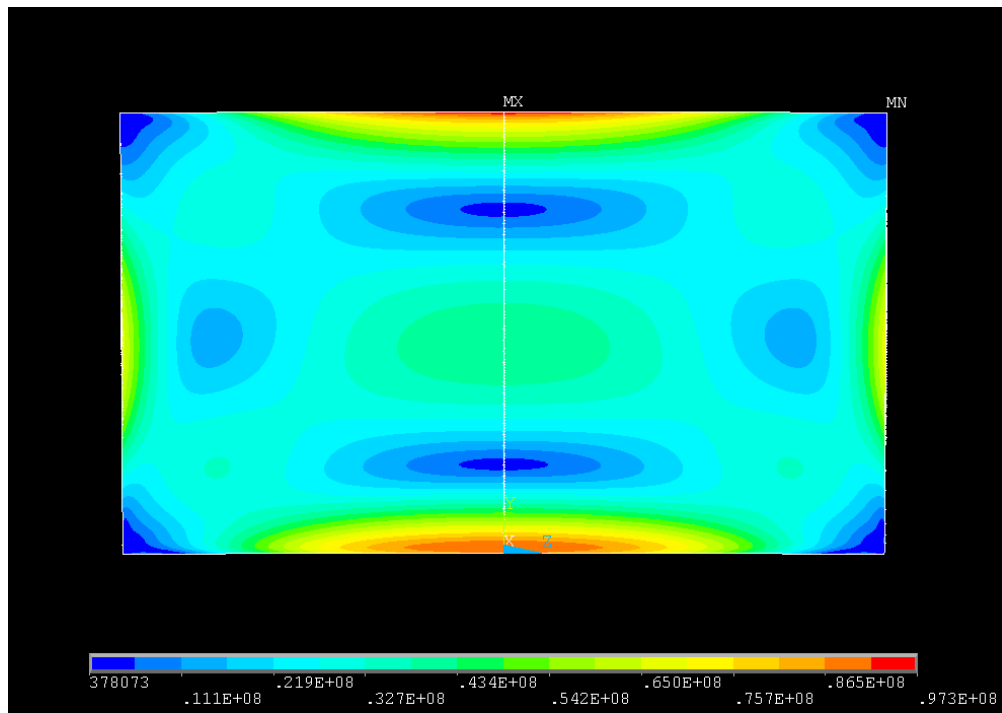


Fig. 38. Von Mises Equivalent Stress in Steady State LTHE, (Pa)

Low Temperature Heat Exchanger Transient Thermal Stress

The LTHE transient thermal stress analysis revealed that determining when the most harmful stresses occur during a thermal transient is nontrivial. Numerous temperature distribution snapshots for the 30.0 °K/s ramp rate case were tested in the LTHE Thermal Stress model to determine the most severe stress state. The results of these approximately 20 test runs are summarized in Fig. 39, which are plotted in sync with the heat transfer rate on the hot and cold fluid sides of the partition plate. It can be seen from this figure that the most severe stresses, which were compressive, occurred at about 21 seconds after the ramp procedure was commissioned as opposed to 7 seconds after the ramp was commissioned where the heat lag (ΔQ) was at a maximum. This result implies there is perhaps only a slight correlation between the timing of ΔQ and the most severe stress state during a transient period. During this most severe transient state, plastic strain was not endured but stress was found to be significantly worse than that calculated for the LTHE steady state, reaching -64.5 MPa in the Y dimension and -113 MPa in the Z dimension as shown in Fig. 39 (c).

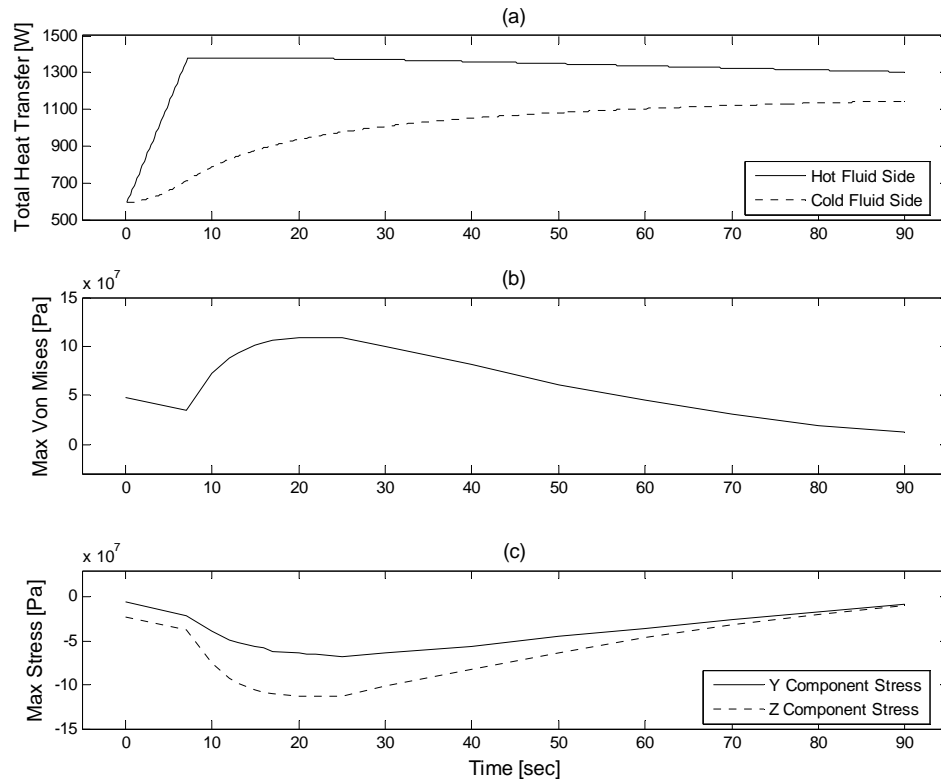


Fig. 39. Maximum transient thermal stress occurrences for the 30.0 °K/s ramp rate case: (a) Heat transfer to and from a single heat exchanger plate, (b) Von Mises Equivalent stress, and (c) Y and Z Component stresses

To help visualize how thermal stress can be created in heat exchanger partition plates during transient operation, an oblique view contour plot of temperature for the transient state LTHE is shown in Fig. 40, along with its corresponding thermal strain magnified by 100X. It can be observed from this figure that the length edges of the plate are relatively straight, as opposed to the LTHE steady state condition shown in Fig. 31, where the length edges have curvature. This implies that for the transient case, only the hot fluid inlet end of the plate has yet had a chance to expand due to increased temperature. Thus, it would be expected that in this case, compressive stress exists along the width edge of

the hot inlet end of the plate, which must be accompanied by a reactionary, or tensile stress in or near the center region of the plate.

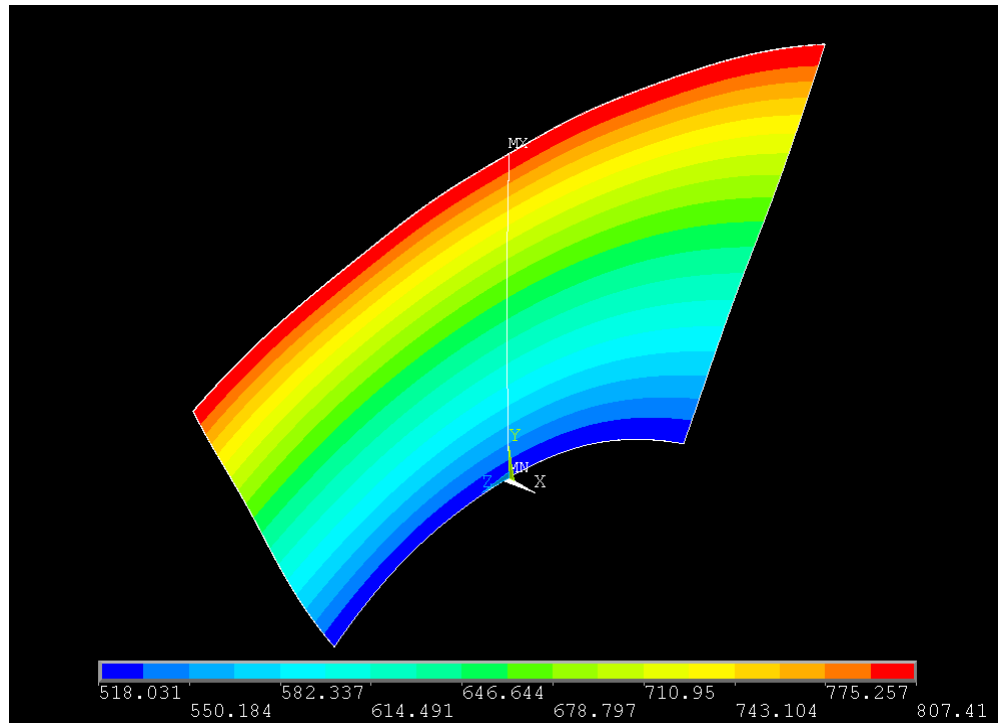


Fig. 40. Body Temperature and Magnified Strain in Transient State LTHE, ($^{\circ}\text{K}$)

Fig. 41 and Fig. 42 are contour plots of Y and Z Component thermal stress for the LTHE transient state condition. As expected from the observation of Fig. 40, it is shown in Fig. 42 that compressive stress (indicated by the negative values as shown in the legend) indeed exists at the hot inlet edge of the plate, and that tension (indicated by the positive values as shown in the legend) exists near the center region of the plate during the temperature ramp up procedure. It is shown in this figure that the most severe stresses during this thermal transient were located at the hot fluid inlet end of the plate, which was implied by the concentration of temperature contours shown in Fig. 30 (e).

Fig. 43 is a contour plot of YZ Shear stresses for the LTHE transient state condition; note that the maximum shear stresses are located near the corners of the hot fluid inlet end of the plate, and that the minimum shear stresses are located near the corners of the cold fluid inlet end of the plate. This is in direct contrast to the YZ Shear stress profile for the LTHE steady state condition shown in Fig. 37. A contour plot of Von Mises Equivalent stress is shown in Fig. 44 for the LTHE transient state condition.

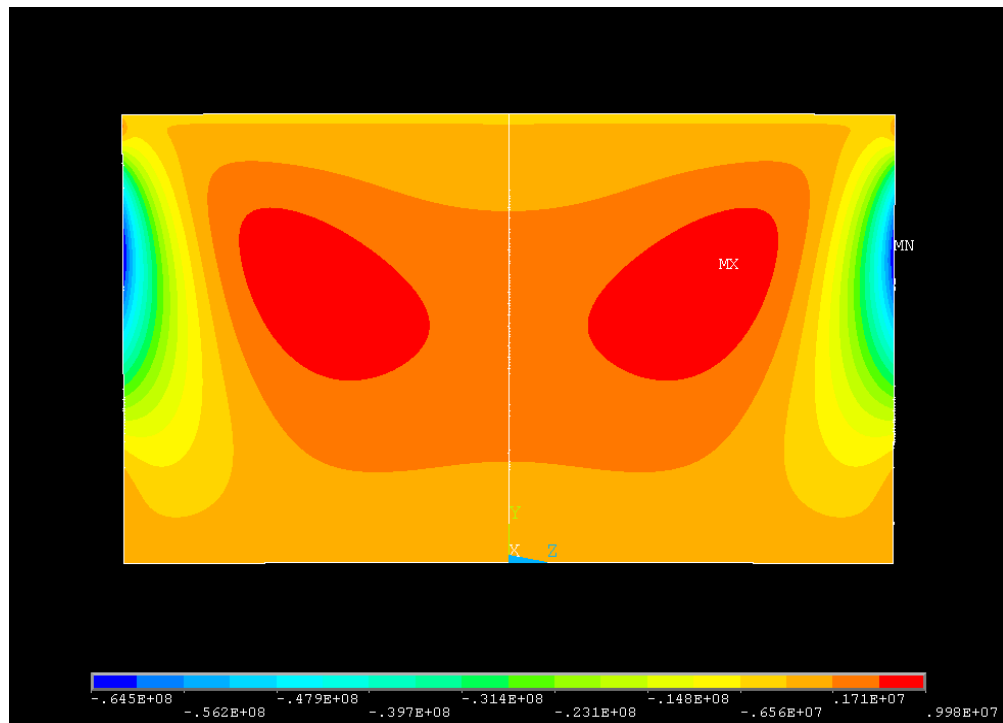


Fig. 41. Y Component Stress in Transient State LTHE, (Pa)

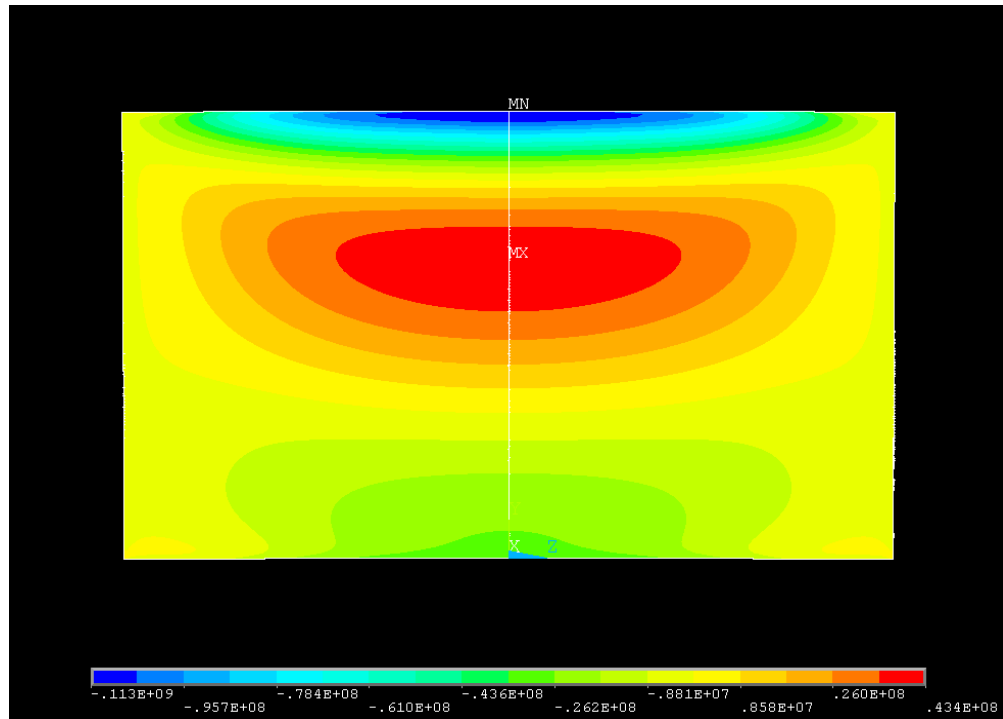


Fig. 42. Z Component Stress in Transient State LTHE, (Pa)

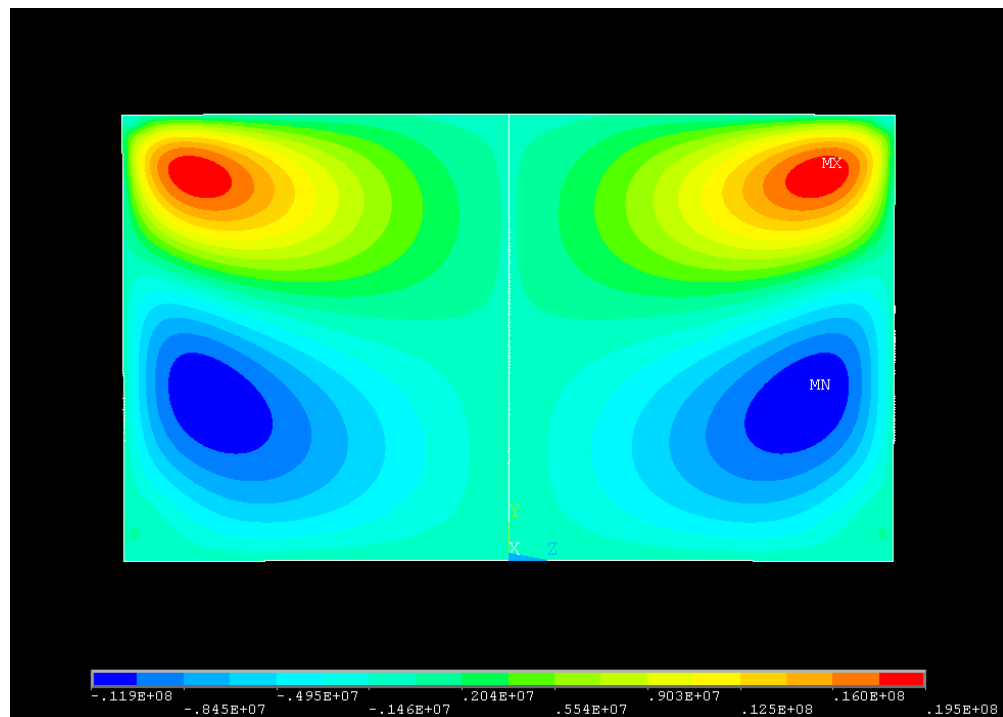


Fig. 43. YZ Shear Stress in Transient State LTHE, (Pa)

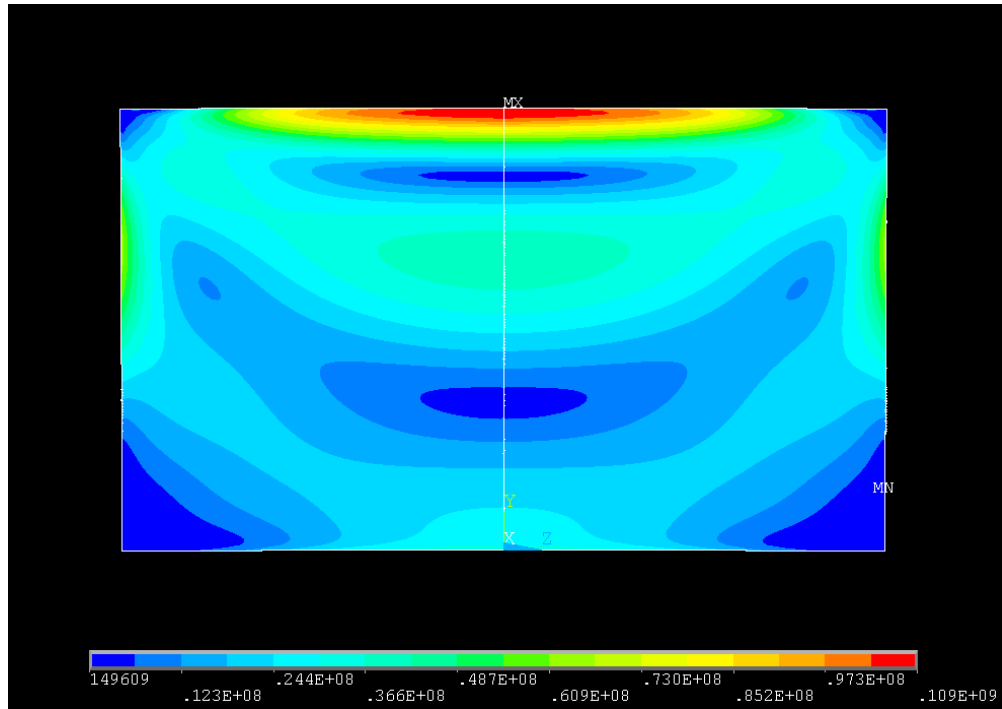


Fig. 44. Von Mises Equivalent Stress in Transient State LTHE, (Pa)

It was realized that the trend of the static (before ramp up and steady state) stress contour plots and transient stress contour plots were essentially opposite of one another. For the steady state condition, tension exists along the partition plate edges and compression exists in the center region of the plate. For the transient state condition, compression exists in salient portions of the partition plate edges and tension exists near the center region of the plate. Therefore, portions of the partition plate edges undergo a complete shift in stress from tension in the before ramp up state to compression in the transient state and then back to tension again during steady state operation when subject to the 30.0 °K/s ramp schedule. Further, it is noted that both steady and transient stress states have in common the location of the most severe stress, namely the center of the hot fluid inlet edge of the partition plate as shown in Fig. 38 and Fig. 44. It is here that a

concern of low cycle fatigue failure would be present. A summary of maximum and minimum stress values found in the LTHE partition plate for the before ramp up, most severe transient state, and after ramp up (steady state) are shown in Table 9.

Table 9. LTHE Maximum and Minimum Stress Summary

Stress (MPa)	Before Ramp		Transient State		Steady State	
	Maximum	Minimum	Maximum	Minimum	Maximum	Minimum
Y Component	33.765	-6.035	9.985	-64.478	69.214	-12.769
Z Component	46.722	-22.999	43.355	-113.130	95.660	-46.203
YZ Shear	9.312	-8.591	19.521	-11.945	19.110	-17.600
Von Mises	47.584	NA	109.450	NA	97.273	NA

High Temperature Heat Exchanger Thermal Stress Before Creep

Plate temperature and corresponding 100X magnified strain in the candidate HTHE designs before creep from the 300 hour operating cycle are shown in Fig. 45 and Fig. 46. It can be observed from these two figures how significant of a role the width dimension of the partition plate can play on producing thermal stress. Recall that the width of HTHECA is 25.4 cm and the width of HTHECB is 38.1 cm, which is the only difference between the two candidate HTHE partition plate designs. It can be seen in Fig. 45 and Fig. 46 that the temperature distributions of these two plates are virtually identical. Also recall that stress was calculated in these two candidate partition plates for a before creep state, and an after creep state where the stress in the plates relaxed over time due to creep deformation.

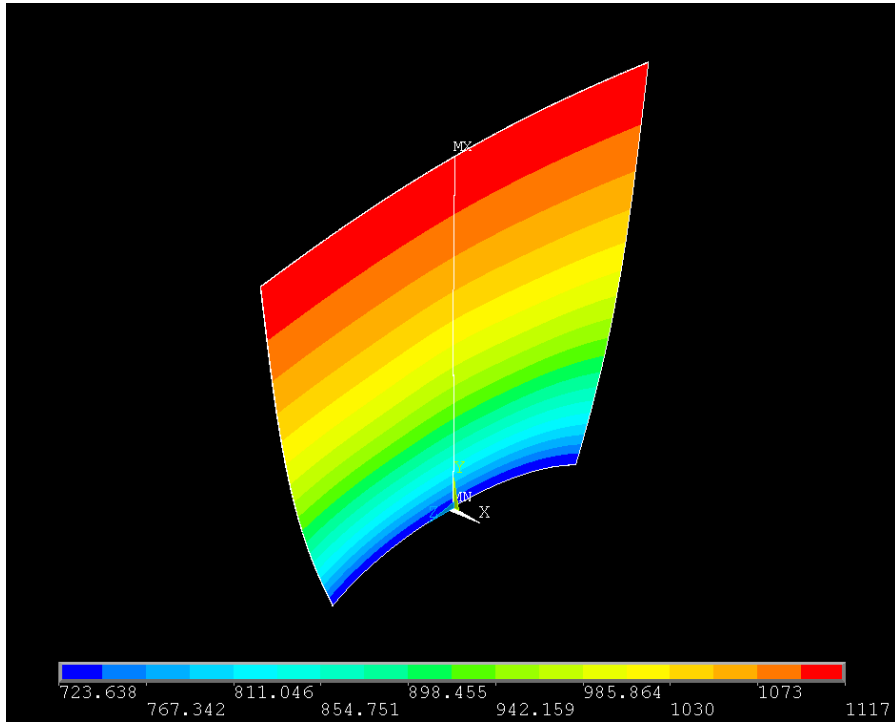


Fig. 45. Body Temperature and Magnified Strain in HTHECA Before Creep, (°K)

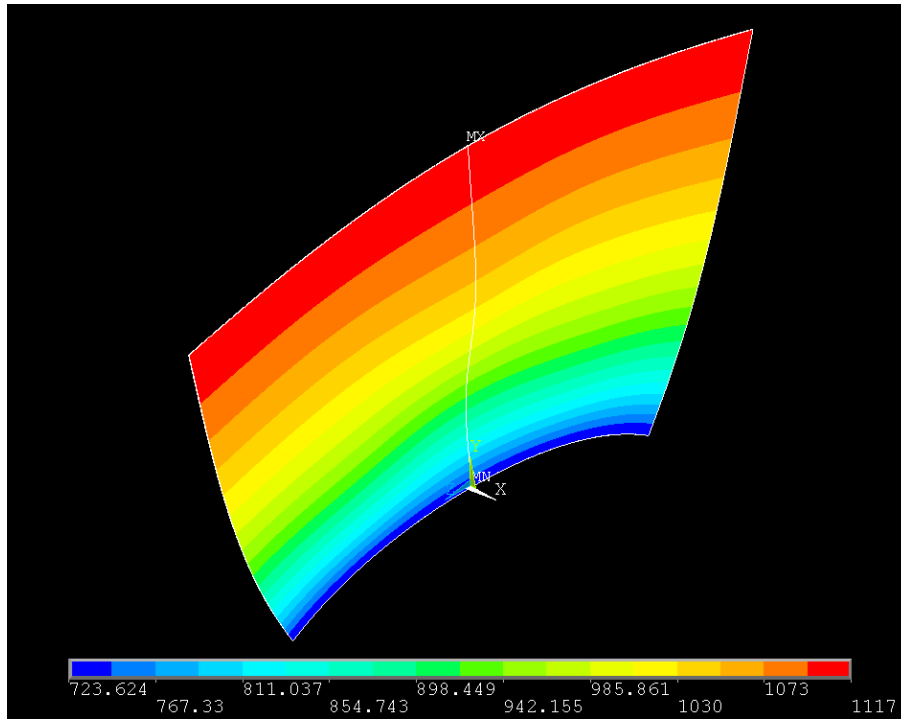


Fig. 46. Body Temperature and Magnified Strain in HTHECB Before Creep, (°K)

With the magnified oblique views of the HTHE partition plates shown in Fig. 45 and Fig. 46, it is clearly observed that the wider plate HTHECB endures much more distortion than HTHECA, which is certainly expected to be accompanied with more severe levels of stress. The reflective symmetry line at the center of these two plates is very telling. For HTHECA, it can be seen that its symmetry line is unaltered, straight as it was when the plate was at the uniform reference temperature. For HTHECB, one can clearly see that the symmetry line is wavy, indicating that the center of the plate was unable to expand as it would if it could expand freely. This wavy centerline is indicative of excessive compressive stress in the center region of the plate, with commensurate opposing (tensile) stress along the periphery of the plate. These hypotheses can be confirmed through observation of the stress contour plots of the two HTHE candidate designs shown in Fig. 47 through Fig. 54.

The stress contours for the two HTHE candidate designs HTHECA and HTHECB were observed to be very similar. Fig. 47 and Fig. 48 show the Y Component stresses of HTHECA and HTHECB respectively. It is shown in these two figures that, similar to the LTHE steady state condition, tension exists along the length edges and compression exists in the center region of the partition plates. In HTHECA, the most severe Y Component stress is 84.3 MPa and in HTHECB the most severe Y Component stress is 89.8 MPa. Fig. 49 and Fig. 50 show the Z Component stresses of HTHECA and HTHECB respectively. Also, similar to the LTHE steady state condition, it is shown in these figures that tension exists along the width edges and compression exists in the center region of the of the partition plates. In HTHECA, the most severe Z Component

stress is 95.9 MPa and in HTHECB the most severe Z Component stress is 132 MPa. The magnitude of Z Component stress produced in the partition plates was the most notable difference between the two candidate designs. As will be shown subsequently, these stresses are rather high for long term, high temperature operation. Although, neither candidate design endures stress high enough to induce plastic damage from operating at steady state.

Fig. 51 and Fig. 52 show the YZ Shear stresses for HTHECA and HTHECB respectively, where they too exhibit very similar stress contours to that of the LTHE steady state condition. These figures show that the most severe YZ Shear stress in HTHECA is 22.5 MPa and the most severe YZ Shear stress in HTHECB is 25.5 MPa. Like the LTHE steady state condition, the shear stresses are not very harmful in comparison to the component stresses. Contour plots of Von Mises Equivalent stress calculated for the two HTHE candidate designs are shown in Fig. 53 and Fig. 54. Similar to the steady state LTHE equivalent stress plot shown in Fig. 38, it can be seen that a region of zero stress, or a transition region, exists between the areas of tension and compression found in the candidate partition plates. This transition region appears in the shape of a circle for HTHECA and an oval for HTHECB. In contrast to the LTHE results, the HTHE results were found to have the most severe stress location at the center of the cold fluid inlet end of the partition plate as shown in Fig. 53 and Fig. 54. Table 10 contains a summary of salient maximum and minimum stresses found in the two HTHE design candidates before the creep process.

Table 10. HTHE Maximum and Minimum Stress Before Creep

Stress (MPa)	HTRCA		HTRCB	
	Maximum	Minimum	Maximum	Minimum
Y Component	84.258	-26.940	89.783	-16.691
Z Component	95.902	-34.572	132.340	-58.031
YZ Shear	22.524	-18.450	25.522	-21.814
Von Mises	91.802	NA	128.030	NA

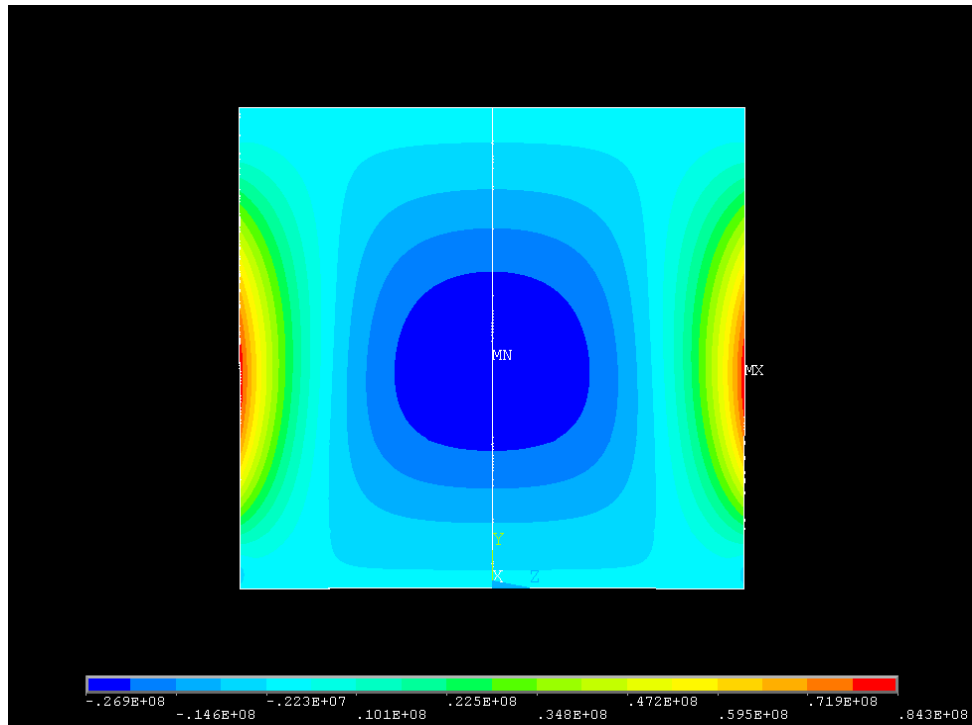


Fig. 47. Y Component Stress in HTHECA Before Creep, (Pa)

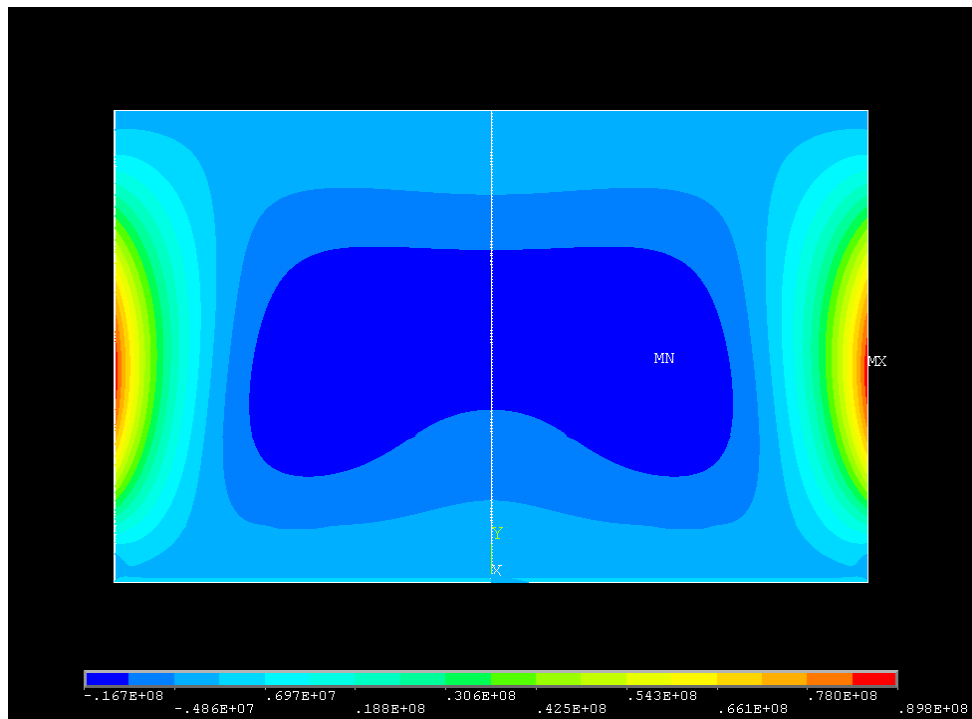


Fig. 48. Y Component Stress in HTHECB Before Creep, (Pa)

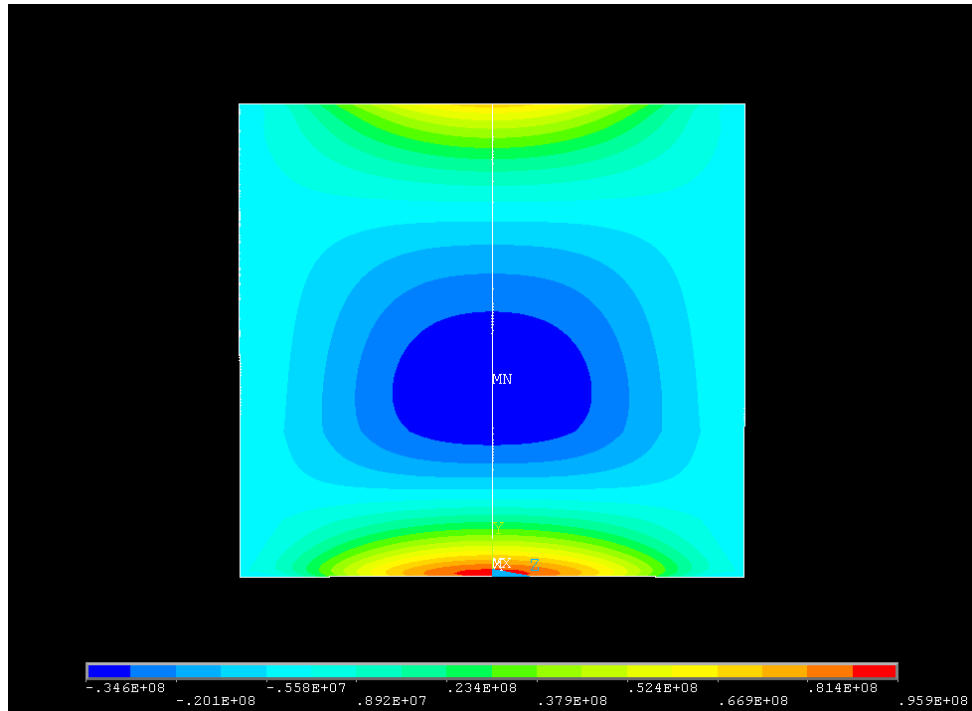


Fig. 49. Z Component Stress in HTHECA Before Creep, (Pa)

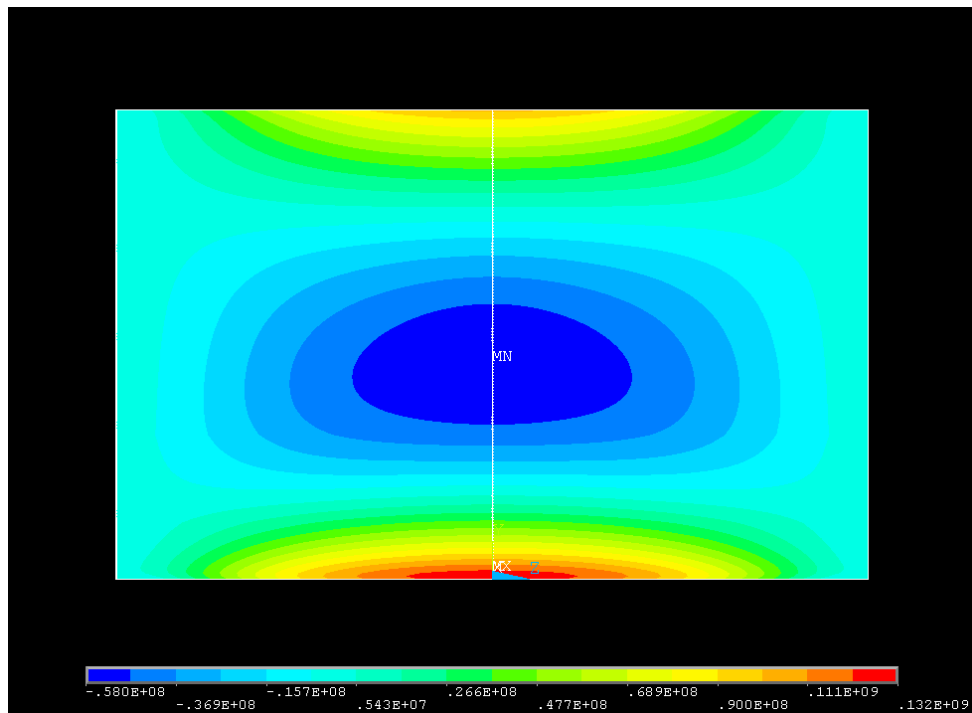


Fig. 50. Z Component Stress in HTHECB Before Creep, (Pa)

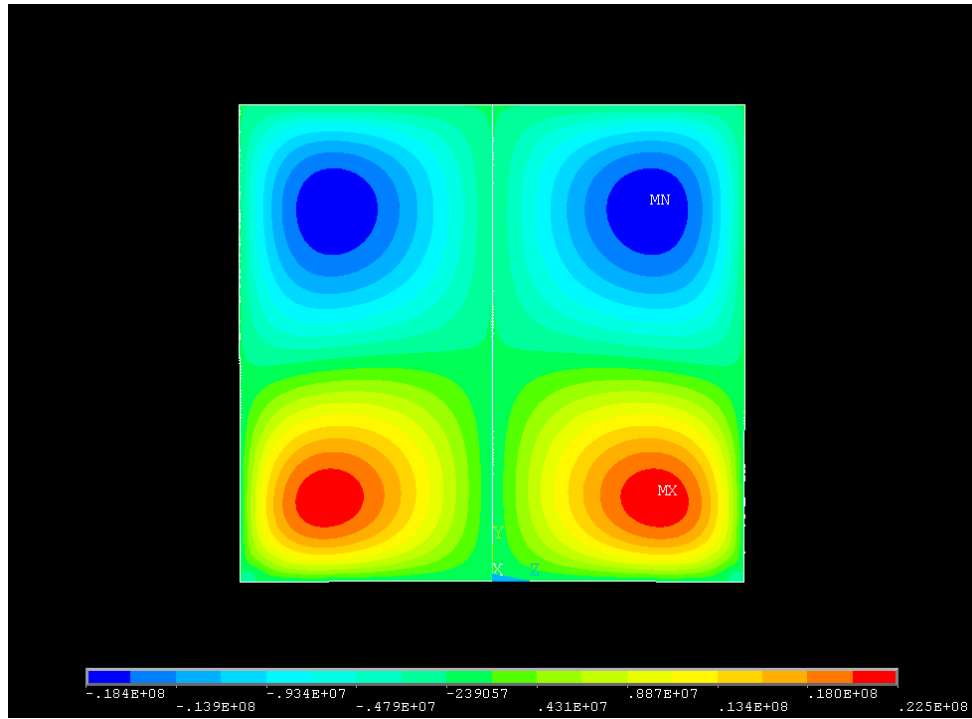


Fig. 51. YZ Shear Stress in HTHECA Before Creep, (Pa)

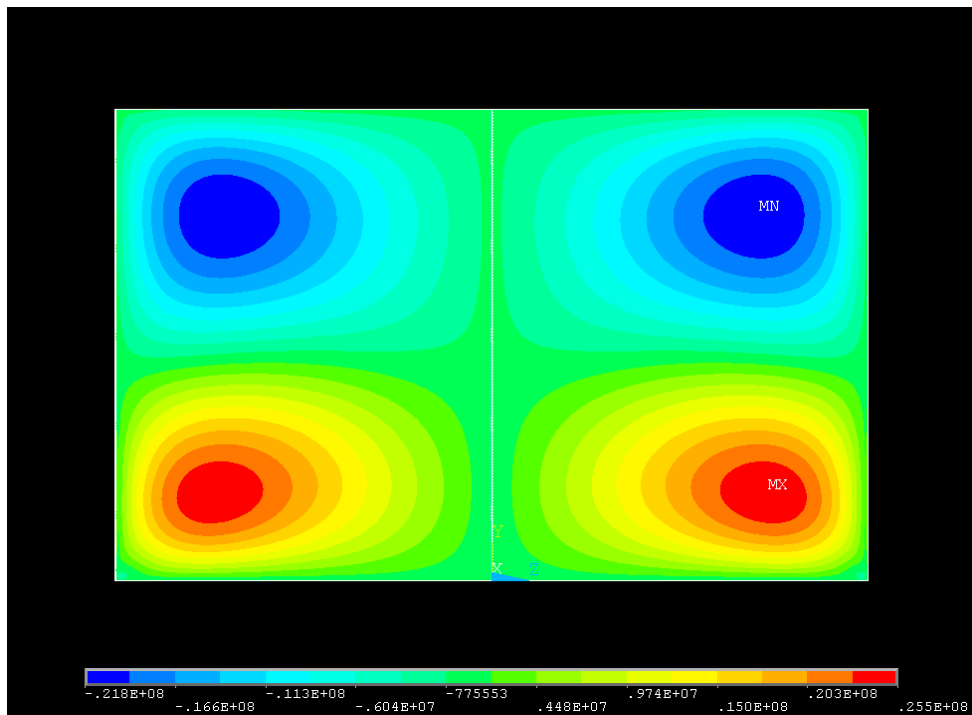


Fig. 52. YZ Shear Stress in HTHECB Before Creep, (Pa)

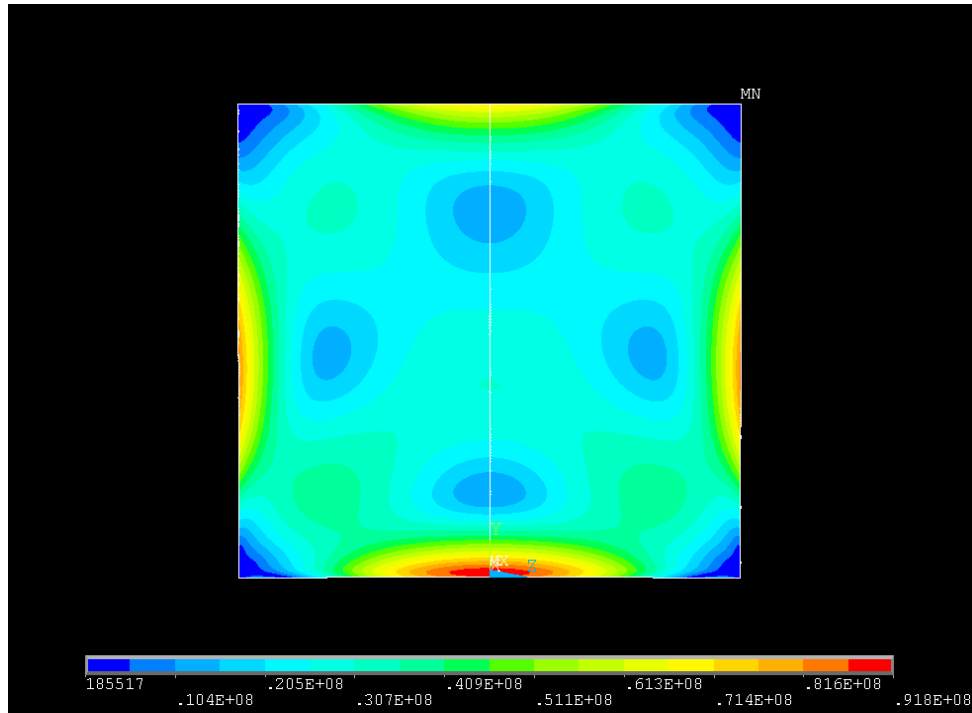


Fig. 53. Von Mises Equivalent Stress in HTHECA Before Creep, (Pa)

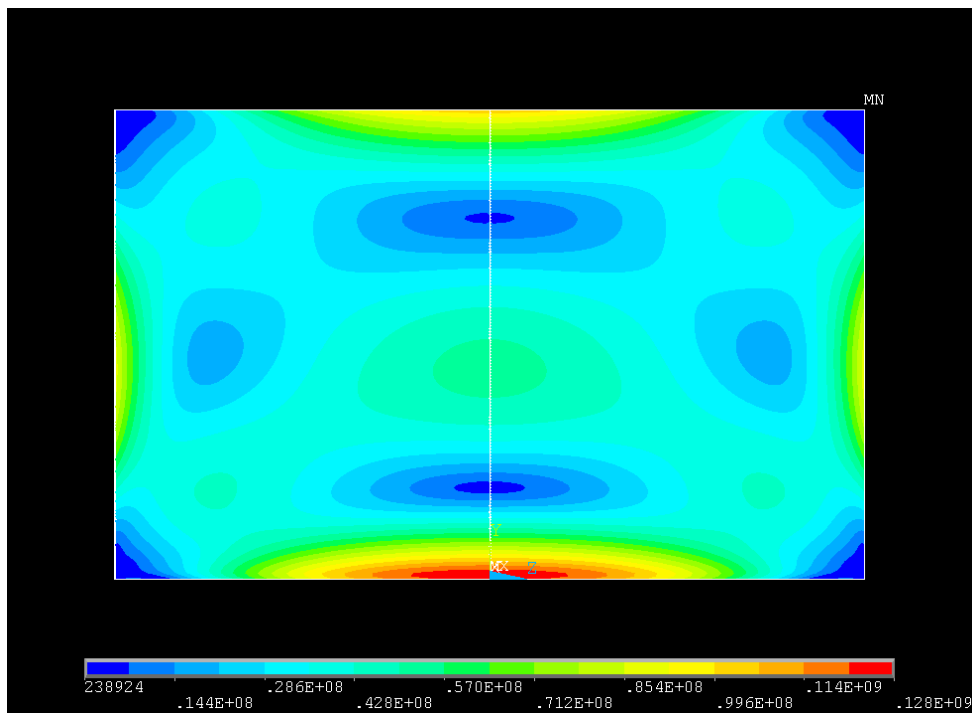


Fig. 54. Von Mises Equivalent Stress in HTHECB Before Creep, (Pa)

High Temperature Heat Exchanger Thermal Stress After Creep

Plate temperature and corresponding 100X magnified strain for the two candidate HTHE designs after the creep process are shown in Fig. 55 and Fig. 56. The plate temperature distributions are the same as they were before the creep process, though due to the creep process, the magnified strain shown for the two figures has changed. It can be observed from Fig. 56 that the symmetry line in the center of the HTHECB partition plate is no longer wavy, as was the case before the creep process as shown in Fig. 46. This implies that a significant amount of stress was relieved due to creep somewhere in this partition plate. Fig. 57 through Fig. 64 show contour plots of Y Component stress, Z Component stress, YZ Shear stress, and Von Mises Equivalent stress after creep for the two HTHE candidate designs.

As observed in the before creep stress contour plots, the after creep stress contour plots for the two HTHE candidate designs HTHECA and HTHECB were observed to be very similar. Fig. 57 and Fig. 58 show the Y Component stresses of HTHECA and HTHECB respectively. It is shown in these two figures that tension remains along the length edges of the partition plates, and compression remains in the center region of the of the partition plates. Though, a significant amount of stress was relaxed, especially near the hot fluid inlet end of the partition plates (which is located at the top of the contour plots). In the HTHECA candidate design, the most severe Y Component stress after creep is 52.7 MPa and in HTHECB the most severe Y Component stress is 53.0 MPa. Fig. 59 and Fig. 60 show the Z Component stresses of HTHECA and HTHECB respectively for the after creep stress state.

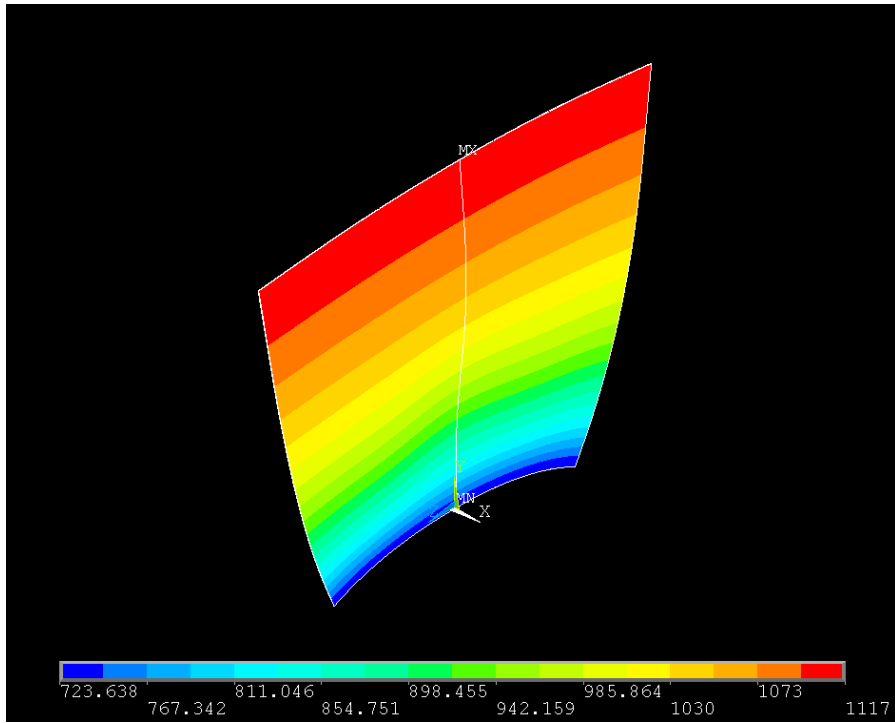


Fig. 55. Body Temperature and Magnified Strain in HTHECA After Creep, ($^{\circ}\text{K}$)

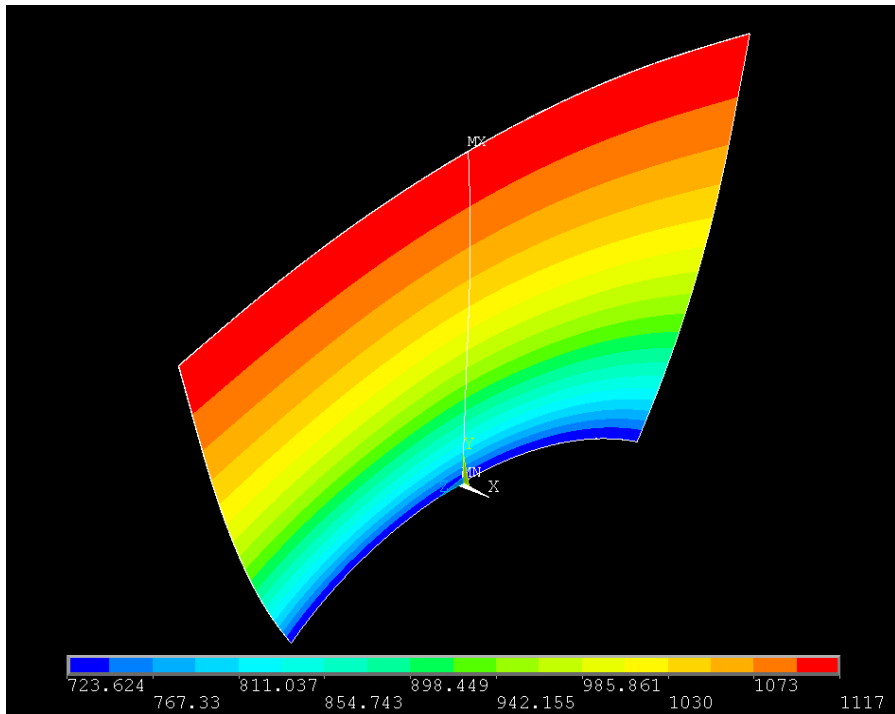


Fig. 56. Body Temperature and Magnified Strain in HTHECB After Creep, ($^{\circ}\text{K}$)

It is shown in these figures that tension remains only along the width edge at the cold fluid inlet end of the partition plates (which is located at the bottom of the contour plots). Fig. 59 and Fig. 60 also show that compression in the Z direction still exists in the center region of the partition plates, though it too is located closer to the cold fluid inlet end of the partition plates due to the stress relaxation that occurred in the hot fluid inlet region of the partition plates. In HTHECA, the most severe Z Component stress after creep is 66.8 MPa and in HTHECB the most severe Z Component stress is 78.8 MPa.

Fig. 61 and Fig. 62 show the YZ Shear stresses for HTHECA and HTHECB respectively for the after creep state. These figures show that stress relaxed in the hot fluid inlet region of the partition plates, and that the most severe YZ Shear stress remaining in HTHECA is 14.6 MPa and the most severe YZ Shear stress remaining in HTHECB is 14.9 MPa. Contour plots of Von Mises Equivalent stress after creep for the two HTHE candidate designs are shown in Fig. 63 and Fig. 64. It can be seen in these figures that stress was relaxed in the hot fluid inlet region of the candidate partition plates. The amount of stress that remains in the hot fluid inlet region of the candidate plates after the creep process is approximately zero. Table 11 is a summary of maximum and minimum stresses found in the two candidate plates after the creep process.

Table 11. HTHE Maximum and Minimum Stress After Creep

Stress (MPa)	HTRCA		HTRCB	
	Maximum	Minimum	Maximum	Minimum
Y Component	52.663	-11.442	53.008	-8.991
Z Component	66.769	-32.173	78.779	-40.574
YZ Shear	14.639	-9.950	14.918	-10.302
Von Mises	64.939	NA	76.954	NA

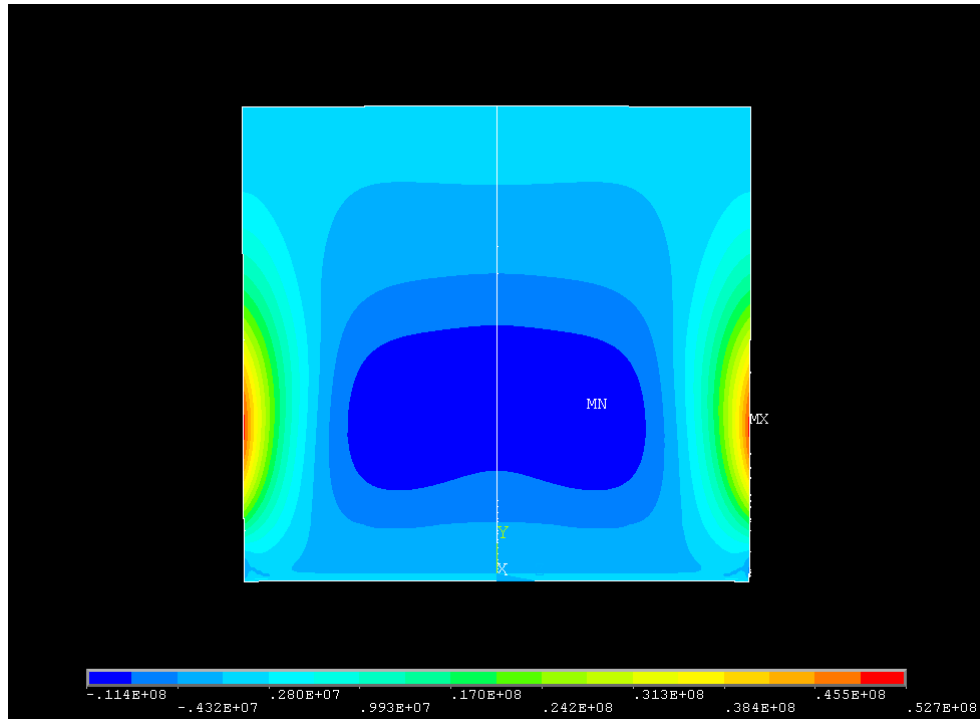


Fig. 57. Y Component Stress in HTHECA After Creep, (Pa)

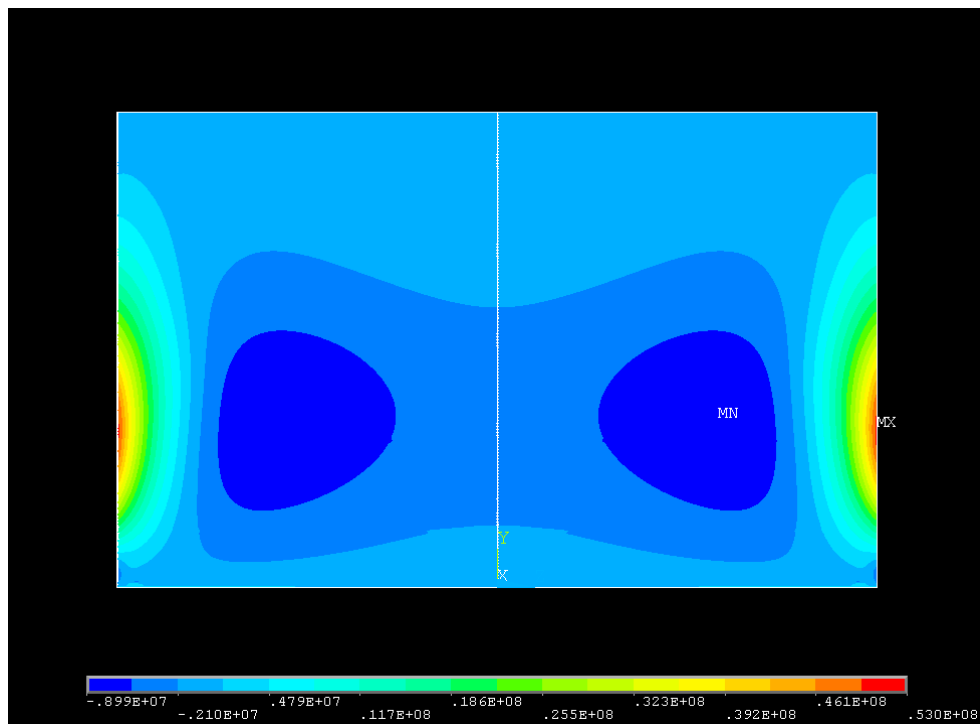


Fig. 58. Y Component Stress in HTHECB After Creep, (Pa)

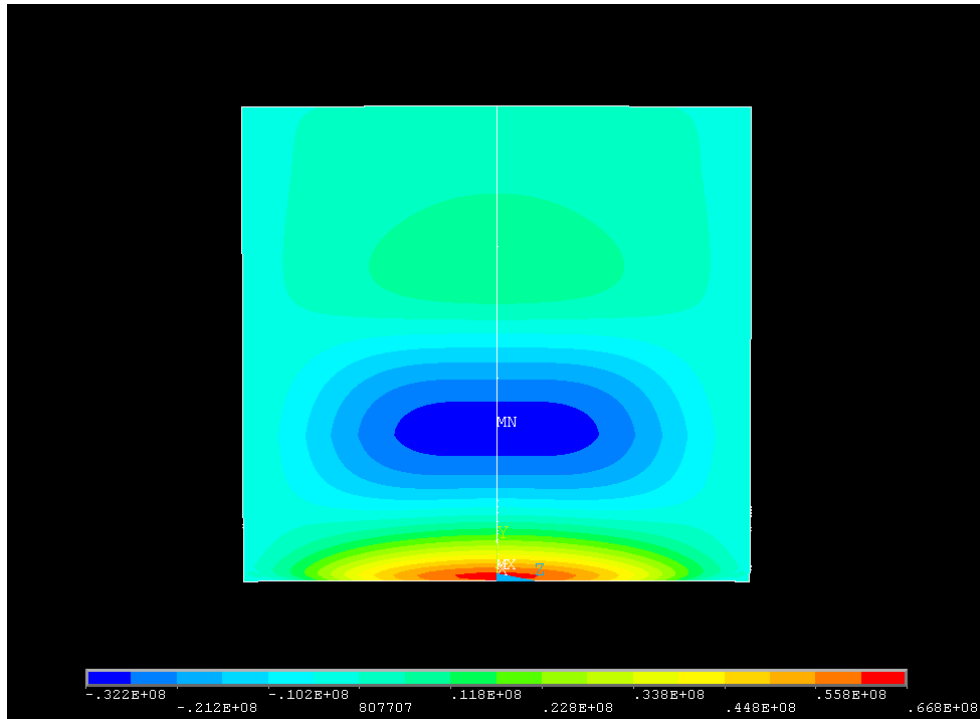


Fig. 59. Z Component Stress in HTHECA After Creep, (Pa)

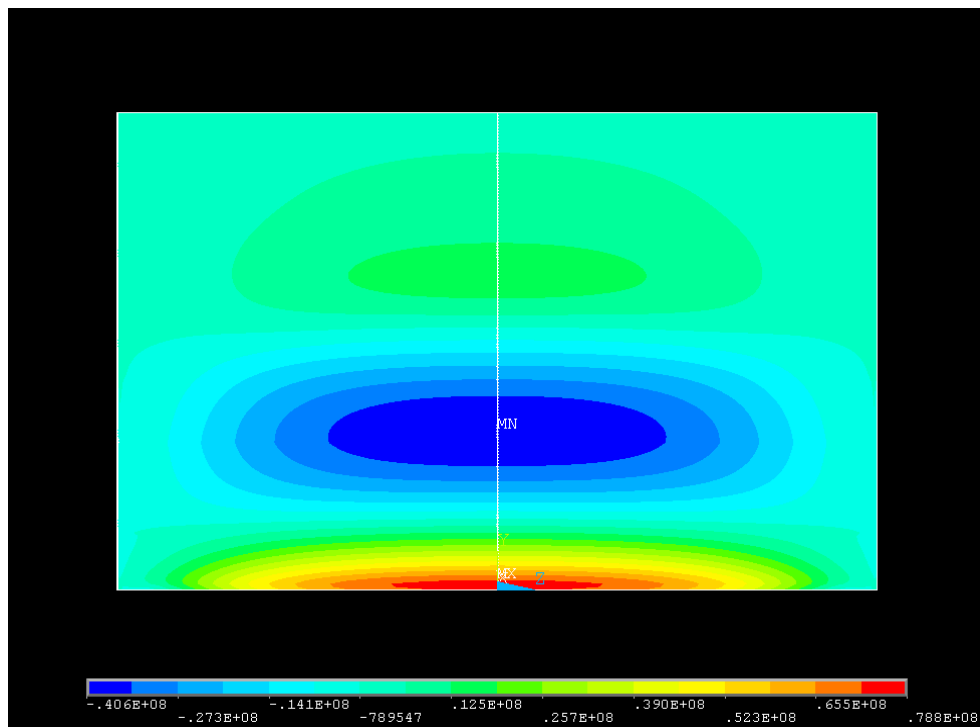


Fig. 60. Z Component Stress in HTHECB After Creep, (Pa)

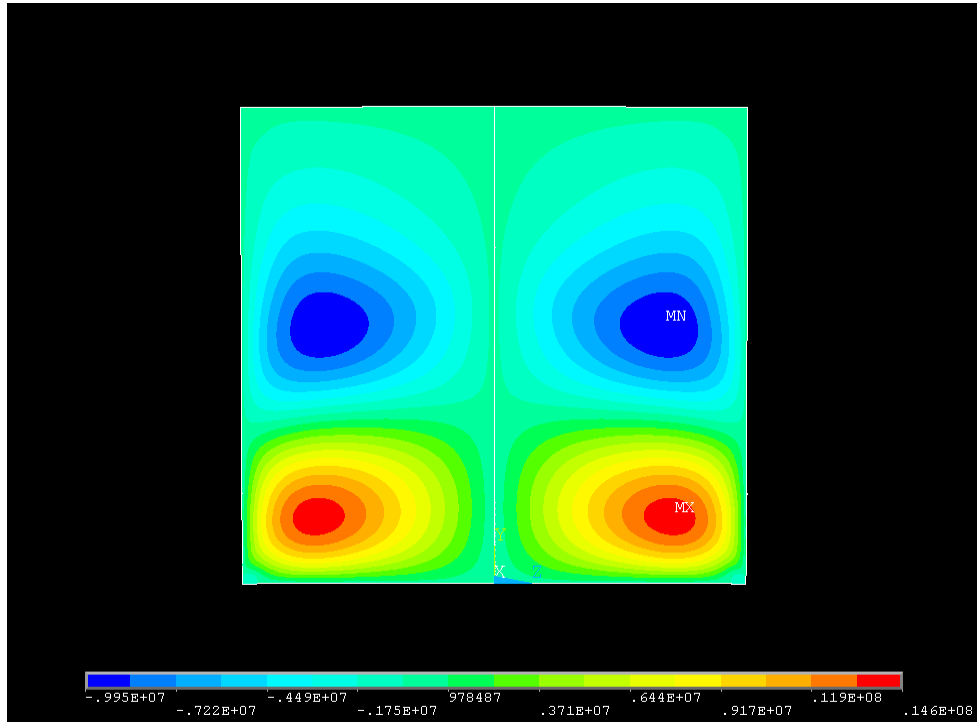


Fig. 61. YZ Shear Stress in HTHECA After Creep, (Pa)

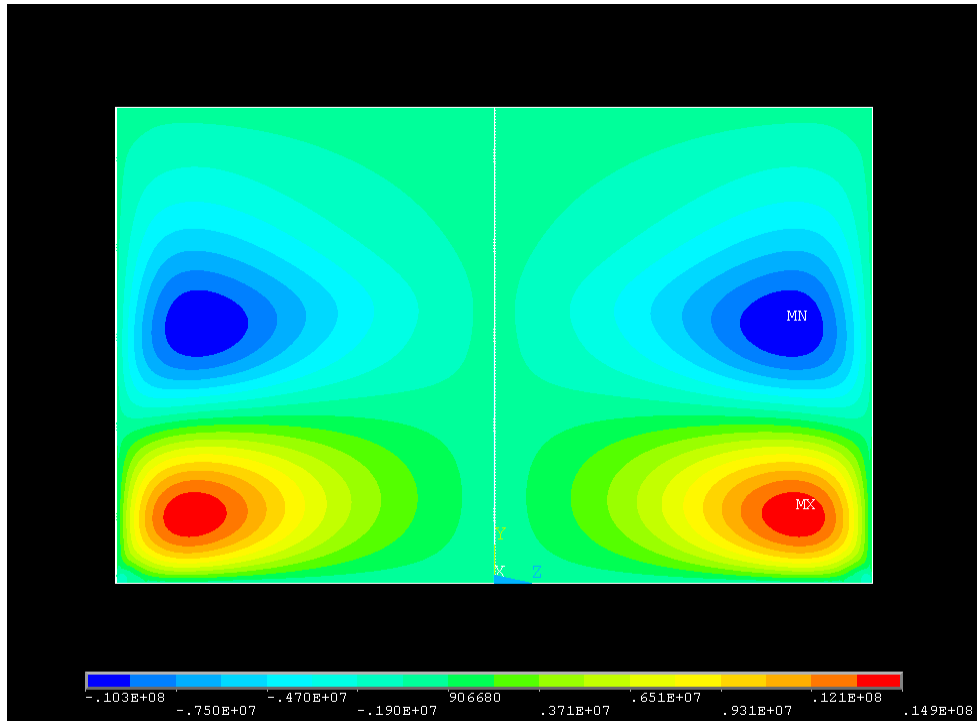


Fig. 62. YZ Shear Stress in HTHECB After Creep, (Pa)

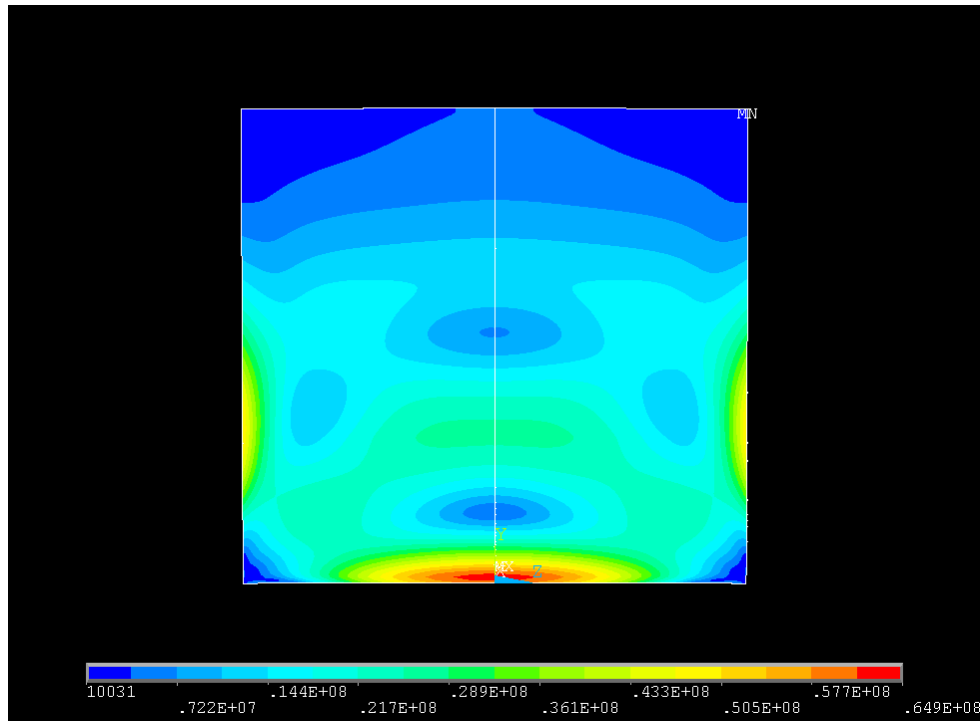


Fig. 63. Von Mises Equivalent Stress in HTHECA After Creep, (Pa)

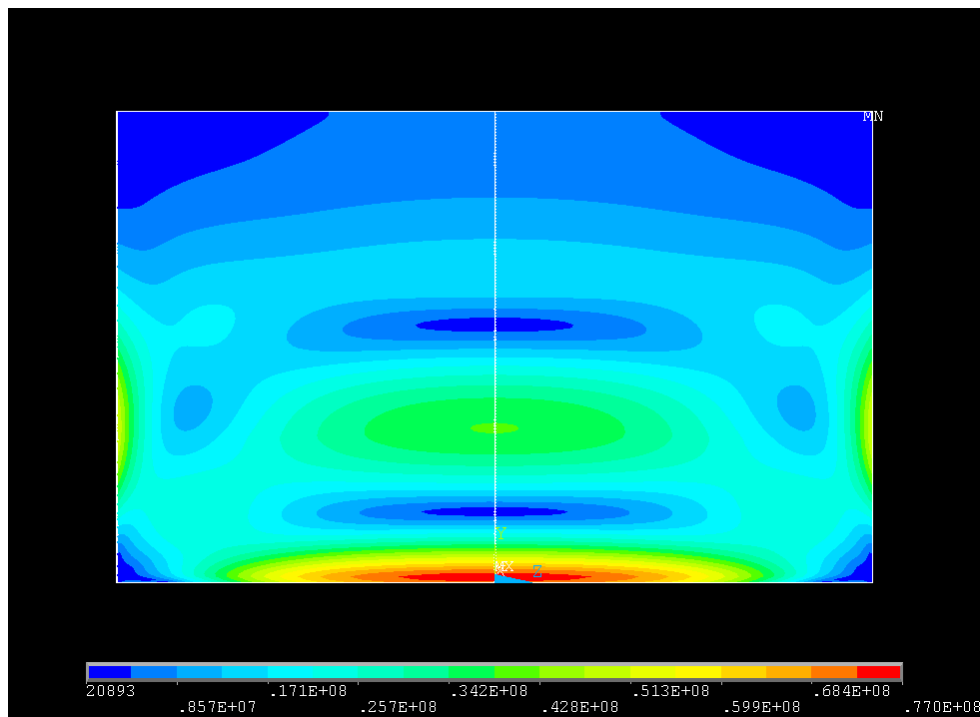


Fig. 64. Von Mises Equivalent Stress in HTHECB After Creep, (Pa)

Although the stress contour plots shown in Fig. 57 through Fig. 64 do not specify where the creep had occurred, it is certainly evident that it did occur given the amount of stress that was relaxed. For example, it can be seen in the Z Component stress contour plots shown in Fig. 59 and Fig. 60 that the maximum stress occurs in the same location as it did prior to the creep process as shown in Fig. 49 and Fig. 50, namely at the cold fluid inlet end of the partition plate. For HTHECA, this maximum stress relaxed from 95.9 MPa to 66.77 MPa, and for HTHECB, this maximum stress relaxed from 132.3 MPa to 78.78 MPa. Similar results can be seen for the other components of stress, though in some cases the maximum stress moved to a different location due to the creep process.

It was also observed that the Y and Z Component stress diminished virtually to zero in the hot fluid inlet region of the partition plates as shown in Fig. 57 through Fig. 60. This implies that this is the region where the majority or all of the creep had occurred. This is logical given that the hot fluid inlet edges were operating at 71.5 % of their melting point, which is approximately 1560 °K for solution-treated Inconel 625. It is also important to mention that since the heat exchanger partition plates crept virtually to zero stress in the hot fluid inlet region as shown in Fig. 57 through Fig. 60, no more creep would occur in this region during this cycle of heat exchanger operation. That is, all of the creep damage that could occur in this region of the partition plate has already taken place. This conclusion clearly substantiates the importance of designing for low thermal stress.

High Temperature Heat Exchanger Creep Comparison

Fig. 65 through Fig. 74 show contour plots of X Component creep strain, Y Component creep strain, the Z Component creep strain, YZ Shear creep strain, and Von Mises Equivalent creep strain for the two HTHE candidate designs. It can be seen from any of these creep strain figures that significant levels of creep occurred at the hot fluid inlet region of the heat exchanger plate, which is located at the top of the contour plots. At the most severe location, namely the center of the hot fluid inlet end of the plate, the HTHECA partition plate suffered 0.095 % and the HTHECB partition plate suffered 0.139 % creep strain in the Z Component direction as shown in Fig. 69 and Fig. 70 respectively. This severe location underwent a Z Component stress relaxation corresponding to 68.1 MPa for the HTHECA partition plate and 98.9 MPa for the HTHECB partition plate. The HTHECB partition plate suffered 46.6 % more creep damage than the HTHECA partition plate at this severe location in a single cycle of operation. In short, HTHECB would accelerate towards low cycle fatigue failure in comparison to HTHECA. This result is attributed solely to the discrepancy in plate aspect ratio (Width/Length), given that all other partition plate parameters were identical.

It was also observed from Fig. 65 through Fig. 74 that creep was not suffered at the cold fluid inlet end (the bottom) of the partition plate. Though, it was seen in previous contour plots, namely in Fig. 49, Fig. 50, Fig. 59, and Fig. 60, that stress relaxed significantly at the cold fluid inlet end of the partition plate. Hence, it must be concluded that stress at this location relaxed not by creeping itself, but through the creep that occurred elsewhere in the partition plate, namely at the hot fluid inlet region (the top).

It can also be seen that the tensile stresses in the Y and Z dimensions, in addition to the temperature of certain locations of the partition plate material, governed the creep processes. For example, Y Component tensile stresses located along the length of the partition plates and near the hot fluid inlet region of the plate as shown in Fig. 47 and Fig. 48, produced a positive creep strain in the Y direction as shown in Fig. 67 and Fig. 68. As a result, negative creep strain occurred in the X and Z directions at this location due to Poisson's ratio, which can be seen in Fig. 65, Fig. 66, Fig. 69, and Fig. 70. Thus, salient amounts of X Component creep strain did occur, even though there was very little X Component stress. This was the basis for maintaining a high grid resolution along the thickness of the plate. Lower grid resolutions were not tested to verify the assertion that this was necessary. Table 12 contains salient creep strain found in the two candidate heat exchanger partition plates.

Table 12. HTHE Maximum and Minimum Creep Strain

% Strain	HTRCA		HTRCB	
	Maximum	Minimum	Maximum	Minimum
X Component	0.0029	-0.0475	0.0033	-0.0695
Y Component	0.0330	-0.0472	0.0350	-0.0693
Z Component	0.0946	-0.0164	0.1388	-0.0175
YZ Shear	0.0003	-0.0553	0.0004	-0.0622
Von Mises	0.0946	NA	0.1388	NA

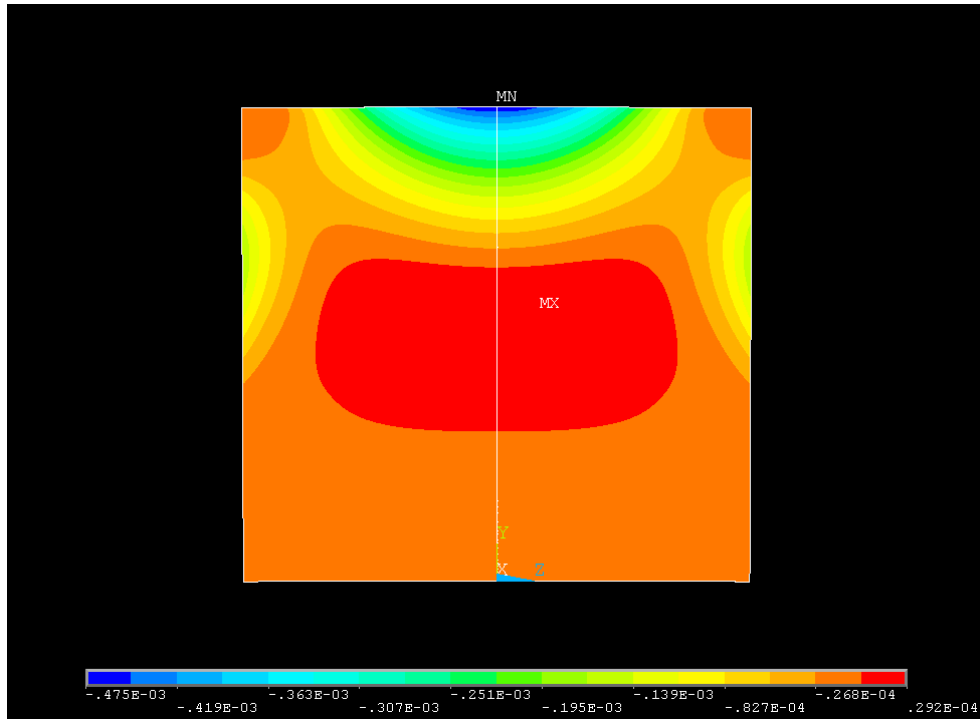


Fig. 65. X Component Creep Strain in HTHECA (---)

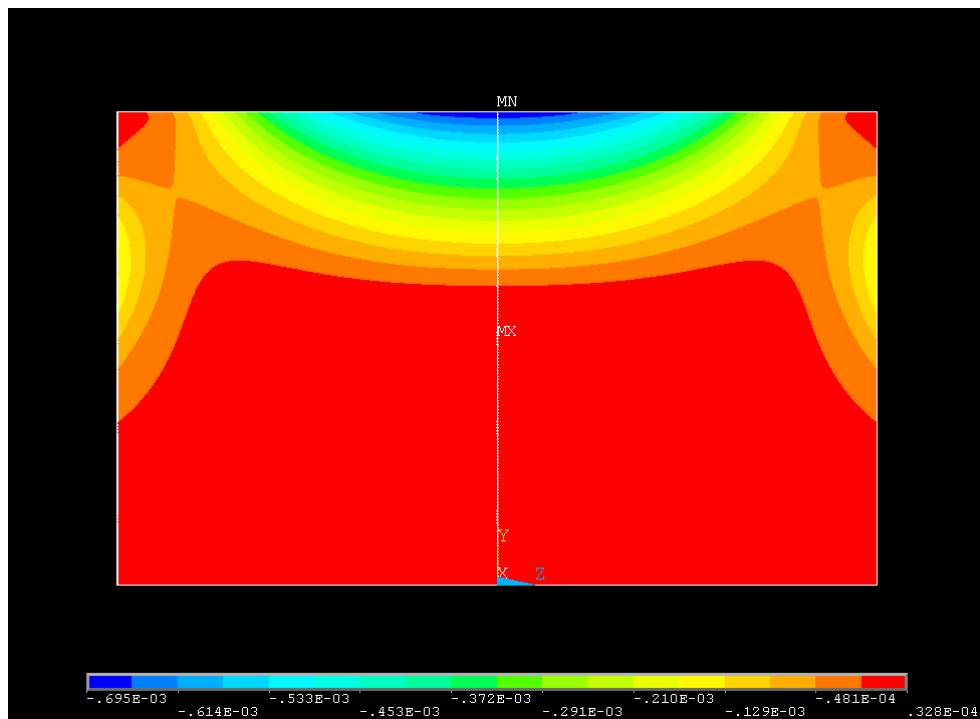


Fig. 66. X Component Creep Strain in HTHECB (---)

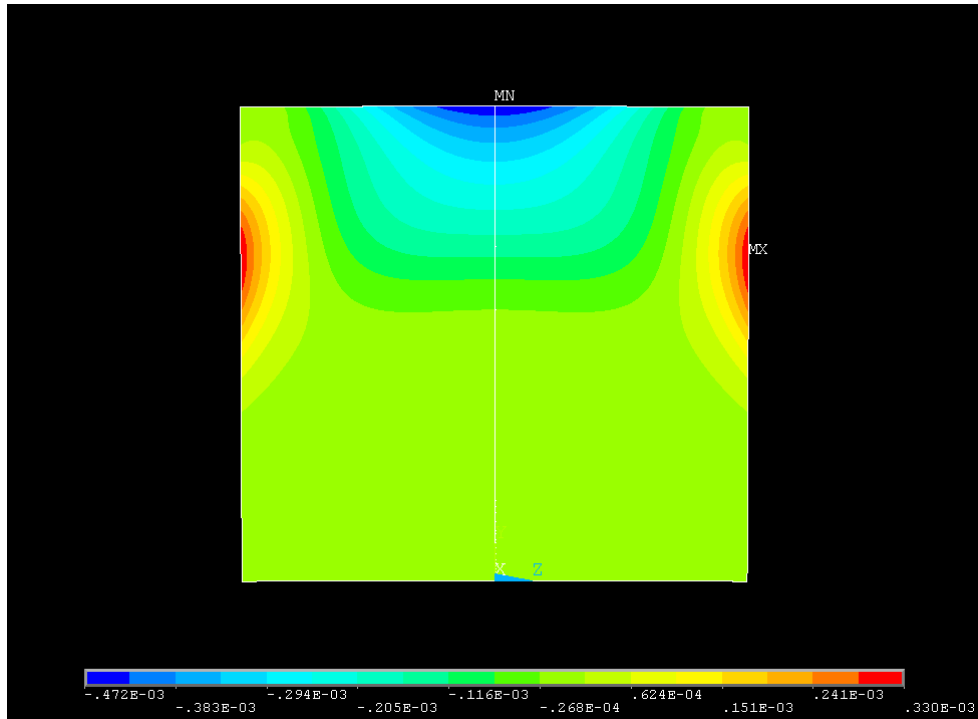


Fig. 67. Y Component Creep Strain in HTHECA (---)

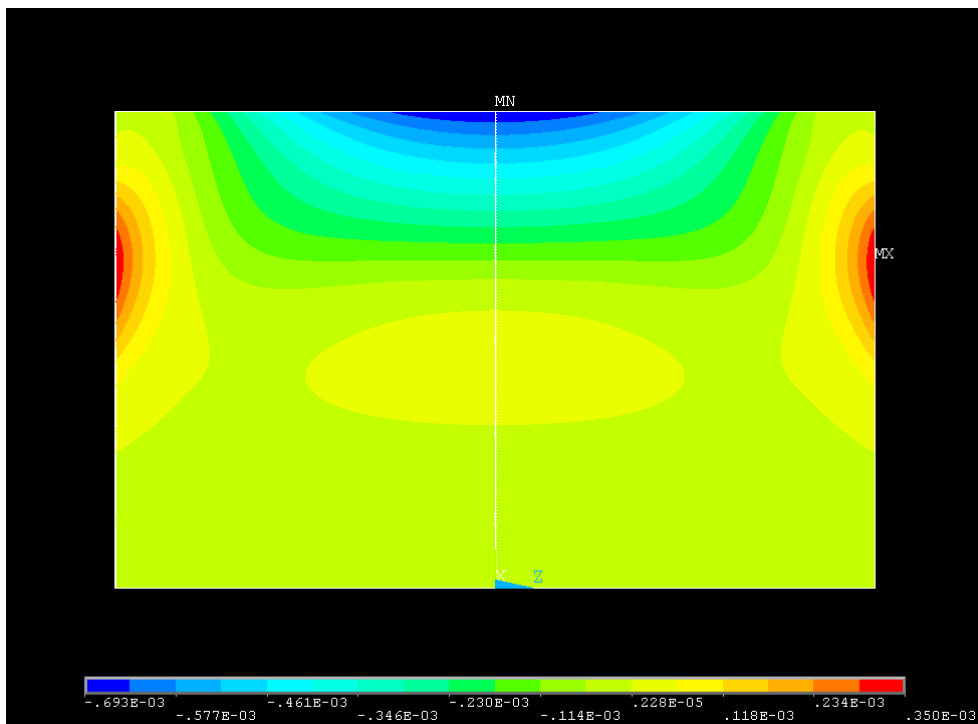


Fig. 68. Y Component Creep Strain in HTHECB (---)

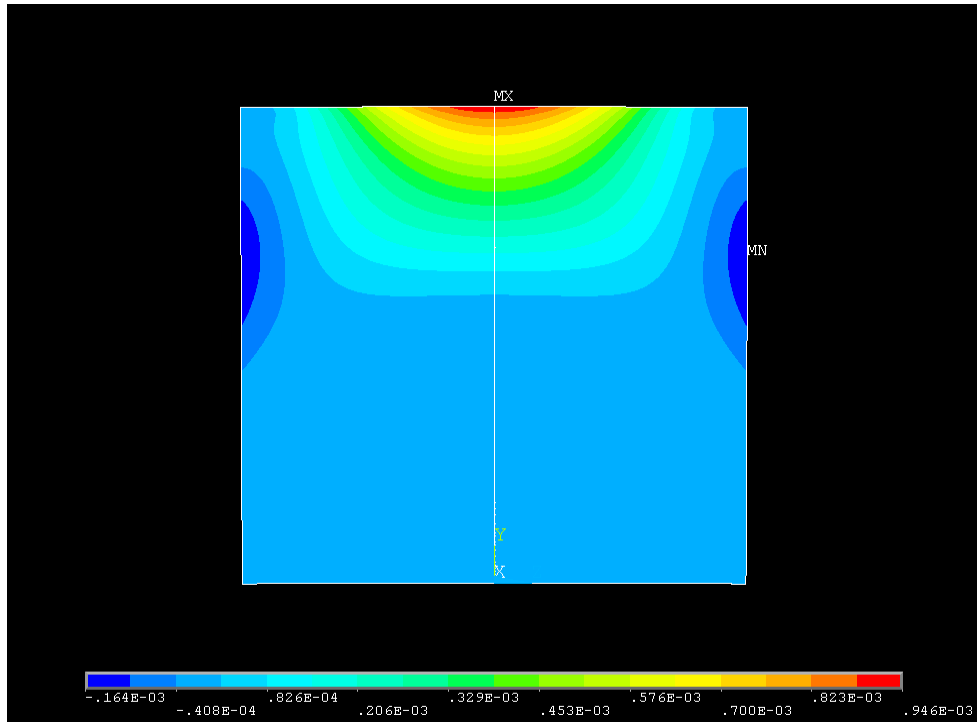


Fig. 69. Z Component Creep Strain in HTHECA (---)

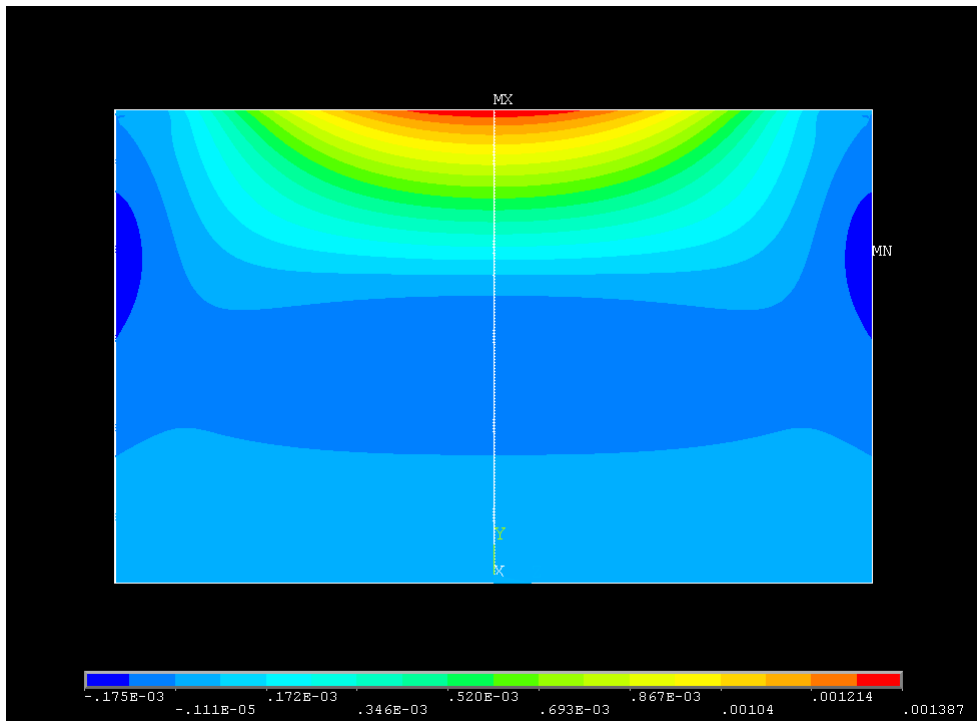


Fig. 70. Z Component Creep Strain in HTHECB (---)

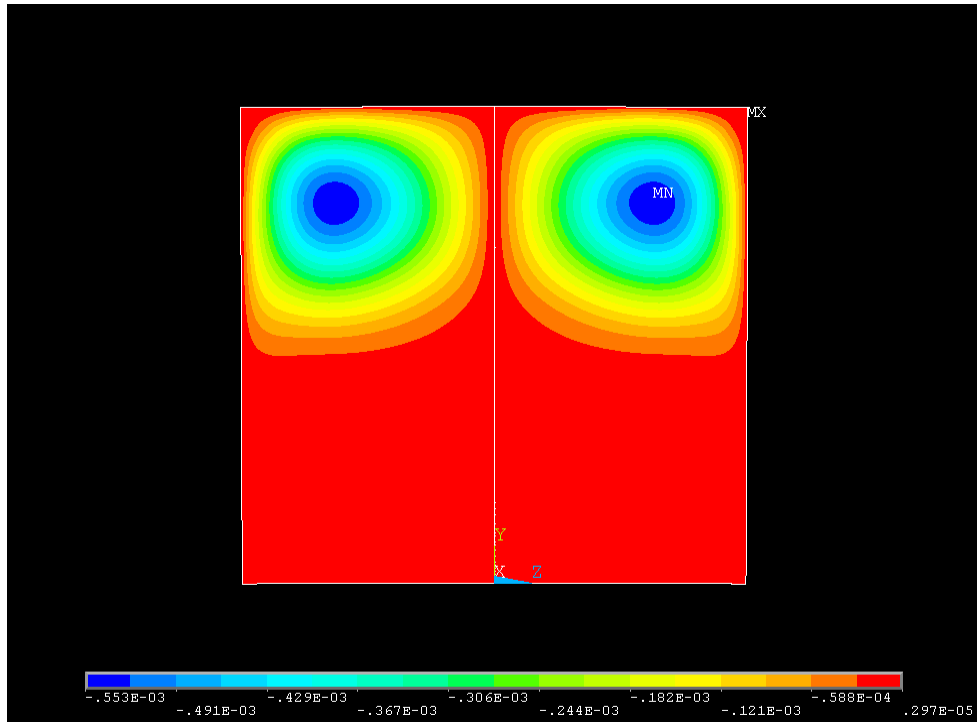


Fig. 71. YZ Shear Creep Strain in HTHECA (---)

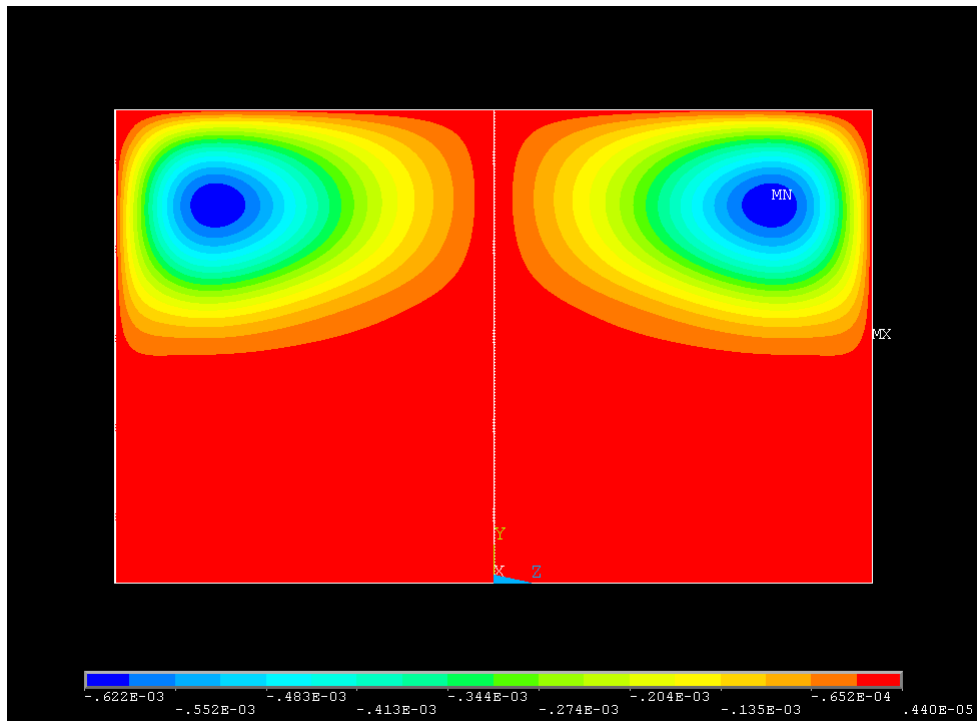


Fig. 72. YZ Shear Creep Strain in HTHECB (---)

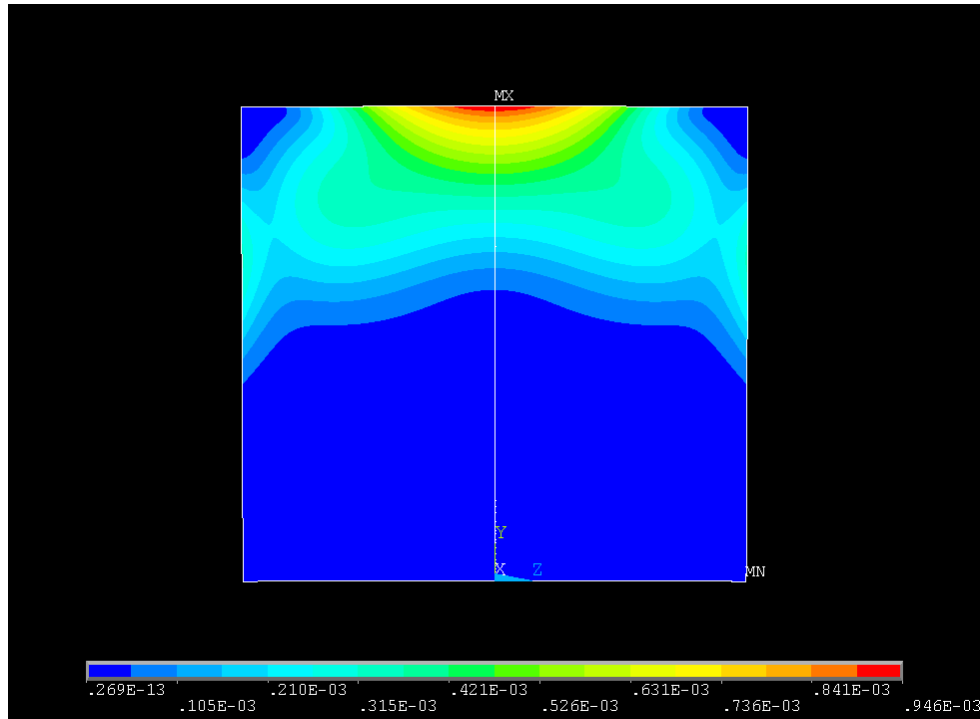


Fig. 73. Von Mises Equivalent Creep Strain in HTHECA (---)

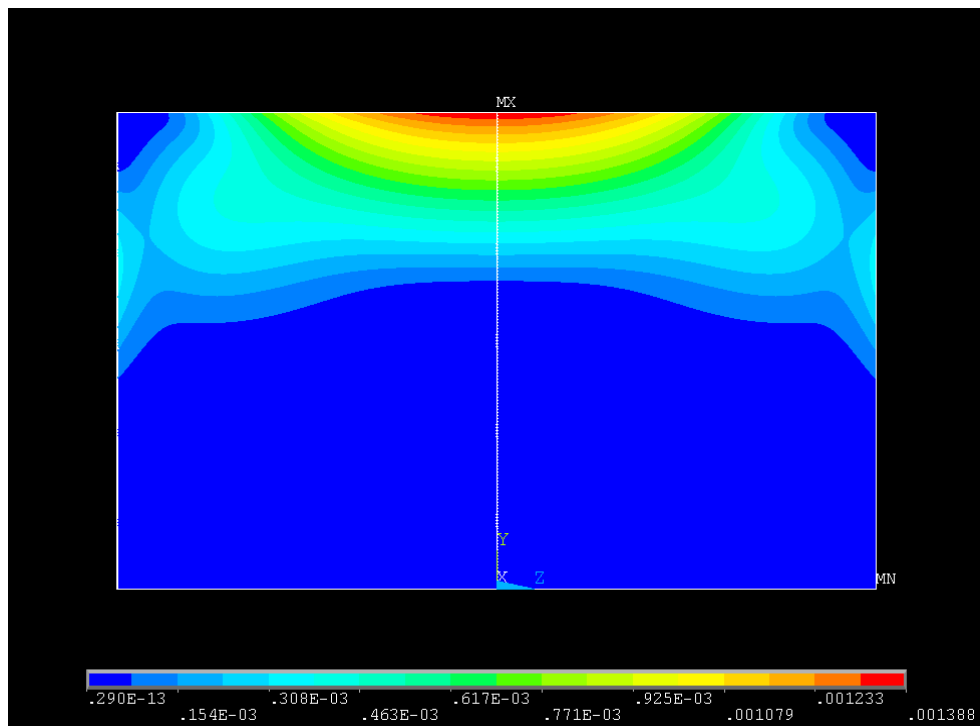


Fig. 74. Von Mises Equivalent Creep Strain in HTHECB (---)

CHAPTER 6

CONCLUSIONS AND RECOMMENDATIONS

Conclusions

Improvements in conventional heat exchanger design must be made to help bring theoretical hybrid fuel cell and gas turbine (FCGT) system designs to commercialization. Heat exchanger performance improvements can be made through the use of heat transfer surfaces that yield higher core thermal density and flow length given a specified pressure drop. Through the use of the latest heat exchanger construction materials and non-monolithic design techniques described by Child et al. (1999) and Abiko et al. (2003), increased operating temperature can be employed to further enhance heat exchanger functionality. Stainless steel 304 was found to provide a good combination of low cost, durability, and corrosion resistance for operating temperatures up to 925 °K. Solution-treated Inconel 625 was found to provide competitive corrosion and creep resistance for process gas temperatures up to 1150 °K. Managing heat exchanger cost will be a difficult task in the course of attaining these performance improvements, especially for the high temperature applications which will need to use special nickel alloys such as Inconel 625. These additional costs may be minimized by selecting heat transfer surfaces that yield longer flow lengths given a specified pressure drop, thus reducing the number of heat exchanger cells required for a given heat duty. Based on the heat exchanger literature review and fin performance comparison performed in this work, the plate-fin heat

exchanger with the louver fin geometry was determined as the most promising vehicle to obtain these improvements for the hybrid FCGT application.

The strip fin was found to be capable of producing a compact heat exchanger, though at the expense of a short flow length given a set pressure drop. The wavy fin was found to yield a longer flow length in comparison, but it was shown to yield lower thermal density given the same pressure drop and compactness level. The louver fin was found to yield high thermal density and long flow length relative to the competing surface geometries given the same pressure drop and compactness level. It was also revealed that the louver fin can be produced with a relatively inexpensive manufacturing process.

Durability has been a recurring issue for conventional gas turbine heat exchangers. The durability of a heat exchanger depends on many components, the obvious ones being the partition plates, braze connections, and fins. To predict heat exchanger service life, a cyclic stress strain scenario should be developed for the various heat exchanger components under duress, which may permit an estimation of the number of cycles until failure. To perform this task, one must begin with a thermal model to determine the temperature distributions during steady state and transient operation. When the temperature distributions are obtained for the various heat exchanger components, stress analyses may be performed, followed by creep analyses, which can ultimately lead to a legitimate heat exchanger service life calculation.

A transient thermal model of a counterflow heat exchanger partition plate and its working fluids was developed using an alternating direction implicit finite difference scheme. Four different temperature ramping rates were tested with this numerical model

for a specified temperature ramp up schedule. It was shown that all different temperature ramping rates yield noticeable transient thermal behavior, which was quantified through a parameter defined as heat lag. Intuitively, it was found that the faster the ramping rate, the larger heat lag becomes, which is known to be coincident with excessive thermal stress. Thus, to better understand why excessive thermal transients create severe levels of stress, the 30.0 °K/s ramping rate case was evaluated in the LTHERM Thermal Stress model.

The transient thermal model produced temperature data for candidate heat exchanger partition plates, for steady state and transient thermal stress calculations. During steady state, it was found that the partition plate develops tensile stress along its peripheries, and compressive stress in its inner region. In contrast, it was found that during a temperature ramp up procedure the partition plate can develop rather large compressive stress at its edges near the hot fluid inlet end of the plate, and tensile stresses near its inner region. Thus, as mentioned previously, portions of the partition plate can endure a complete shift in stress from tensile to compressive and then back to tensile stress again during a temperature ramp up procedure. Thermo-mechanical fatigue is of great concern when this type of loading is present. However, it was found that a heat exchanger that experiences temperature ramping consistent with high temperature fuel cells, or at about a rate of 0.03 °K/s, endures very little transient behavior and is not subject to this thermal stress undulation. Therefore, it was concluded that transient thermal stress can be ignored when determining max stresses/strains for calculating life in FCGT system heat exchangers that employ this slow of a ramping rate. It was also found that there is only a slight correlation between the timing of maximum heat lag and the most severe stress

state in heat exchanger partition plates. To find the most severe stresses during a thermal transient, one simply has to test several snapshots in time to ultimately produce a sketch of the transient thermal stress profile. It was confirmed however that concentrations of temperature contours can be used to coarsely identify severe stress times and locations.

It was found that the centers of the partition plate edges represented the locations of the most severe stress in the partition plates analyzed herein, which may well hold true for more complex heat exchanger partition plate designs. The validity of the thermal stress distributions were established through the use of two, four bar linkage idealizations. It was learned that the aspect ratio (Width/Length) of a heat exchanger partition plate has a major effect on the magnitude of thermal stress produced within the plate, where the larger the aspect ratio the larger the thermal stress will be. This finding is perhaps the most important since it is fundamental to partition plate design. In all likelihood, this conclusion will hold true for more complex heat exchanger partition plate geometries.

Approximate creep behavior of a partition plate operating at high temperature (up to 1120 °K) constructed out of solution-treated Inconel 625 was modeled in this work. Using the most relevant experimental data found in the literature, a primary creep law for Inconel 625 was formulated and used in the HTHE Thermal Stress model to predict creep behavior. The accuracy of this creep law was considered only approximate, though as it turned out, its accuracy may not have been crucial. The creep results for the Inconel 625 partition plate showed that any stress within the hot fluid inlet region of the plate will diminish to virtually zero stress within the 300 hour operating cycle. This stress

relaxation was also found to be accompanied by a significant amount of creep deformation. Therefore, it was apparent that the creep resistance of Inconel 625 was not overestimated by the creep law constructed in this work. It was also found that the aspect ratio (Width/Length) of the heat exchanger partition plate had an even larger effect on the amount of creep behavior produced in the plate than it did on the amount of thermal stress produced in the plate. Again, the larger the aspect ratio the larger the amount of creep there will be.

Numerical modeling tools were developed in this work that enable the appropriate balance of heat exchanger parameters such as compactness, pressure drop, and partition plate width for the ultimate goal of minimizing heat exchanger cost and extending service life. Quick evaluation of counterflow heat exchanger designs can be carried out with the techniques discussed herein.

Recommendations for Future Work

The following list summarizes several points of interest that would be evaluated if this work was continued. There are two main areas that are discussed, namely preliminary modeling and detailed modeling. The numerical techniques developed in this work fall under the preliminary modeling category, which were intended to help guide the heat exchanger design process. Eventually, models having detailed heat exchanger structures and fewer simplifications will eventually be necessary to accurately predict heat exchanger service life. The recommendations listed below relate to the areas of

thermal and structural modeling, material evaluation, and overall heat exchanger development.

1. Future work considerations pertaining to thermal and structural modeling:

- To quickly obtain approximate values of thermal stress at partition plate / braze interfaces, a layer of braze material would be added to both sides of the partition plate in the Transient Thermal Simulation and thermal stress models.
- Increased detail such as radiation and stream-wise variations in heat transfer and friction coefficients would be added to the Fine Filter model. These variations, as well as temperature dependent properties such as plate density and thermal conductivity, would be added into the Transient Thermal Simulation model.
- Using the ANSYS model, various heat exchanger partition plate configurations would be tested to develop a low stress heat exchanger design. Provisions would be made to account for the effects of sealing and stacking the heat exchanger cells. Once these details are built into the models, stress and creep induced by differential fluid pressure would be evaluated.
- When the stress and creep analyses are completed, life cycle prediction of the high stress heat exchanger components would be made using techniques such as the strain range partitioning method.

2. Future work considerations pertaining to material selection:

- Creep laws for multiple high temperature partition plate and braze materials would be developed. The performance of these heat exchanger materials would be evaluated in the models described previously.

- Use of coatings to help prevent oxidation and corrosion in the FCGT heat exchangers would be evaluated. Cracks initiated in oxidation layers can often propagate into the substrate.
3. Future work considerations pertaining to overall heat exchanger development:
- Based on the preliminary plate / braze stress analysis that would be performed, the alternative of using diffusion bonding for the high temperature application (>925 °K) would be evaluated.
 - The most conducive cleaning and or filtering technique for hybrid FCGT system heat exchangers would be determined to mitigate the effects of fouling.
 - Methods to reduce heat exchanger parts count, the number of braze connections, tooling costs, and scrap metal waste during production would be examined.
 - The use of a non-monolithic, double fin layer on the hot fluid side (which is also known as a split gas fin) would be modeled. The hot and cold fin positions would be varied to minimize the creation of hot spots within the heat exchanger.
 - The various heat exchanger support structures, enclosures, and header designs would be examined.

REFERENCES CITED

REFERENCES CITED

- Abiko, T., Tujii, J., and Eta, T., "Plate Fin Type Heat Exchanger For High Temperature", United States Patent Application Number US 2003/0075308 A1, Apr. 24, 2003.
- Bacquet, N., "The Spiral Heat Exchanger Concept and Manufacturing Technique", Compact Heat Exchangers and Enhancement Technology for the Process Industries, edited by Shah, R., Deakin, A., Honda, H., and Rudy, T., Begell House, Inc., 2001.
- Behm, P. Personal Communication, Brown FinTube, 2003.
- Bonet, J. and Wood, R. D., "Nonlinear Continuum Mechanics for Finite Element Analysis", Cambridge University Press, 1997.
- Boyer, H.E., "Atlas of Creep and Stress-Rupture Curves", ASM International, Chap. 5, 1988.
- Chapra, S.C., and Canale, R.P., "Numerical Methods for Engineers: With Programming and Software Applications", 3rd Edition, McGraw-Hill, Chaps. 11, 21, and 30, 1998.
- Child, M.S., Kesseli, J.B., and Nash, J.S., "Unit Construction Plate-Fin Heat Exchanger", United States Patent Number 5,983,992, Nov. 16, 1999.
- Deakin, A., Hills, P., Johnston, T., Adderley, C., Owen, R., Macdonald, T., Gregory, E., Lamb, B., Patel, N., Haseler, L., "Guide to Compact Heat Exchangers", Energy Efficiency Enquiries Bureau, Oxfordshire, 1999.
- Esbeck, D., Gates, S., and Schneider, P. "Industrial Advanced Turbine Systems Program Overview", Research Sponsored by the U.S. Dept. of Energy's Morgantown Energy Technology Center, 1998.
- Feltham, P., "On the Validity of Mott's Theory of the Beta-Flow in Polycrystals", Philosophical Magazine, 44, pp. 9 – 12, 1953.
- Fraas, A. P., and Ozisik, M., "Heat Exchanger Design", John Wiley & Sons, Inc., New York, 1965.
- Gadala, M.S. and Wang, J., "Simulation of Metal Forming Processes with Finite Element Methods", International Journal for Numerical Methods in Engineering, Vol. 44, pp. 1397-1428, 1999.
- Hesselgreaves, J. E., "Compact Heat Exchangers – Selection, Design, and Operation", Pergamon, New York, 2001.

- Ingersoll-Rand, "Gas-Turbine Engine Manufacturers Consider the PowerWorks™ Recuperator for Long-Term Survival, Better Efficiency, and Low Life-Cycle Cost", NREC News, Volume 11, Issue 2, 1997.
- Ingersoll-Rand, "PowerWorks™ Recuperator, A Breakthrough Technology For Gas-Turbine Performance", 2001.
- Kandlikar, S. G., Grande, W. J., "Evolution of Microchannel Flow Passages – Thermohydraulic Performance and Fabrication Technology", (2002) [Online]http://www.rit.edu/~taleme/77_imece2002_32043.pdf.
- Kays, W.M., and London, A.L., "Compact Heat Exchangers", 3rd Edition, Krieger Publishing Company, Florida, pp. 240, 1984.
- Kesseli, J., Wolf, T., Nash, J., Freedman, S., "Micro, Industrial, and Advanced Gas Turbines Employing Recuperators", Proceedings of ASME Turbo Expo, Atlanta, Georgia, USA, 2003.
- Kraus, A., Aziz, A., Welty, J., "Extended Surface Heat Transfer", John Wiley & Sons, Inc., New York, 2001.
- Kretzinger, K., Valentino, S., and Parker, K., "Heavy duty regenerators for gas turbines", Modern Power Systems, pp. 55-61, March, 1983.
- Kunitomi, K., Takeda, T., Horie, T., and Iwata, K. "Development of Compact Heat Exchanger With Diffusion Welding", Document XA9642788, 1999.
- Leo, A.J., Ghezal-Ayagh, H., and Sanderson, R., "Ultra High Efficiency Hybrid Direct Fuel Cell / Turbine Power Plant", ASME Turbo Expo Paper 2000-GT-0552, Munich, Germany, 2000.
- Mathew, M.D., Bhanu Sankara Rao, K., Mannan, S.L., "Creep properties of Service-exposed Alloy 625 after re-solution annealing treatment", Materials Science and Engineering A, 372, pp. 327 – 333, 2004.
- McDonald, C. "Gas Turbine Recuperator Technology Advancements, Materials Issues in Heat Exchangers and Boilers", The Institute of Materials, London, England, 1997.
- McDonald, C., "Low-cost primary surface recuperator concept for microturbines", Applied Thermal Engineering, 20, pp. 471 – 479, 2000.
- McDonald, C., "Recuperator considerations for future higher efficiency microturbines", Applied Thermal Engineering, 23, pp. 1463 – 1487, 2003.

- McMeeking, R.M. and Rice, J.R., "Finite Element Formulations for Problems of Large Elastic-Plastic Deformation", *International Journal of Solids and Structures*, Vol. 121, pp. 601-616, 1975.
- Oswald, J., Personal Communication, Rolls Royce, 2003.
- Parker, K. O., "Plate regenerator boosts thermal and cycling efficiency", *The Oil and Gas Journal*, pp. 74-78, April 11, 1977.
- Patankar, S.V., "Numerical Heat Transfer and Fluid Flow", Hemisphere Publishing Company, Chaps. 3 and 4, 1980.
- Pint, B., Swindeman, R., Tortorelli, P., More, K., "Materials Selection for High Temperature Metallic Recuperators for Improved Efficiency Microturbines", Microturbine Materials Program, Oak Ridge National Laboratory, 1999.
- Reid, G., "A numerical investigation of microchannel heat transfer", Masters Thesis, University of Seattle, Washington, 1998.
- Rodriguez, R., Hayes, R.W., Berbon, P.B., Lavernia, E.J., "Tensile and creep behavior of cryomilled Inco 625", *Acta Materialia*, 51, pp. 911 – 929, 2003.
- Sanders, R.C. and Louie, G.C., "Development of the WR-21 Gas Turbine Recuperator", Paper Number 99-GT-314, Presented at the International Gas Turbine and Aeroengine Congress and Exhibition, Indianapolis, Indiana, June 7 – 10, 1999.
- Shah, R. K., "Classification of Heat Exchangers", *Heat Exchangers – Thermal-Hydraulic Fundamentals and Design*, edited by Kakac, S., Bergles, A., and Mayinger, F., Hemisphere Publishing Corporation, 1981.
- Shah, R. K. and Webb, R. L., "Compact and Enhanced Heat Exchangers, Heat Exchangers – Theory and Practice", edited by Taborek, J., Hewitt, G. F., and Afgan, N., Hemisphere Publishing Corporation, 1983.
- Shah, R. K., "Plate-Fin and Tube-Fin Heat Exchanger Design Procedures", *Heat Transfer Equipment Design*, edited by Shah, R. K., Subbarao, E. C., and Mashelkar, R. A., Hemisphere Publishing Corporation, 1988.
- Shah, R. K., "Compact Heat Exchangers", *The CRC Handbook of Thermal Engineering*, edited by Kreith, F., CRC Press, New York, 2000.
- Shah, R. K. and Sekulic, D. P., "Fundamentals of Heat Exchanger Design", John Wiley and Sons, Inc., New Jersey, 2003.
- Snider, A. D., "Introduction to Vector Analysis", Allyn and Bacon, Inc., New York, 1979.

- Solar Turbines Inc., A Caterpillar Company, Recuperators (Brochure), Recuperator Development, Dept. 221, T-5, P.O. Box 85376, San Diego, CA. 92186-5376, 1995.
- Stinton, D.P., and Raschke, R.A., "DER MATERIALS QUARTERLY PROGRESS REPORT, January 1 – March 31", Oak Ridge National Laboratory, 2004.
- Utriainen, E., and Sunden, B., "Recuperators and regenerators in gas turbine systems, Investigation of Some Heat Transfer Surfaces for Gas Turbine Recuperators", Lund, Sweden, 2001a.
- Utriainen, E., Sunden, B., "Numerical analysis of a primary surface trapezoidal cross wavy duct", Investigation of Some Heat Transfer Surfaces for Gas Turbine Recuperators, Lund, Sweden, 2001.
- Valentino, S. J., "Designing Reliability into High-Effectiveness Industrial Gas Turbine Regenerators", Transactions of the ASME, Vol. 102, pp. 518-523, July, 1980.
- Voss, M.G., Personal Communication, Modine Manufacturing Company, 2004.
- Wadekar, V., "Compact Heat Exchangers", American Institute of Chemical Engineers. (2003) [Online] www.aiche.org/cep/.
- Walker, G., "Industrial Heat Exchangers, 2nd Ed.", Hemisphere Publishing Corp, New York, 1990.
- Wang, C., "Design, Analysis and Optimization of the Power Conversion System for the Modular Pebble Bed Reactor System", Doctoral Thesis, Massachusetts Institute of Technology, Massachusetts, 2003.
- Webster, G. A. and Ainsworth, R. A., "High Temperature Component Life Assessment", Chapman and Hall, London, 1994.

APPENDICES

APPENDIX A

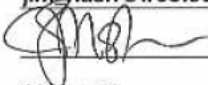
PERMISSION TO USE IMAGES

Photo Consent and Release

I, JimNash, grant permission to Joel D. Lindstrom of Montana State University - Bozeman for the use of the photograph(s) or electronic media images as identified below for use in Joel D. Lindstrom's Masters Thesis document, of which will be subject to publication and copyright; further, I grant such use for no fee or charge whatsoever. I hereby release Joel D. Lindstrom and Montana State University - Bozeman from all claims of every kind related to such use.

Additionally, I certify by signing below, that I have the authority to grant permission to use the photograph(s) and image(s) noted below without charge to Joel D. Lindstrom or Montana State University - Bozeman.

Holder Release

Name	<u>Jim Nash</u>
Company	<u>Ingersoll-Rand Energy Systems</u>
Street Address	<u>130 New Hampshire Avenue</u>
City / State / Zip	<u>Portsmouth, NH 03801</u>
Phone	<u>603-430-7108</u>
E-mail	<u>jim_nash@irco.com</u>
Signature	
Date	<u>12 Jan 05</u>

Photograph(s) / Image(s)

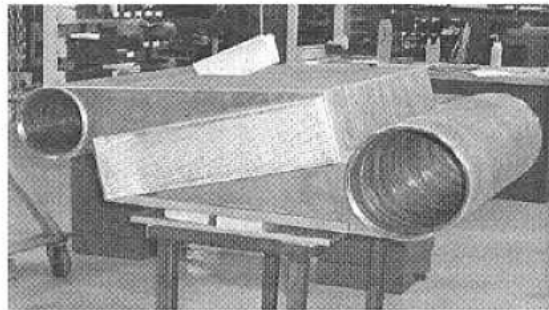
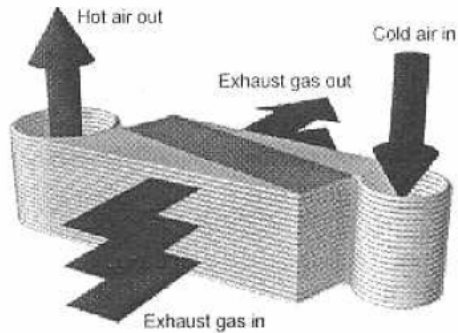


Photo Consent and Release

Axima Refrigeration GmbH grants permission to Joel D. Lindstrom of Montana State University - Bozeman for the use of the photograph(s) or electronic media images as identified below for use in Joel D. Lindstrom's Masters Thesis document, of which will be subject to publication and copyright; further, I grant such use for no fee or charge whatsoever.

Additionally, I certify by signing below, that I have the authority to grant permission to use the photograph(s) and image(s) noted below without charge to Joel D. Lindstrom or Montana State University - Bozeman.

Holder Release

Name	Mr. Frank Uebelen
Company	Axima Refrigeration GmbH
Street Address	Kemptener Str. 11-15
City / State / Zip	88131 Lindau (Germany)
Phone	08382-706-354
E-mail	Frank.Uebelen@de.axiref.com
Signature	 Axima Refrigeration GmbH Lindau, Bodensee
Date	01th March 2005

Photograph(s) / Image(s)

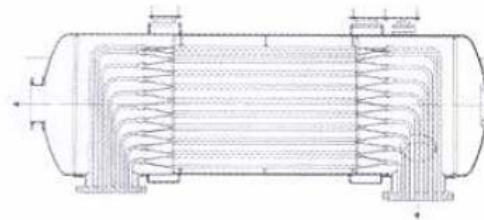
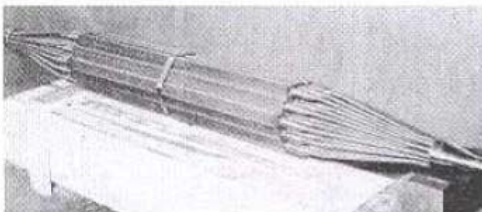
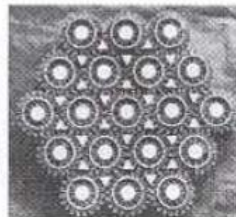
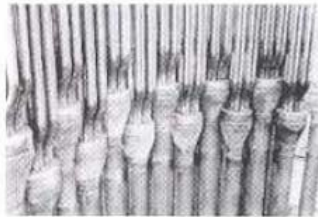


Photo Consent and Release

I, Odito grant permission to Joel D. Lindstrom of Montana State University - Bozeman for the use of the photograph(s) or electronic media images as identified below for use in Joel D. Lindstrom's Masters Thesis document, of which will be subject to publication and copyright; further, I grant such use for no fee or charge whatsoever. I hereby release Joel D. Lindstrom and Montana State University - Bozeman from all claims of every kind related to such use.

Additionally, I certify by signing below, that I have the authority to grant permission to use the photograph(s) and image(s) noted below without charge to Joel D. Lindstrom or Montana State University - Bozeman.

Holder Release

Name _____

Company _____

Street Address _____

City / State / Zip _____

Phone _____

E-mail _____

Signature _____

Date _____



089 114 83 2698

odito.unmelting@unmc.mtu.de

i.V. Odito

2.2.05

Photograph(s) / Image(s)

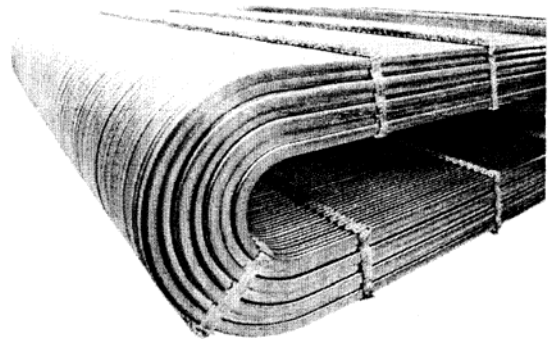
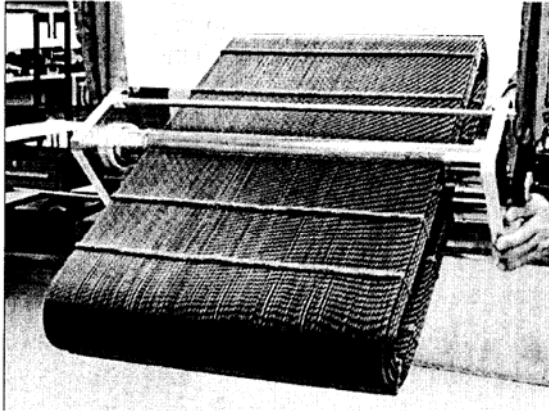
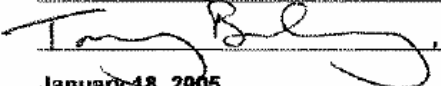


Photo Consent and Release

I, Tony Bowdery, grant permission to Joel D. Lindstrom of Montana State University - Bozeman for the use of the photograph(s) or electronic media images as identified below for use in Joel D. Lindstrom's Masters Thesis document, of which will be subject to publication and copyright; further, I grant such use for no fee or charge whatsoever. I hereby release Joel D. Lindstrom and Montana State University - Bozeman from all claims of every kind related to such use.

Additionally, I certify by signing below, that I have the authority to grant permission to use the photograph(s) and image(s) noted below without charge to Joel D. Lindstrom or Montana State University - Bozeman.

Holder Release

Name	Tony Bowdery
Company	Heatric
Street Address	11490 Westheirner, Suite 850
City / State / Zip	Houston, TX, 77077
Phone	713-978-7236
E-mail	Tony.Bowdery@Heatric.com
Signature	
Date	January 18, 2005

Photograph(s) / Image(s)

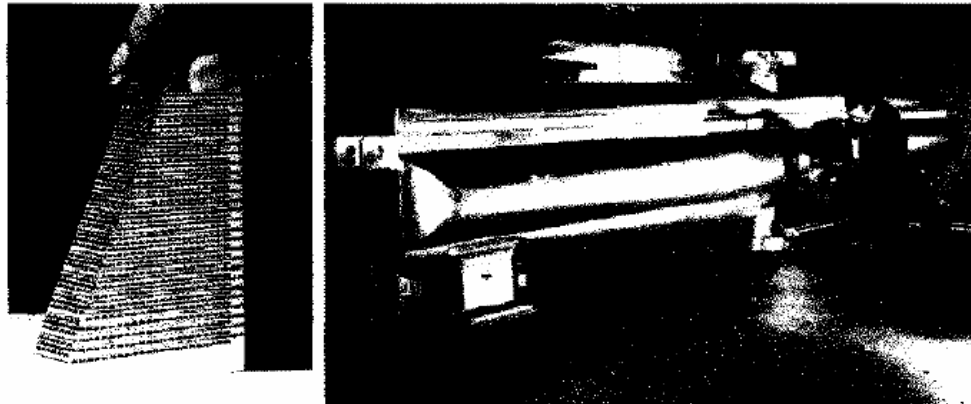



Photo Consent and Release

I, Philippe Moliteur, grant permission to Joel D. Lindstrom of Montana State University - Bozeman for the use of the photograph(s) or electronic media images as identified below for use in Joel D. Lindstrom's Masters Thesis document, of which will be subject to publication and copyright; further, I grant such use for no fee or charge whatsoever. I hereby release Joel D. Lindstrom and Montana State University - Bozeman from all claims of every kind related to such use.

Additionally, I certify by signing below, that I have the authority to grant permission to use the photograph(s) and image(s) noted below without charge to Joel D. Lindstrom or Montana State University - Bozeman.

Holder Release

Name	Moliteur Philippe
Company	ACTE s.a.
Street Address	Rue Gilles Magnée, 92
City / State / Zip	4430 ANS, Belgique
Phone	+32 4 247 11 24
E-mail	<u>info@acte-sa.be</u>
Signature	
Date	14/01/2005

Photograph(s) / Image(s)

